Study on precise airway segmentation from chest CT volumes based on machine learning and local intensity analysis

MENG Qier

Abstract

Lung cancer has become one of the leading causes of cancer-related death, accounting for 1.6 million deaths. Therefore, early detection and diagnosis are necessary. In diagnosis and surgery on lung cancer, a physician always wants to obtain useful and precise information for the assessment of the lesion in the lung. With the development and improvement of the 3-D CT and the generation of high-resolution data, more accurate treatment of disease is feasible. Thus, the segmentation of airway trees in the 3D chest computerized tomography (CT) volume is an important step in the analysis of various pulmonary diseases like asthma and chronic bronchitis.

This work introduces several new approaches for airway segmentation which is a vital core component of computerized aided diagnosis. There are several proposed methods developed to segment the airway from the 3D CT volumes. One method is composed of three steps. First, Hessian analysis is utilized to enhance the tube-like structure in CT volumes, then an adaptive multiscale cavity-enhancement filter is employed to detect the cavity-like structure with different radii. In the second step, support vector machine (SVM) learning will be utilized to remove the false positive (FP) regions from the result obtained in the previous step. Finally, the graph-cut algorithm is used to refine the candidate voxels to form an integrated airway tree.

Second one is recognizing the airway regions from the trachea using the volume of interests (VOIs) to segment each branch. A VOI is placed to envelop the branch currently being processed. Then a cavity enhancement filter is performed only inside the current VOI so that each branch is extracted. At the same time, we perform a leakage detection scheme to avoid any leakage regions inside the VOI. Next the GVF magnitude map and a tubular-likeness function are computed in each VOI. This assists the predictions of both the position and direction of the next child VOIs to detect the next child branches

to continue the tracking algorithm. Finally, we unify all of the extracted airway regions to form a complete airway tree.

In the last work, we combine 3D deep learning with image-based tracking in order to automatically extract the airways. Our method is driven by adaptive cuboidal volume of interest (VOI) analysis using a 3D U-Net model. We track the airways along their centerlines and set VOIs according to the diameter and running direction of each airway. After setting a VOI, the 3D U-Net is utilized to extract the airway region inside the VOI. All extracted candidate airway regions are unified to form an integrated airway tree. We trained on 30 cases and tested our method on an additional 20 cases. Compared with other state-of-the-art airway tracking and segmentation methods, our method can increase the detection rate by 5.6 while decreasing the false positives (FP) by 0.7 percentage points.

Keywords:

Airway segmentation, Computer aided diagnosis, Hessian analysis, Support vector machine, Multiscale cavity-enhancement filter, Volume of interests, Gradient vector flow, Fully convolutional network.

Contents

List of Figures

List of Tables

Study on precise airway segmentation from chest CT volumes based on machine learning and local intensity analysis

Qier Meng

Chapter 1

Introduction: Airway segmentation uses for therapeutic and diagnostic

Lung cancer is one of the leading cancers, and there were around 1.6 million deaths (around 20% of all cancer-related deaths) in 2015 [1]. Therefore, early detection and diagnosis are necessary. In diagnosis and surgery on lung cancer, a physician always wants to obtain useful and precise information for the assessment of the lesion in the lung. With the development and improvement of the 3-D CT and the generation of high-resolution data, more accurate treatment of disease is feasible. The morphological effects of a great number of pathologies are different in the bronchial regions and the parenchyma. Thus, the segmentation of airway trees in the 3D chest computerized tomography (CT) volume is an important step in the analysis of various pulmonary diseases like asthma and chronic bronchitis. To obtain precise recognition of the airway, the extraction of an airway tree from a 3D CT volume is an important step for analyzing different kinds of diseases such as pneumothorax and asthma. Since a single CT examination usually contains hundreds of slice images, it is extremely difficult and time-consuming to manually trace airway trees and might take over seven hours of intensive work per volume in our experience [2]. To reduce the workload on physicians, a precise method for airway segmentation from chest CT volumes in a computer-aided system is required. At the same time, the extraction of the airway tree is always helpful for other segmentation, for instance lobe, nodule and pulmonary segmentation [3, 4, 5, 6, 7].

Another application of airway extraction is virtual bronchoscopy, which is usually used as planning and guidance for bronchoscope navigation [8, 9]. A precise segmentation result can provide physicians plenty of information for diagnosis and surgery. To decrease the incidence rates and the mortality of chest disease and cancer patients, early detection and diagnosis are greatly needed, which is to allow us to do more effective treatment in the preliminary stages of these diseases [10][11][12][13][14]. In the diagnosis and treatment of the phycisians, medical imaging is quite important, because of the computer tomography (CT), Magnetic Resonance Imaging (MRI), and ultrasound (US) diagnostics can provide lots of information of diseases and organs [15][16][17][18][19]. However, the radiologist has to study a lot of medical image in a comprehensive way quickly. To reduce the amont of their work, the technology developed from the computer to process the medical image is used: computer-aided diagnosis (CAD) [20][21][22][19]. The CAD system is used to support the physicians during diagnosis and prescribing treatment. With CAD, the computer can reach the ability that physicians have, and can achieve some tasks that require human assistance. In fact, there is a large number of CAD systems developed to help the doctors to check the disease in the early stage for instance the chest CAD system and the colonography CAD system[19].

In CAD system development, the airway segmentation plays an important role. Image segmentation is the procedure of separating regions in an image into objective regions belonging to different objects. It is necessary to separating the objects of interest when we process an image. We do such applications on medical imaging analysis, where the physicians are usually concerned with the organs in the image [23]. Precise airway segmentation from CT volumes is essential in medical imaging analysis because precisely quantifying the disease parts is always a difficult task for humans [24][25].The quantification of emphysema in lungs, a typical example of a quantification method for diseases regions is to measure low CT value regions [26]. Other measurement would be used by providing precise measured of airway wall and completed airway tree segmentation [27].

Airway segmentation is applied for other purposes. In computer-assisted surgery, we need to perform the airway segmentation from CT images for the consideration of visualization and manipulation. Airway segmentation can be utilized the landmark detection in the surgery navigation system.

This thesis presents three automated airway tree segmentation methods in chest computed tomography (CT) scans. This chapter generally briefly shows medical background of our research and chest anatomy.

1.1 Lung Anatomy

The lung in the chest includes two large organs used for respiration located in the chest, and it is responsible for inhaling oxygen from the air and expelling the carbon dioxide from the blood. In humans, each lung is wrapped in a thin membranous sac called the pleura, and each is connected with the trachea (windpipe) by its main bronchus (large air passageway) and with the heart by the pulmonary arteries [28]. A structure called the mediastinum separates the lungs. Each lung consists of the heart, the trachea, the esophagus, and blood vessels, the right lung has three lobes, and the left lung has two lobes [28]. Figure 1.2 shows the lung anatomy [29].

1.2 Bronchus Anatomy

The airway tree is the organ of the respiratory system that conducts the air from the upper airways to the lung parenchyma. The airway consists of the trachea and the intrapulmonary airways [28]. Trachea diameters vary widely, ranging from 10 to 25 mm in the coronal plane. Bronchi is plural for bronchus and represent the passageways leading into the lungs. Bronchi will branch into smaller tubes that become bronchioles. These are 3mm or less. Then, it reaches air sacs. This sac is called alveoli and the place, where the actual gas molecules of oxygen and carbon dioxide are exchanged between the respiratory spaces and the blood capillaries [28]. Figure 1.2 shows the bronchus anatomy [30].

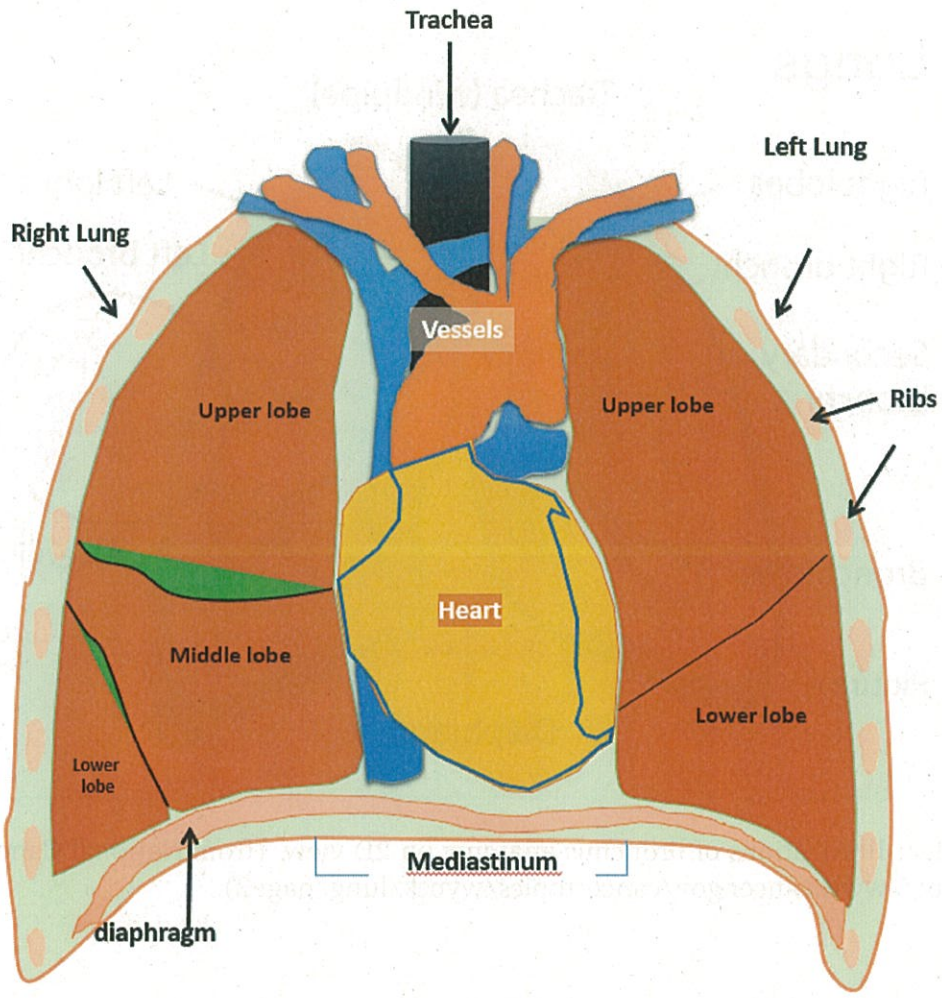

Figure 1.1: Illustrations of lung anatomy on 2D view. (from National Cancer Institute http://www.cancer.gov/cancertopics/wyntk/lung/page2)

1.2.1 Bronchus on CT

In chest CT scans, airways appear as dark tubular regions. that are surrounded by brighter bronchial walls. Bronchial branches makes furcations with decreasing diameters. While contrasting the airway lumen in trachea with large diameters is easy, the differentiation of peripheral airway branches from lung parenchyma becomes much more difficult due to partial volume effects (PVEs).[28] Generally, doctors use three sections to examine the human body from the CT volume. We demonstrate these three sections obtained from a 3D chest CT volume in Figure 1.3. From these CT slices we

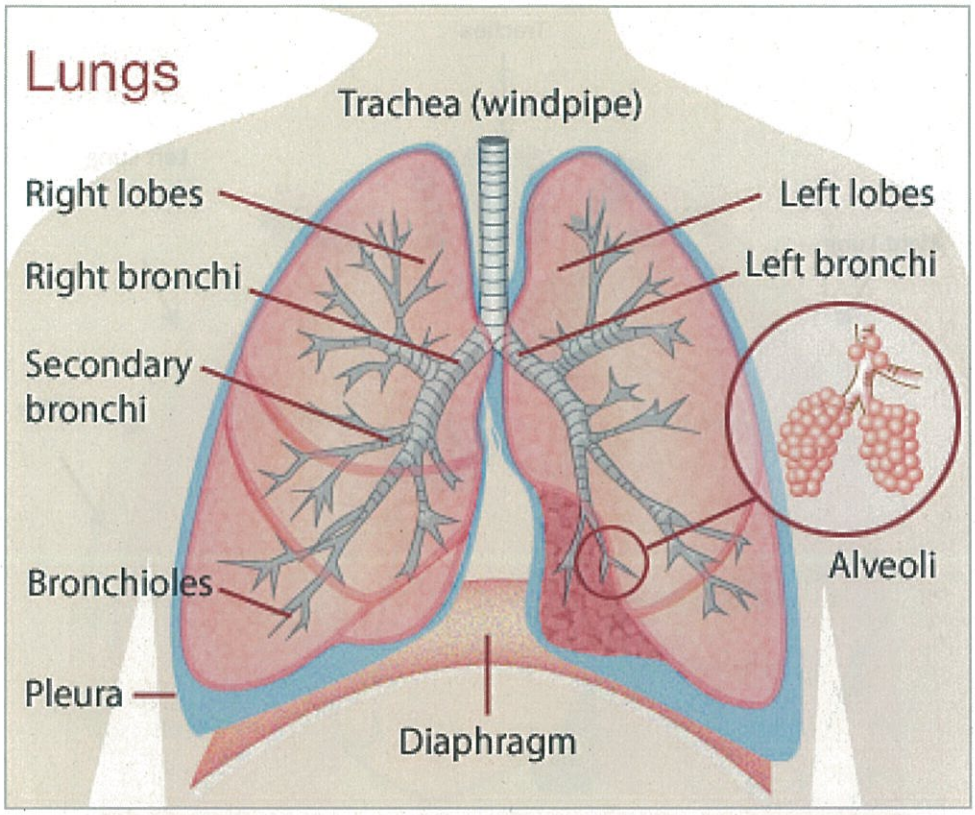

Figure 1.2: Illustrations of bronchus anatomy on 2D view. (from National Cancer Institute http://www.cancer.gov/cancertopics/wyntk/lung/page2)

can find that the bronchus consists of the following components [31]:

(1) Trachea: The trachea, called the windpipe, is a cartilaginous tube that connects the pharynx and larynx to the lungs [32].

(2) Principal bronchus: A principal bronchus, also known as a main or primary bronchus, is an airway in the respiratory tract that conducts air into the lungs [32].

(3) Bronchus: Any of the larger passages conveying air to a lung and within the lungs [32].

(4) Peripheral bronchi: The bronchi, singularly known as a bronchus, are extensions of the windpipe that shuttle air to and from the lungs [32].

(5) Bronchiole: The tiny branch of air tubes within the lungs that is a continuation of the bronchus. The bronchioles connect to the alveoli (air sacs) [32].

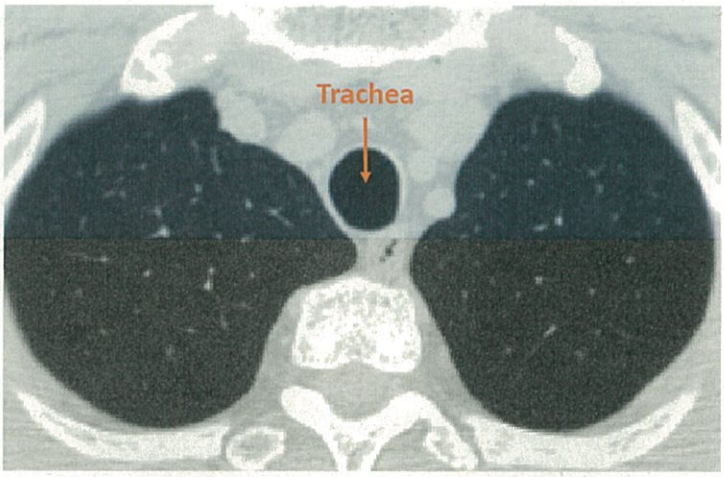

(a) Trachea regions on axial slice.

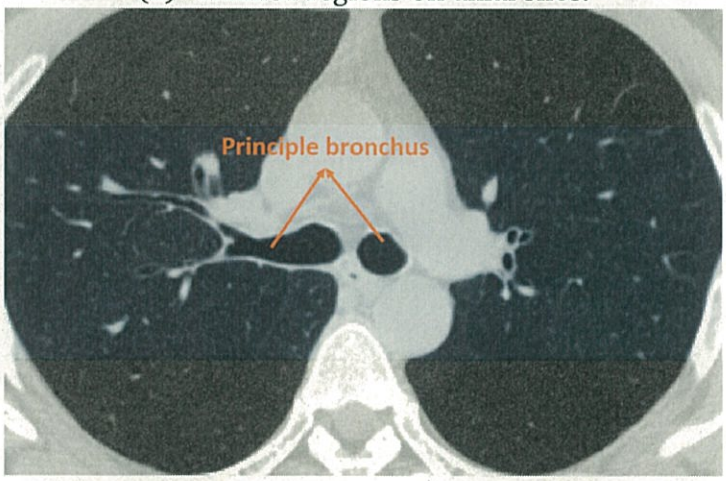

(b) Principle bronchus regions on axial slice.

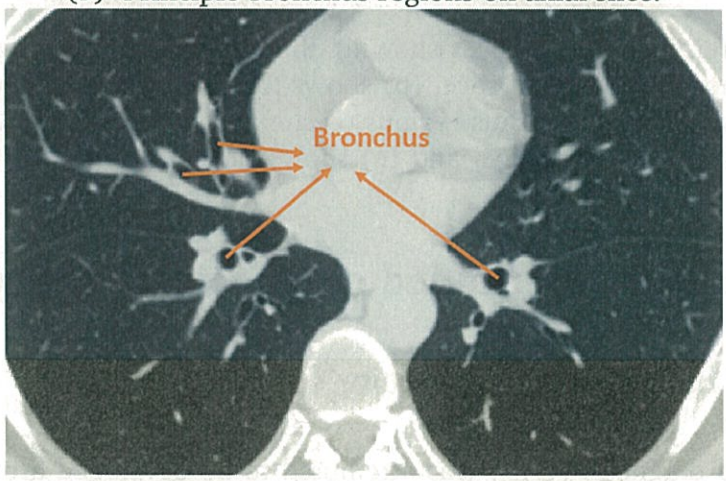

(c) Bronchus regions on axial slice.

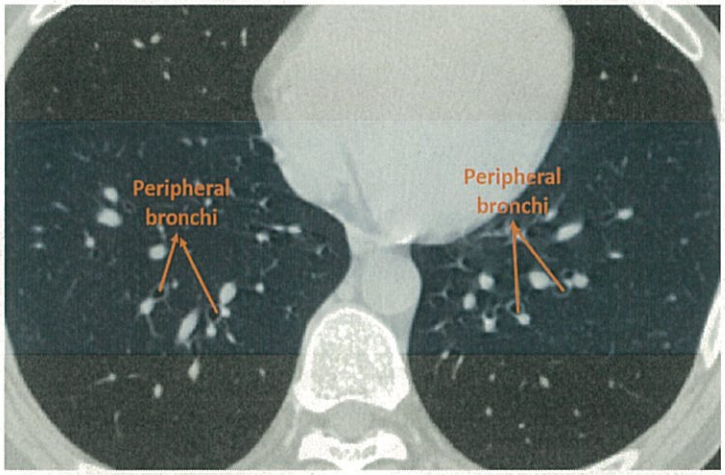

(d) Peripheral bronchi regions on axial slice.

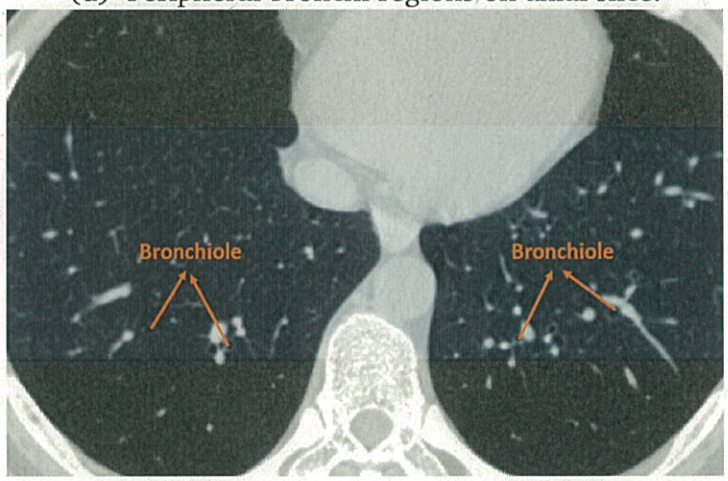

(e) Bronchiole regions on axial slice.

Figure 1.3: Different CT axial slices showing the airway structure regions. (a) shows the trachea regions on the axial slice, (b) shows the principle bronchus regions on the axial slice, (c) shows the bronchus regions on the axial slice, (d) shows the peripheral bronchi regions on the axial slice, and (e) shows the bronchiole regions on the axial slice.

1.3 Chest computer-aided diagnosis (CAD) system

1.3.1 Brief history of CAD system

Computer-aided diagnosis (CAD) was attempted to be developed around 1970 by researchers. In recent years, CAD attracts a lot of attentions in the medical imaging analysis field. CAD is an important tool for assisting the doctors during diagnosis and surgery. A CAD system is usually confined to marking conspicuous structures and eval-

Figure 1.4: Interface of CAD system in our laboratory.

uates such structures. Also, a CAD system is expected to help doctors in analyzing effective treatment and giving opinions for therapy planning.

1.3.2 CT Colonography CAD system

Computed tomography (CT) colonography is a screening modality which is used to examine colonic polyps before the deterioration of colorectal cancer occurs. Colorectal cancer screening can reduce mortality from colorectal cancer by 13% to 18%. Current screening guidelines include optical colonoscopy, the most frequently recommended study. However, patient compliance with optical colonoscopy is poor for several reasons, including discomfort with the procedure and bowel cleansing, as well as cost.

1.3.3 Chest CAD system

The most important application of the lung CAD system is to detect the suspicious regions and to diagnose the disease. Various studies have been devoted to the construction of a CAD system in recent years [33][34][35][36]. The segmentation of the airway tree

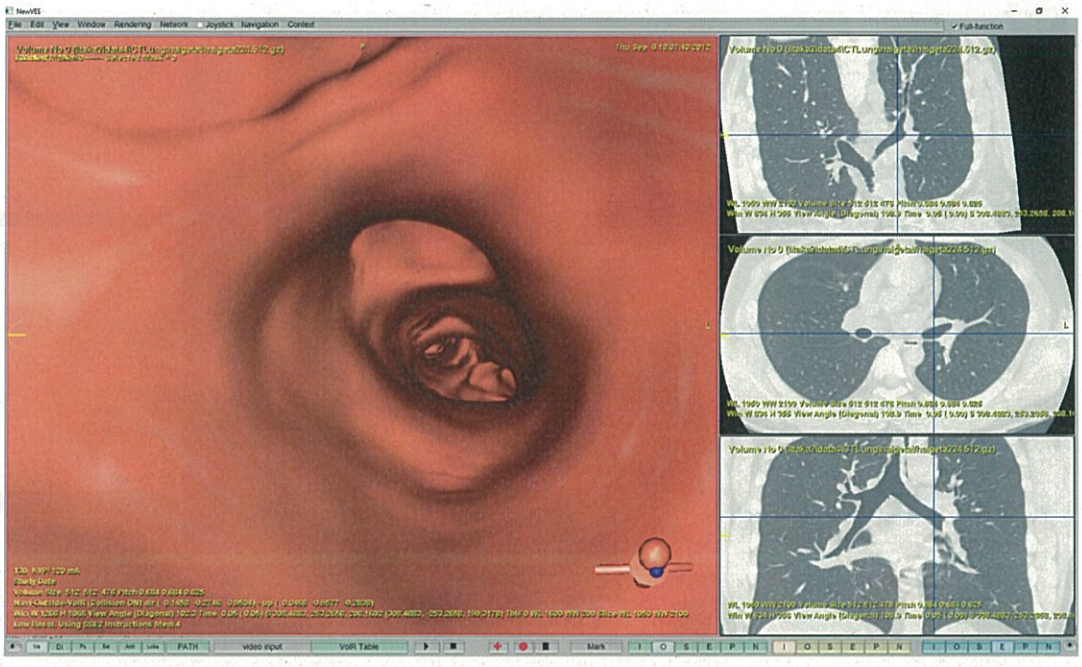

Figure 1.5: Interface of virtual bronchoscopy system in our laboratory.

from chest images is an essential task in CAD systems, which provides assistance to early diagnosis of lung cancer, as well as other lung diseases. The segmentation of the airway tree is a very challenging problem due to its complex structure. The airway segmentation result and its center-line can be used as the guideline and path of the bronchoscope navigation system. Since chest X-ray is the most common imaging modality. Many researchers focus on lung nodule detection from chest X-ray images. Hence, CAD system for chest CT images are the most popular research topics [37][38][39][40].

1.4 Computer-aided surgery (CAS) system used in chest CT volume: bronchoscopy navigation system

Computer-assisted surgery (CAS) contains the concept of surgery and certain methods that uses computer technology for assisting surgery including intervention guidance or surgical navigation. Typical principles used in CAS include a virtual image of the patient, image analysis and processing, surgical navigation, and robotic surgery. The

bronchoscope navigation system is developed for guiding bronchoscopic examination [41][42][43]. The airway segmentation result plays an important role in the bronchoscope navigation system.

1.4.1 Navigated bronchoscopy

Minimally invasive bronchoscopic procedures or interventions are often highly interactive; various operations are performed immediately by physicians in surgical rooms. While performing these operations, the physicians expect continuous visual feedback from the navigation-assisted system to help them control the medical tool movements. In navigated bronchoscopy, visual feedback requires the estimation of endoscope position and orientation in a 3D space. The navigated bronchoscopy is developed to enhance the capability of medical doctors to diagnose and treat patients, for example, by enabling them to rapidly and accurately localize the bronchoscope tip to tumor regions for a biopsy.

1.4.2 Virtual Bronchoscopy

Medical visualization is one of the popular topics in the medical imaging field. Visualized human body is widely discussed in the CAS field. We can simulate or examinations on vitrualization human body [44][45][46].

Virtual bronchoscopy (VB) is a technique to construct three-dimensional (3D) visualizations of the airway anatomy from pre-operative. It allows us to flythrough inside the bronchus for observation [14].

1.5 History of Airway Segmentation

Automated human airway tree segmentaion for CT examinations is a building block for most computerized airway-related analyses. Because there is a relative high contrast between the airway lumen and the airway wall. Usually, a simple way of extracting the airway tree from the 3-D chest CT volume is to use a 3-D region-growing procedure

specifically designed to identify the lumen regions. However, due to the partial volume effects (PVE) and image noise, a pure region-growing-based operation frequently leads to leakage into the parenchyma under a given threshold value. The leakage often occurs in small airways thereby leading to an early termination of the progressive airway tree detection. Although some schemes such as front propagation have been developed to prevent leakage, there is no strategy that can completely prevent the leakage occurring.

1.5.1 Region-growing methods

Mori et al. [47] proposed an approach of gradually increasing the threshold value used in region growing until a sudden leakage occurrence appears. Usually, when specifying a seed for region growing, the general idea is to locate the trachea regions that are typically defined as regions with low intensity and circular shapes. However, it is difficult to guarantee the seed point selected by this criteria that can extract the regions in the peripheral branches.

Despite these limitations, the region-growing approach is simple and efficient to implement. Therefore, many conventional methods use the region-growing-based method as an initial step for airway segmentation and hereafter implement additional procedures to identify smaller airways while preventing the potential leakage. According to the main characteristic of their methodology, the conventional airway segmentation methods can be categorized into several types (Table 1.1): (1) region-growing based methods, (2) morphological- based methods, (3) knowledge- or rule-based methods, (4) template matching-based methods, (5) machine learning-based methods [50].

1.5.2 Morphological methods

Whereas an airway tree always has a circular shape on the CT image slices, identification of an airway tree may be transformed into a task of detecting two-dimensional (2D) circular structures and then reconstructing them as a 3D airway tree. In nature, the morphological method aims to explore the specific shape, size, and intensity of the airways, as well as their spatial relationship on neighboring slices for airway identifica-

tion. For example, Aykac et al. [24] identified the original airways on CT slices by using gray-scale morphology and then reconstructing a connected 3-D airway tree. Rather than using a traditional morphological operation, Fetita et al. [84] derived a mathematical morphology operator based on the concept termed "connection cost", namely, the selective marking and depth-constrained connection cost (SMDC connection cost) for a complete airway reconstruction. The connection cost considers three types of regions related to airways, including (1) lumen, (2) airway walls, and (3) adjacent parenchyma tissue.

1.5.3 Knowledge- or rule-based methods

To utilize the property specific to the airway, various anatomical knowledge or rule based approaches have been utilized for airway identification. The features include (1) adjacency to vessels [51], (2) low airway intensity [52][53], (3) the degree of airway wall existence, (4) a progressive decrease in diameter. Usually, the combination of these rules may be used to achieve a better performance. Considering that airways are adjacent to vessels, Sonka et al. [54] defined a set of rules with regard to the spatial relationship between airways and vessels to detect the airways in a slice-by-slice manner. This method on five examinations shows higher sensitivity than the traditional region-growing method. However, the proposed method also results in a large number of false positive regions because the predefined rules do not necessarily satisfy the conditions of the existence of actual adjacent airways. Park et al. improved this method using a set of fuzzy rules that increased the specificity of the method without compromising its sensitivity. The fuzzy rules are organized using a table to detect the airways. In practice, it is very difficult to enumerate all rules associated with airways, and these rules may not give the actual identification of an airway. However these rules may be used along with other approaches for removing potential false positive regions.

1.5.4 Template matching methods

Template matching methods use a set of 2D/3D predefined masks (templates) to search for airway regions with similar shapes. Because of the tubular shape of airways, the commonly used masks are 2D circular templates with a range of sizes and intensity levels[55]. To identify airways in each image slice, shape matching is typically used. Airways always appear as circular or elliptical shapes in cross section only when the airway travels perpendicular to the scanning plane. Otherwise, there are several elliptical shapes in the airways, which makes it difficult to use a limited number of templates to fully describe the airways in a cross-sectional form. Also the variability in airway sizes also makes it difficult to identify the airway in a limited number of templates. In particular, the connection of airways with other tissues and the presence of lung disseases may result in inaccurate detection. To overcome the limitation of 2D circular templates [56], a 3D cylindrical is used shape to progressively obtain the airway starting from the trachea by adaptively predicting the size, orientation and position of the airway tree branches [57]. The utilization of a 3D cylinder template will prevent the leakage in the peripheral branches effectively.

1.5.5 Machine learning methods

The motivation for using machine learning methods is to capture the underlying probability distribution of specific airway characteristics by automatically summarizing the possible patterns and determining if these represent true airways. Lo et al. [58] developed a classifier that used several image appearance-based features and a K-nearest neighbor (KNN) classification approach to differentiate airways from non-airways at varying scales. Only the features that maximize the area under the receiver operating characteristics (ROC) curve of the KNN classifier were regarded as optimal. The involved training procedure is based on a cost function that considers several measures, including airway shape, airway orientation, and an airway probability map. Recently, Lo et al. [59] improved the approach using a combination of an airway appearance

model and a vessel orientation similarity measure. The appearance model uses a classifier that is trained with a set of easily acquired incomplete airway tree segmentations and is used to differentiate airways and nonairways. Whereas a training process is involved, the selected features and the diversity of the prelabeled data play a critical role in the ultimate performance of the airway tree identification.

Type	Studies	Case	Section thickness	Method	2D/3D	Auto	Performance
2	Aykac et al. (Ref [24])	8	3 mm	Morphological reconstruction	2D	Fully	1) Sensitivity: 73%
						2) Total 364 branches	
1	Bartz et al. (Ref [85])	22	1.0 mm	3D region growing, 2D wave propagation, and 2D template matching	2D + 3D	Semi	1) 7th generation 2) 20∼100s
1	Fabijanska et al (Ref [26])	10	0.625 mm	Region growing and morphological operation	3D	Fully	1) ∼9th generation 2) ∼10 min
3	Fetita et al. (Ref [27])	30	0.6 mm	Energy based reconstruction	3D	Fully	1) Sensitivity is ∼91%
2	Kiraly et al. (Ref [9])	30	0.6 mm	3D region growing and mathematical morphology	3D	Fully	1) 2∼25min 2) 12 generations per case
4	Mayer et al. (Ref [55])	22	1.25 mm	3D region growing, 2D wave propagation, 2D template matching	2D + 3D	Fully	1) Sensitivity: 86%∼94% 2) 27 s
3	Tschirren et al. (Ref [56])	22	0.6 mm	Fuzzy connectivity	3D	Fully	1) 27.0 ± 4.4 segments
5	Lo et al. (Ref [2])	15		Machine learning Region-growing	3D	Fully	1) TPR : 98.68% 2) False discovery rate: 24.94%
1	Sonka et al. (Ref [54])	44	3.0 mm	3D region growing, rules, anatomical knowledge	2D + 3D	Fully Fully	1) Sensitivity: 69%∼87%

Table 1.1: Summary and comparison of several airway segmentation methods.

1.5.6 Disadvantages of current methods

This section summarizes the key to the question of current airway-segmentation methods. We are concerned with the limitation of the segmentation methods of the airway structure. These limitations are discussed in the following paragraphs. Figure 1.6 shows examples of four different airway extraction results.

(1) Airway-tree segmentation is a difficult problem for many reasons. While voxel intensity of the airway region is around -1,000 H.U., it is impossible to use only a simple threshold to identify all of the airway voxels from the CT volumes due to the noise and partial volume effects. 3D region growing has a fast speed to extract the airway, but it is affected easily by partial volume effects and noise. The thresholds change from large airways to small airways. Most of the conventional methods based on region-growing can either describe incomplete structures or suffer from leakage in parenchyma regions. This disadvantage corresponds with the region-growing method.

(2) The mathematical morphology includes the operations in image processing that utilize the properties of shape and gray-scale. Airway segmentation methods based on mathematical morphology consists of two or more processing phases. First, airway candidate regions are detected by different kinds of morphological operations. We distinguish the airway and others based on 3D relationship and shapes. While these methods are popular and effective, the computation time is quite long and impossible to be implemented. Variations in the morphological operator's property directly affect candidate determination. In addition, the reconstruction process, can be performed after we difine the candidates. Further, these methods does not work well for large 3D high-resolution CT. This disadvantage corresponds with the morphological method.

(3) The difficulty of the segmentation of the peripheral branches makes the segmentation result incomplete. Due to the low contrast of the intensity between the peripheral airway regions and airway wall. Detection of peripheral bronchus branches and the reduction of the FP regions in the parenchyma regions remain the main problems in an airway segmentation method. To extract the peripheral bronchi branches, the local intensity filters are applied to filter the candidate airway regions. Due to the partial

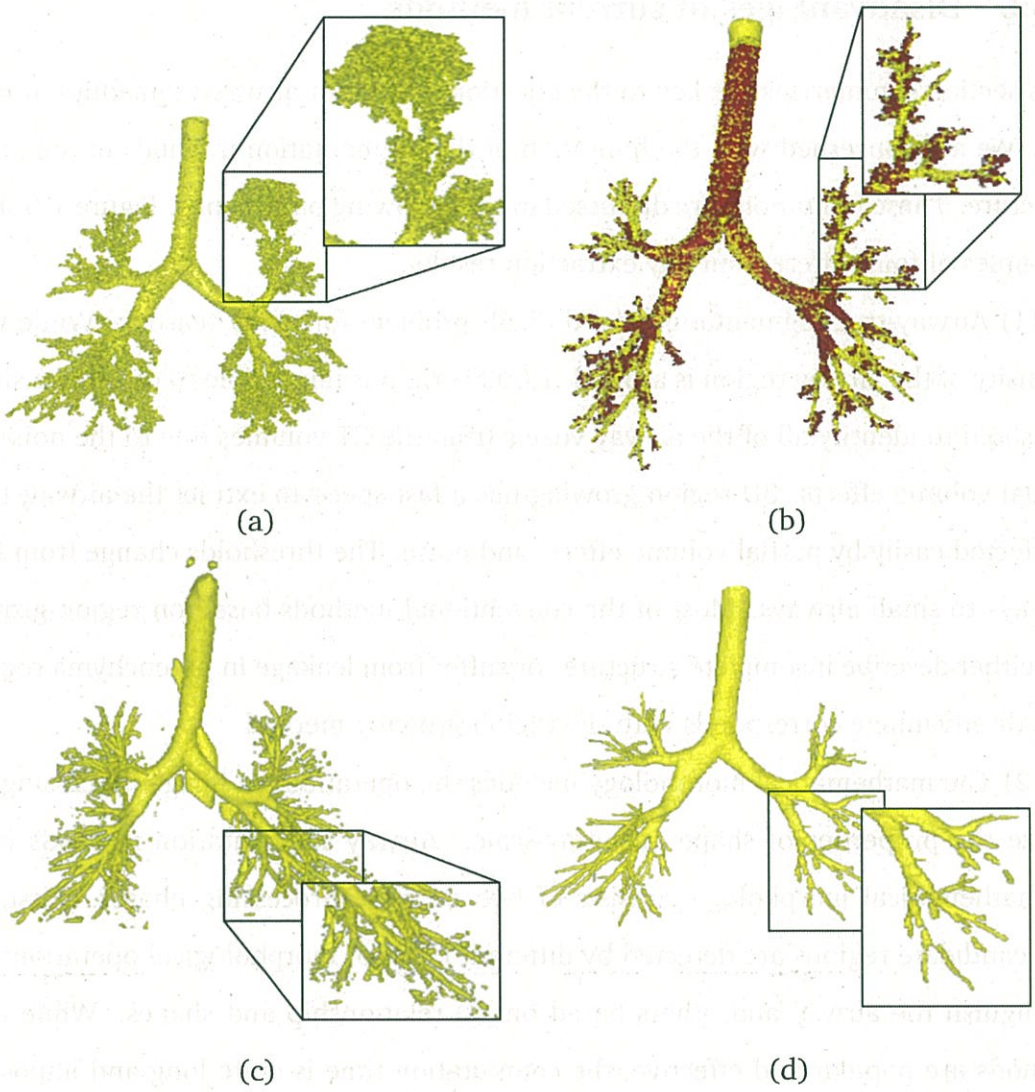

Figure 1.6: Results of different airway segmentation algorithms. (a) shows the airway segmentation result with leakage, (b) shows the airway segmentation result of local intensity filter-based algorithm, (c) shows the airway segmentation result of deep learning-based algorithm, and (d) shows the result of machine learning-based algorithm.

volume effects, the local intensity filters extract lots of false positive regions as well as the airway regions. Although the local intensity filters can detect the small bronchi regions effectively, many false positive regions over the lung area are yielded unavoidably. This disadvantage corresponds with the knowledge-based method and template matching-based method.

(4) The current learning-based segmentation methods usually have good performance on segmentation, but not on airway segmentation. Different features were extracted in the learning phase. To obtain good performance on airway segmentation, it is necessary to train the classifier by decades of ground-truth data. However, obtaining a complete airway tree is tedious and time consuming work. At the same time, to find effective features is also hard. However, the ineffective extracted branches or inappropriate reduced branches are unavoidable due to inappropriate selection of features. However, the deep learning technique can extract the proper feature effectively. But it is difficult to obtain the precise segmentation result by directly using the deep learning technique due to the low intensity contrast between the airway regions and the parenchyma regions. This disadvantage corresponds with the learning-based method.

1.6 Current status of airway segmentation

Although airway segmentation was developed several decades ago, its diagnostic and therapeutic moralities have been somewhat limited simply to increase clinical application of diagnoses and treatment of pulmonary diseases. The main reason is the difficulties of guaranteeing a high detection rate and low false positive rate. Without integrated and accurate segmentation results of the airway, it is difficult to provide the precise location and orientation for the bronchoscopy navigation while significantly improving its ability to localize target regions, to sample diagnostic tissues, and to prohibit unnecessary surgical interventions in diagnosis and staging of lung cancer [14].

This section reviews current state-of-the-art developments in airway segmentation, including filter-based airway segmentation techniques, volume of interest-based airway segmentation technique and deep learning-based airway segmentation technique. All of these techniques resulted in increased segmentation rate and decreased false positive rate.

1.6.1 Filter and machine learning-based airway segmentation

Filter-based airway segmentation uses the enhancement filter to process all of the voxels in the lung region. Yano et al. [60] presented a method to extract the airway regions in the lung area that is based on Hessian analysis and Radial reach filter to select the candidate airway regions. This method can segment the bronchus region utilizing the local intensity structure filters, CT intensity distribution and features of shape. First, this method extracts line-like structures using the Hessian matrix. This is done for local intensity structure analysis. Second, tube structures is extracted using a modified Radial Reach Filter (RRF) [60]. This method can extract many candidate airway regions but generate lots of false positive regions meanwhile.

1.6.2 Volume of interest-based airway segmentation

Since lung diseases commonly involve bronchial airway structures and morphology, airway segmentation out of chest CT volumes is now widely used in computer-aided diagnosis and surgery assistance systems. However, due to the complex tree-like structure of the airways, obtaining segmentation results with high accuracy for a complete 3D airway structure remains challenging. An airway segmentation method based on volume of interest from 3D chest CT volumes was proposed. Kitasaka et al. [53] proposed a method that uses the 3D region growing method within the volume of interest to extract the airway region. Tschirren et al. [56] proposed an airway segmentation method using a cylinder region to process the segmentation. This method extract the airway region using fuzzy connectivity within the cylinder region. These methods can extract the complete airway branches.

1.6.3 Deep learning-based airway segmentation

Airway segmentation plays an important role in analyzing chest computed tomography (CT) volumes such as lung cancer detection, emphysema diagnosis, and surgical navigation. However, due to the complex tree-like structure of the airways, obtaining

segmentation results with high accuracy for a complete 3D airway extraction remains a challenging task. In recent years, deep learning-based methods, especially fully convolutional networks (FCN), have improved the state-of-the-art in many segmentation tasks. 3D U-Net is an example that is optimized for 3D biomedical imaging. It consists of the encoder part to study the input volume and a decoder part to obtain the complete 3D segmentation results. While 3D U-Net can be trained for any 3D segmentation task, its direct application to airway segmentation is challenging due to differently sized airway branches. Charbonnier proposed a method that removes the leakage in the airway segmentation result by using CNN. This method can decrease the false positive in the airway segmentation result.

1.7 Organization of this dissertation

Our research aims to develop an airway segmentation method. This dissertation introduces three topics of our research: 1) Automatic segmentation of airway tree based on local intensity analysis; 2) Automatic segmentation of airway tree based on volume of interest; 3) Automatic segmentation of airway tree based on deep learning technique.

In the thesis, we aim to improve airway segmentation performance by increasing the segmentation accuracy and decrease the false positive rate. This dissertation consists of five chapters.

Chapter 1 introduces the background of our research. The main medical background including the anatomy of lung structure and bronchus structure, the CAD system used for airway segmentation, and the history of the airway segmentation method are introduced.

Chapter 2 introduces the airway segmentation method based on the local intensity analysis and machine learning technique. This proposed segmentation method is composed of three steps. First, Hessian analysis is utilized to enhance the tube-like structure in CT volumes, then an adaptive multi-scale cavity-enhancement filter is employed to detect the cavity-like structure with different radii. In the second step, support vector

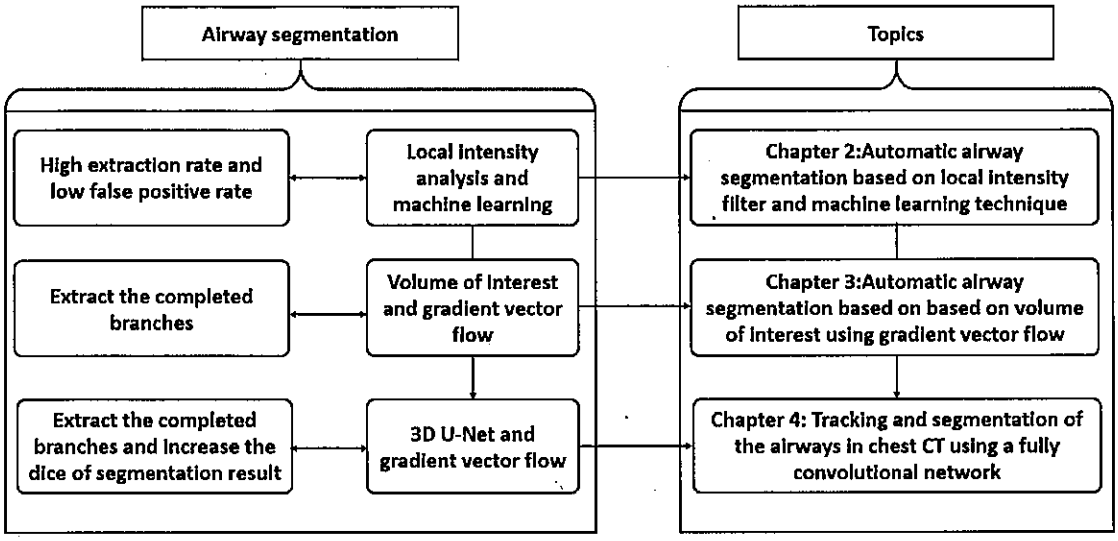

Figure 1.7: General research scope of each proposed methodology for airway segmentation.

machine (SVM) learning will be utilized to remove the false positive (FP) regions from the result obtained in the previous step. Finally, the graph-cut algorithm is used to refine the candidate voxels to form an integrated airway tree. This proposed method can solve the problem of extracting the peripheral bronchi branches.

Chapter 3 introduces a new airway segmentation method from 3D chest CT volumes based on the volume of interest (VOI) using gradient vector flow (GVF). This method segments the bronchial regions by using a cavity enhancement filter (CEF) to trace the bronchial tree structure from the trachea and utilizes the CEF in the VOI to segment each branch. Furthermore, a tubular-likeness function based on GVF and the GVF magnitude map in each VOI assists the predictions of both the positions and the directions of the child branches. After fixing the position and direction of each child branch, we continue extracting the airway branches in the VOI. At the same time, we perform a leakage detection procedure calculating both the pixel and the shape information of the extracted airway candidate regions to avoid the leakage in each VOI. Finally, we unify all of the extracted bronchial regions to form an integrated airway tree. We used a test data-set that includes 50 standard-dose human chest CT volumes to evaluate our

proposed method. The average extraction rate was approximately 78.1% with the significantly decreased FP rate. This proposed method can solve the problem of extracting the connected bronchi branches.

Chapter 4 introduces a novel methodology for the automatic segmentation of the airway tree based on deep learning technique and the airway tracking algorithm. In this work, we combine 3D deep learning with image-based tracking automatically extract the airways. We apply the airway tracking algorithm by using an adaptive cuboidal volume of interest (VOI) analysis using a 3D U-Net. All of the extracted candidate airway regions are unified to form an integrated airway tree. The proposed method can increase the airway segmentation extraction rate by using 3D U-Net and also avoid the false positive regions using the airway tracking algorithm.

In chapter 5, we conclude this thesis work on airway segmentation. We summarize limitations of the proposed method. Future work and future research directions are discussed for further development of airway segmentation algorithms. The research flowchart of this thesis is shown in the right side of Figure 1.7.

Chapter 2

Automatic airway segmentation based on local intensity filter and machine learning technique

Airway segmentation plays an important role in analyzing chest computed tomography (CT) volumes for computerized lung cancer detection, emphysema diagnosis, and pre- and intra-operative bronchoscope navigation. This proposed segmentation method is composed of three steps. First, Hessian analysis is utilized to enhance the tube-like structure in CT volumes, then an adaptive multiscale cavity-enhancement filter is employed to detect the cavity-like structure with different radii. In the second step, support vector machine (SVM) learning will be utilized to remove the false positive (FP) regions from the result obtained in the previous step. Finally, the graph-cut algorithm is used to refine the candidate voxels to form an integrated airway tree. The proposed method mainly corresponds to our journal paper "Automatic segmentation of airway tree based on local intensity filter and machine learning technique in 3D chest CT volume" that was published in **International Journal of Computer Assisted Radiology and Surgery** [in English].

The main purpose of this method is to improve the segmentation accuracy of airway tree from the 3D chest CT volumes and decrease the false positive regions during the segmentation. For the segmentation, we focus on:

(1) Segmentation of the airway tree with high accuracy.

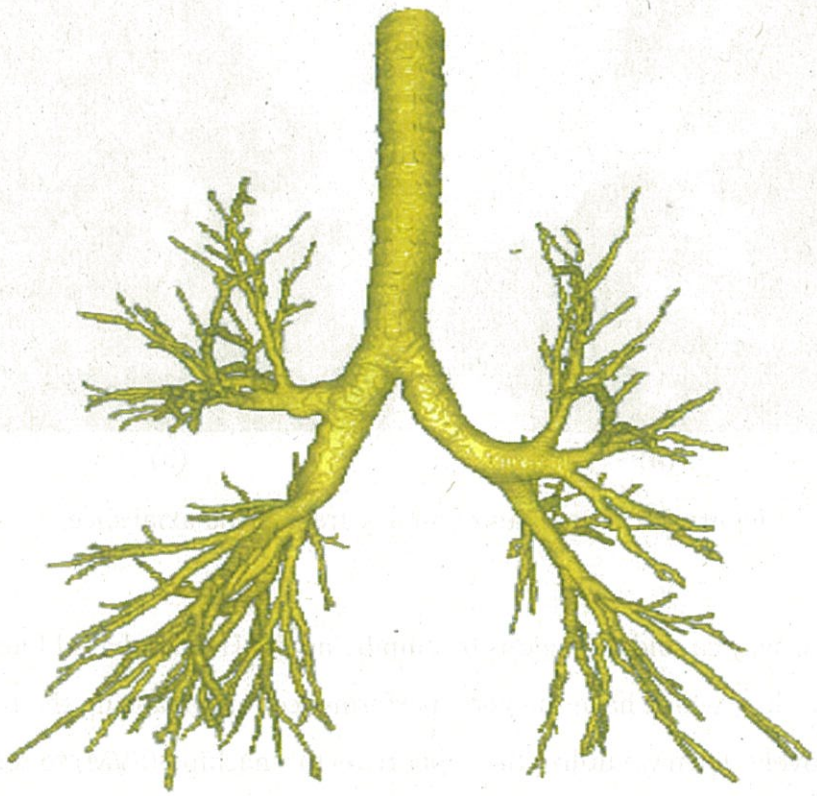

Figure 2.1: Volume rendering of one example of airway tree segmentation result.

(2) Reduction of the FPs generated during the segmentation procedure.

Figure 2.1 shows the volume rendering result of an airway tree. An integrated airway tree is composed of trachea, principle bronchus, and some peripheral bronchi. To extract the peripheral bronchi branches is challenging. The FPs of an airway segmentation method are mainly generated in the regions among the blood vessels and the bronchus wall. Figure shows the examples of the axiel slices of the airway regions. In Fig. 2.2, the red arrows point to the airway regions, and the green arrow points to the airway peripheral regions. Since they show very similar features such as shape intensity in CT scans, to reduce the FPs in airway segmentation result is challenging.

To handle the above problems and to achieve the purpose, the proposed method

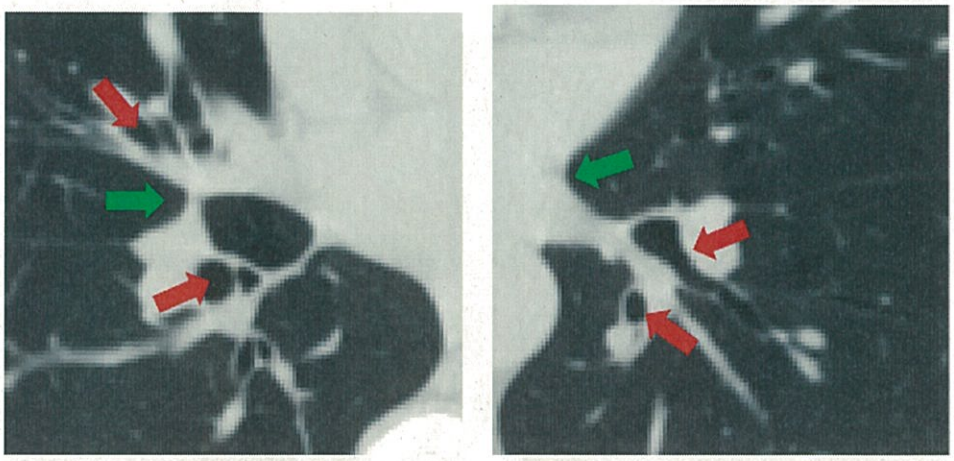

(a) (b)

Figure 2.2: Examples of airway tree on the axial slice.

segment the airway candidate regions by employing the Hessian-based filter and cavity enhancement filter, which have the good performance for enhancing the tubular structures, respectively. Then we utilize the support vector machine (SVM) to reduce the FPs obtained in the airway candidate regions. Finally, we use the graph-cut algorithm to refine all of the candidate region to form an integrated airway tree.

2.1 Introduction

According to the Chapter 1, the segmentation of airway from CT volume is very difficult and complicated. Limited image intensity distribution and increased noise results in instability of intensity in the airway lumen. Furthermore, leakage into the lung parenchyma during the procedure of segmentation often occurs due to the low contrast between the intensity of the air and the lung parenchyma. At the same time, the regions among the bronchus wall and pulmonary blood vessels have a similar intensity value distribution to the airway region. This will result in false positive regions, and this attribution will affect the extraction result.

Many studies have focused on the automated bronchus recognition from 3D chest CT volumes. Lo et al. [2] summarized airway segmentation methods through the

challenge called EXACT09. It shows various algorithms of airway tree segmentation. The 3D region-growing algorithm [24, 54, 65, 66] is the most commonly and widely used method in airway tree segmentation. This is a basic and simple segmentation method that makes use of the threshold value in the CT image and does not require prior knowledge of the airways such as shape, size and direction of small bronchi. Mori et al. [65], Kitasaka et al. [67], Tschirren et al. [56] and Feuerstein et al. [68] used region growing-based methods that adjusted a suitable threshold value to extract the airway regions. Schlathoelter et al. [69] accomplished airway segmentation based on the front propagation method. Lo et al. [59] introduced a method for segmenting the airway regions from 3D CT volumes using the trained airway appearance model, airway orientation information and region-growing method. However, the region growing-based methods can often suffer from leakages due to the low contrast in the peripheral branches, though the region-growing method is effective for extracting the large airway branches including the trachea and principle bronchi.

To avoid and reduce the leakages in the airway tree segmentation result, some researchers developed a classification-based method. Lo et al. [58] used a k-NN classifier that is trained to differentiate between airway and non-airway voxels and then utilized the region growing to finish the airway segmentation. This method can avoid the leakage effectively, but it failed to extract the small bronchi.

To track the smaller bronchi, the tube enhancement filter method is introduced here. Many studies have taken this approach recently. Yano et al. [60] proposed a method that utilizes the tube enhancement filter based on local intensity structure to detect the candidate bronchial regions. This method can detect small bronchi location effectively, but many false positive regions over the lung area are yielded unavoidably.

In this chapter, we propose a method that takes into account the tube detection filter, machine learning, and graph cut to extract the airway region precisely while reducing the FP regions. This method considers the CT image intensity and cavity-like structure in the CT volume to track and detect the candidate airway regions. It utilizes two types of tube enhancement filters to detect the possible candidate airway regions in the 3D CT

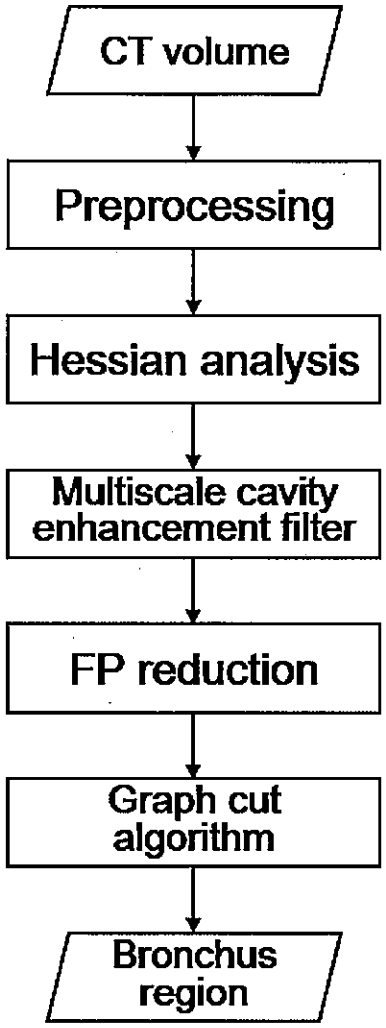

Figure 2.3: Flowchart of proposed method

volume. After that, a classifier is built to classify the appropriate candidates and delete the FP regions using the statistical values of image intensity and shape information such as eigenvalues of the Hessian matrix as the feature. Finally, we use the graph cut algorithm to refine all of the candidate voxels obtained from the previous steps to form an integrated bronchial tree. In the experiments, 50 cases are used for evaluation of our proposed method. Detection performance and FP rate are both used for comparison with the previous method. This chapter is an extension of work that was published in a

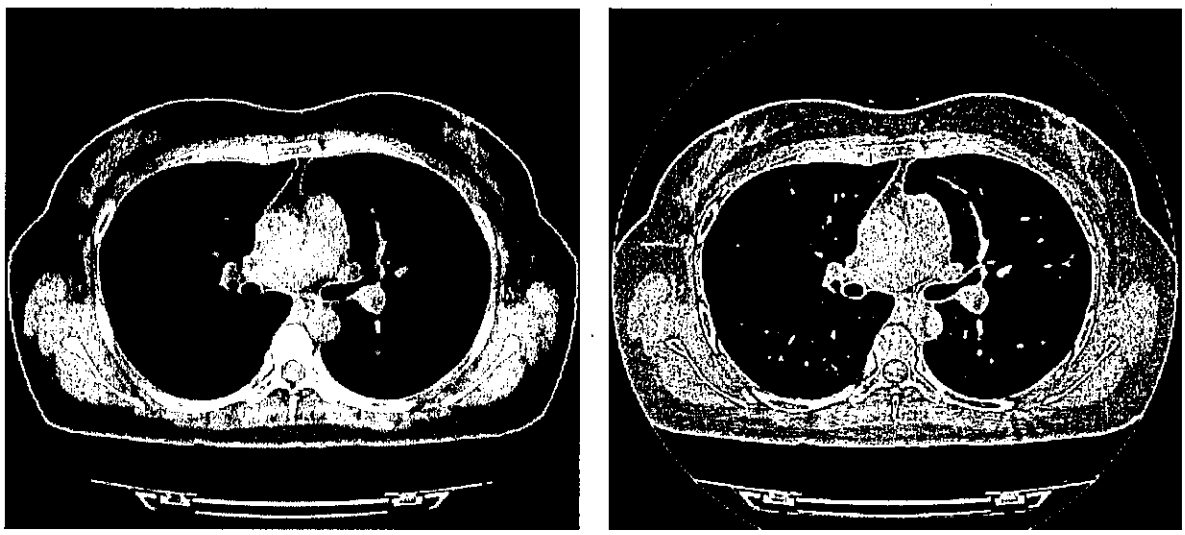

(a) (b)

Figure 2.4: Preprocessing procedure. (a) axial slice of thest CT volume. (b) output of sharpening filter.

previous conference paper [70, 71].

2.2 Method

2.2.1 Overview

Figure 2.3 shows the flowchart of our proposed method, which consists of four main phases to segment an integrated airway tree from an input 3D chest CT volume. (1) Preprocessing: initially, the unsharped mask filter [23] is utilized to sharpen the input volume and reduce the noise in the CT volumes, so that a precise result can be obtained. (2) Hessian analysis and adaptive multiscale cavity enhancement filter (CEF): two different kinds of filters based on local intensity information are employed to enhance the regions with tube-like and cavity-like structures where low intensity lumen is surrounded by higher intensity bronchus wall. (3) FP reduction: Support Vector Machine (SVM) is utilized to classify the candidate voxels and remove the false positives. (4) Final refinement: a graph-cut algorithm is used for refining all of candidate voxels extracted. Detailed information on each step is given below.

2.2.2 Preprocessing

The input CT volume is generally very noisy, and in order to obtain segmentation results with higher accuracy, it is important to sharpen the input image. To this end, we applied an unsharp mask filter with standard deviation σ to the input images [67]. This can significantly reduce the noise and enhance the bronchial walls, especially bronchial walls of thinner bronchial branches. The sharpening procedure can be formulated as:

$$\mathbf{G} = \mathbf{F} - wLoG\left(\mathbf{F}\right), \tag{2.1}$$

where $\mathbf{F}$ and $\mathbf{G}$ are the input and output images respectively, w is a weight that is used to control the effects of the sharpening operation. Figure 2.4 shows the results of the preprocessing step.

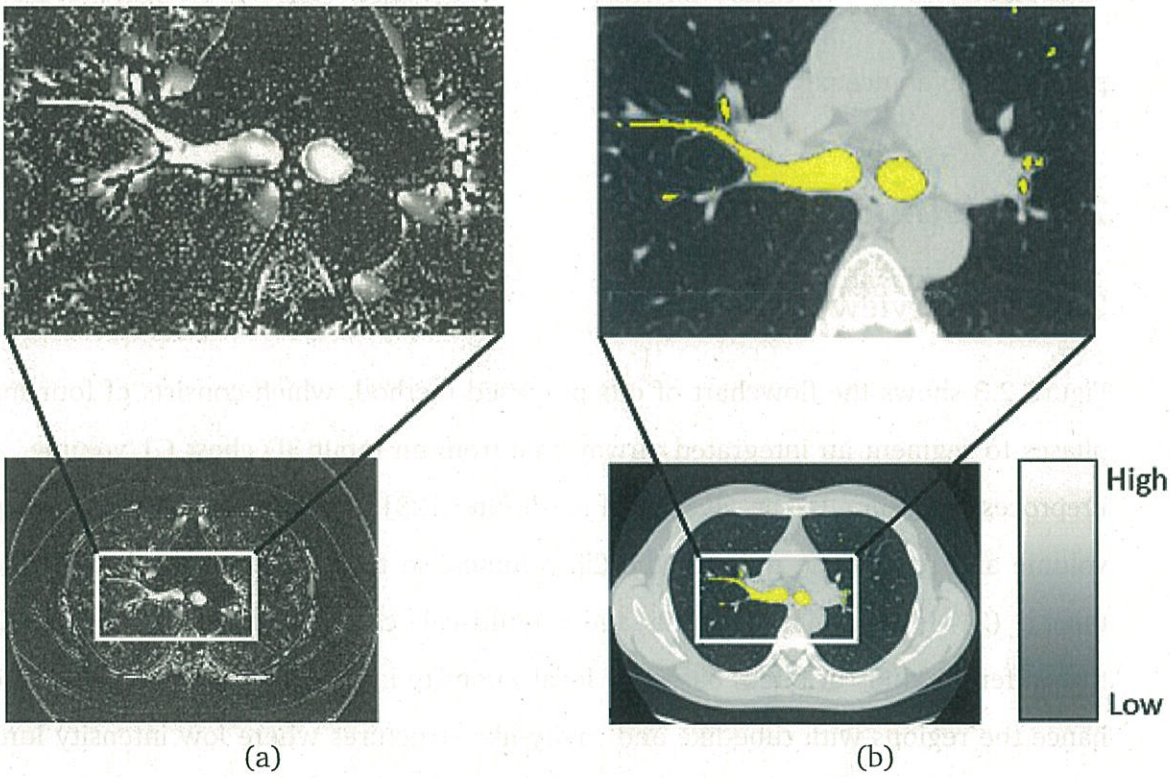

Figure 2.5: Example results of tube enhancement filter. (a) Output of tube enhancement filter. Thinner bronchial regions are obviously enhanced. (b) Bronchus region manually painted overlapping a CT axial slice.

2.2.3 Local intensity structures analysis

The airway region shows the following characteristics in the CT volumes : (1) low-intensity luminal area in the center, (2) relatively higher intensity in the bronchial wall region, and (3) tube-like structure. We enhance the voxels that belong to the tube-like structure by investigating the voxels by computing the Hessian matrix of the intensity value of every voxel in a local region. The Hessian matrix is defined as second order partial derivatives along three directions (x, y, and z) of the Gaussian function of the CT volume intensity [72]. In the following equations, $\mathbf{p}$ is a voxel in the chest CT, and $f(\mathbf{p})$ is the CT intensity value at a voxel of $\mathbf{p}$. $G(\mathbf{p},\sigma_h)$ is the Gaussian function with the deviation of σ_h, and the Hessian matrix is shown as:

$$\mathbf{H} = \begin{bmatrix} \frac{\partial^2 I}{\partial x^2}(i,j,k) & \frac{\partial^2 I}{\partial x \partial y}(i,j,k) & \frac{\partial^2 I}{\partial x \partial z}(i,j,k) \\ \frac{\partial^2 I}{\partial y \partial x}(i,j,k) & \frac{\partial^2 I}{\partial y^2}(i,j,k) & \frac{\partial^2 I}{\partial y \partial z}(i,j,k) \\ \frac{\partial^2 I}{\partial z \partial x}(i,j,k) & \frac{\partial^2 I}{\partial z \partial y}(i,j,k) & \frac{\partial^2 I}{\partial z^2}(i,j,k) \end{bmatrix}, \tag{2.2}$$

$$I_{xx} = \left\{ \frac{\partial^2}{\partial x^2} G(\mathbf{p}, \sigma_h) \right\} \times f(\mathbf{p}). \tag{2.3}$$

If the eigenvalues of $\mathbf{H}$ at voxel (x,y,z) satisfy the condition $\lambda_3 \cong \lambda_2 \geq \lambda_1 \cong 0$, then this voxel belongs to a tube-like structure. Sato [73] proposed a tube enhancement filter based on all three eigenvalues, which is given by:

$$S_{tube(i,j,k)} = \begin{cases} |\lambda_3| \cdot \psi(\lambda_2;\lambda_3) \cdot \omega(\lambda_1;\lambda_2), & \lambda_3 \geq \lambda_2 > 0 \\ 0, & otherwise, \end{cases} \tag{2.4}$$

where λ_3 controls the magnitude of S_{tube}, and $\psi(\lambda_2;\lambda_3)$ and $\omega(\lambda_1;\lambda_2)$ are defined as

$$\psi(\lambda_2;\lambda_3) = \begin{cases} \left(\frac{\lambda_2}{\lambda_3}\right)^{\mu}, & \lambda_3 \geq \lambda_2 > 0 \\ 0, & otherwise, \end{cases} \tag{2.5}$$

and

$$\omega(\lambda_1,\lambda_2)=\begin{cases}\left(1+\frac{\lambda_1}{|\lambda_2|}\right)^{\mu}, & \lambda_2\geq\lambda_1>0\\ \left(1-\alpha\frac{\lambda_1}{|\lambda_2|}\right)^{\mu}, & \frac{|\lambda_2|}{\alpha}<\lambda_1<0\\ 0, & otherwise.\end{cases} \tag{2.6}$$

S_{tube} is calculated by changing the scale σ_h. Many similar tube enhancement filters based on the Hessian matrix have been introduced in previous studies [74, 75, 76]. We choose the output of voxels defined as $l_h(\mathbf{p})$ by this filter, which has largest response at certain σ_h. Figure 2.5 shows the example of the tube enhancement filter result based on Hessian matrix analysis. We extract the bronchial candidate voxels for which $l_h(\mathbf{p}) > T_l$. It clearly shows that the thinner bronchial regions and some furcation regions of pulmonary vessels are obviously enhanced in Fig. 2.5 (a). Figure 2.5 (b) shows the ground-truth data of the bronchus region.

We extract the regions with a tube structure. However, there are many other regions extracted such as the esophagus and areas under the furcation of blood vessels, and these regions are not the bronchial region. To extract the bronchus-like structure from the 3D CT volumes, an adaptive multiscale cavity enhancement filter is employed. The extraction result from the tube enhancement filter based on Hessian analysis will then be input into the adaptive multiscale cavity enhancement filter for further airway extraction processing.

The CEF [77] is defined as:

$$g_{x,y,z} = \sum_{i,j,k\in\{-1,0,1\}} \max_{\substack{r_1=1,\ldots,R_v\\ r_2=1,\ldots,R_v}} \{L_{x,y,z}(i,j,k,r_1,r_2)-P_{x,y,z}(i,j,k,r_1,r_2)\}, s.t.\ 9k+3j+i<0 \tag{2.7}$$

$$L_{x,y,z}(i,j,k,r_1,r_2) = f_{x-ir_1,y-ir_1,z-ir_1}-2f_{x,y,z}+f_{x+ir_2,y+ir_2,z+ir_2} \tag{2.8}$$

$$P_{x,y,z}(i,j,k,r_1,r_2) = f_{x-ir_1,y-jr_1,z-kr_1}-f_{x+ir_2,y+jr_2,z+kr_2}, \tag{2.9}$$

where $f_{x,y,z}$ is the intensity value of a voxel located at (x,y,z), and $g_{x,y,z}$ is the output of CEF. Equation 2.7 expresses the definition of the CEF. Equations 2.8 and 2.9 express the first and second items in equation 2.7. Equation 2.8 is applied for computing the CT

intensity value to differentiate the voxels, and equation 2.9 is a penalty function that is used to avoid the output of CEF when a high CT intensity value exists only on one side of the voxel (x,y,z) in each direction. Set $\{(x-i,y-j,z-k)|i,j,k=0,\pm1;9k+3j+i<0\}$ is half of the 26-neighborhood of a voxel (x,y,z).

In equations 2.7-2.9, r_1 and r_2 are the radii of the filter. This filter enhances the cavity regions up to $2R$ in their diameters. Therefore, R is chosen according to the candidate airway region radius. Figure 2.6 shows the structure of CEF. In the CEF, R is set as a fixed value, which makes the CEF only sensitive to the peripheral bronchi, especially those with a small radius.

To extract the integrated airway tree, we propose an adaptive multiscale CEF. In the adaptive multiscale CEF, the parameter R is set as an adaptive one to fit the different radii in the airway tree. To determine the value of R, we need to utilize one of the parameters used in Hessian matrix analysis. In the Hessian matrix analysis process, we obtain a certain scale σ_h, which generates the corresponding largest response $l_h(\mathrm{p})$ for each voxel $\mathbf{p}$. We estimated the bronchus radius by defining a radii map, which is $R_h = 4\sigma_h$. According to the concept of CEF, the size of radius R should be bigger than the radius of the bronchi; therefore, we used $R_h + 1$ as R. In Figures 2.7 and 2.8, the output of the adaptive multiscale CEF for CT volume axial images and the corresponding 3D rendered volume have been illustrated.

Considering Fig. 2.7, one can see that the adaptive multiscale CEF will take a high value when the voxel (x,y,z) is in a cavity and a low value when no surrounding wall exists at (x,y,z). There are some black spots in Fig. 2.7(b) due to the lower value in the adaptive multiscale CEF result. The adaptive multiscale CEF output is shown in short format data, not binary data. The black spots are the adaptive multiscale CEF result taking a value lower than the CT value in the lung parenchyma, so that the black spots appear. In addition, the adaptive multiscale CEF outputs a different higher value at the air region inside the different radii of the bronchus wall according to the changed radii of this filter. The larger the radius, the higher the value output by the adaptive multiscale CEF. It is evident from Fig. 2.8 that the cavity-like regions with different

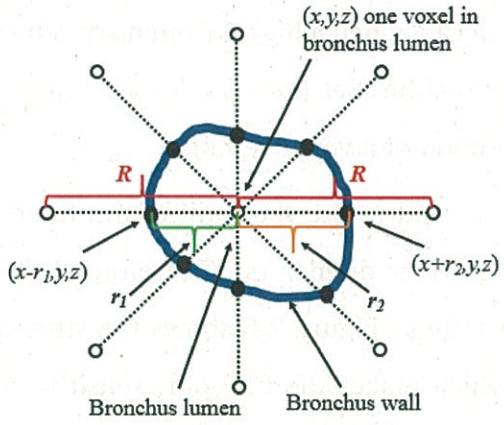

Figure 2.6: Illustration of CEF. r_1 and r_2 are the radii of the filter and R is the maximum radius used for computing the CEF.

radii can be detected effectively by the adaptive multiscale CEF. However, this gives rise to many FP regions. To reduce FPs, we use an SVM classifier, which is introduced in the next subsection.

2.2.4 FP reduction

The candidate airway regions include many false positives. To obtain an appropriate airway region, the SVM is introduced here. This technique is utilized to determine whether a voxel belongs to the true positive (TP) region or FP region. We build an SVM classifier based on the features of the local intensity and Hessian analysis eigenvalues [78]. The SVM classifier is trained in the learning step and will be used to reduce the FP regions of the extracted candidate airway regions in the testing step.

2.2.4.1 Calculation of bronchial features

We utilize 32 dimensional features to determine whether a candidate voxel is a TP or FP voxel. These features are mainly based on the local intensity structure. More detailed information about the features has been listed in Table 2.1.

The extracted features consist of both voxelwise and local regional information

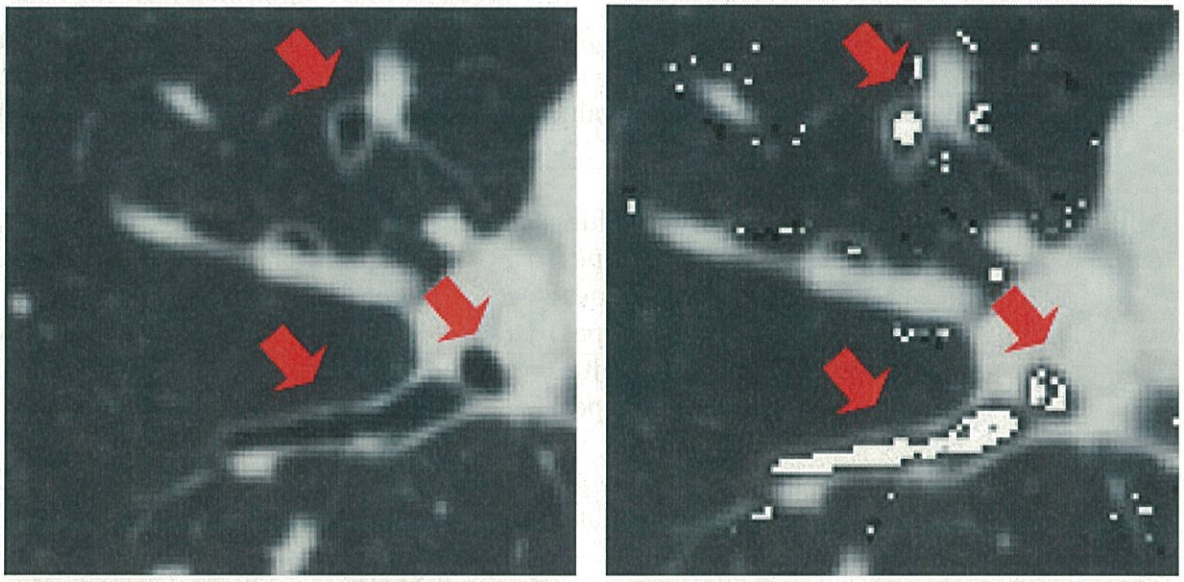

(a) (b)

Figure 2.7: Output of adaptive multiscale CEF for CT image, (a) original CT axial slice with bronchus region (b) CEF output overlapped on CT axial slice. Red arrows indicate the locations of the bronchi. Some black spots appear in (b) due to the low value of the CEF result.

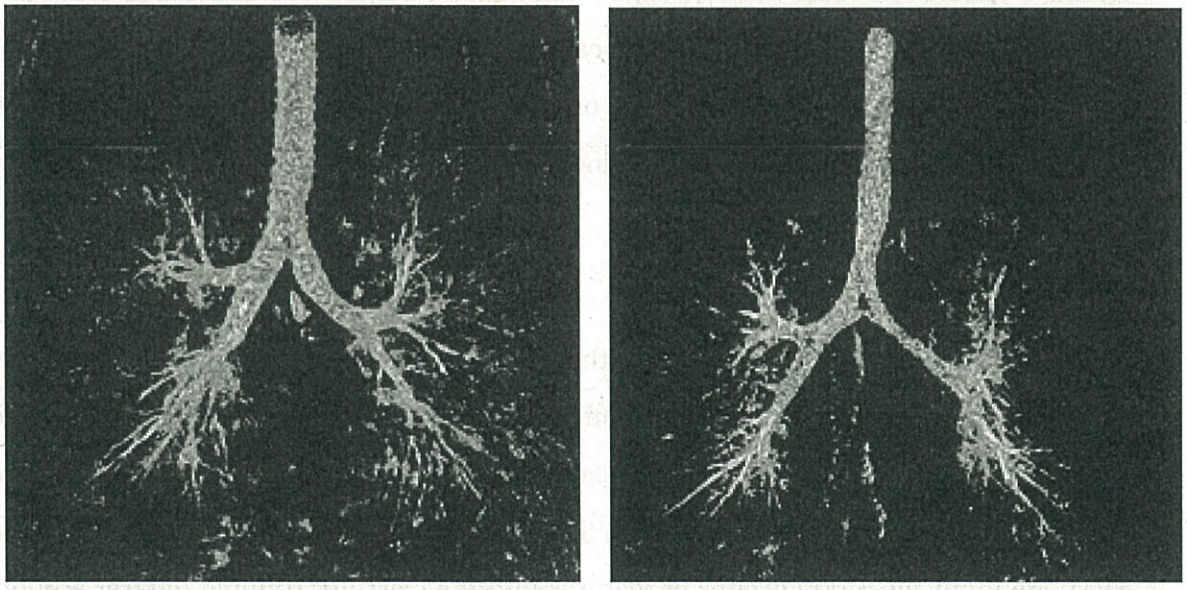

(a) (b)

Figure 2.8: Two examples of 3D rendered volume from output of adaptive multiscale CEF.

Table 2.1: Thirty-two feature values. $x_3, \ldots, x_{29}$ are intensity statistics values in local regions N_i $(i = 0, 1, 2)$. Q_1, Q_2, Q_3 are first, second and third quartile, respectively. x_{30},..., x_{32} are obtained from the eigenvalue of the Hessian matrix. Interquartile range IQR is defined as $Q_3 - Q_1$.

Type of feature values	Feature values	
n-th partial feature values (2 types)	x_1	Intensity
	x_2	Gradient
Moment statistical values (6 types)	x_{3+i}	Average
	x_{6+i}	Variance
Sequence statistical values (21 types)	x_{9+i}	Minimum
	x_{12+i}	$Q_1 - 1.5 \times \mathrm{IQR}$
	x_{15+i}	Q_1
	x_{18+i}	Q_2
	x_{21+i}	Q_3
	x_{24+i}	$Q_3 + 1.5 \times \mathrm{IQR}$
	x_{27+i}	Maximum
Shape feature values	x_{30}	λ_2
	x_{31}	λ_2 / λ_1
	x_{32}	λ_3 / λ_1

within a sphere. In Table 2.1, x_1,..., x_8 and x_{30},..., x_{32} are obtained from the voxel, and x_9,..., x_{29} are obtained from the local region, and x_{30},..., x_{32} are set based on the eigenvalues of the Hessian matrix. To obtain more effective features, three spheres, centered at the candidate voxel, are defined. (See Figure 2.9 for more information.)

2.2.4.2 Classification using SVM

Our method builds the SVM classifier with following parameters: w_{SVM} is the parameter used to adjust the imbalance of the number of positive and negative samples. C_{SVM} is the one to adjust the cost of marginal maximum. The parameter σ_{SVM} is the standard deviation of the Gaussian kernel used in SVM. LIBSVM [79] is used as an implement of SVM. We input the 1,000 groups of features into the classifier training dataset and obtain the classification model. Thereafter, we input the candidate voxels into the trained SVM classifier for classification and remove the candidates classified as FPs. In Figures 2.10 and 2.11, the flowchart of the FP reduction procedure and the result of the segmentation after FP reduction are depicted, respectively.

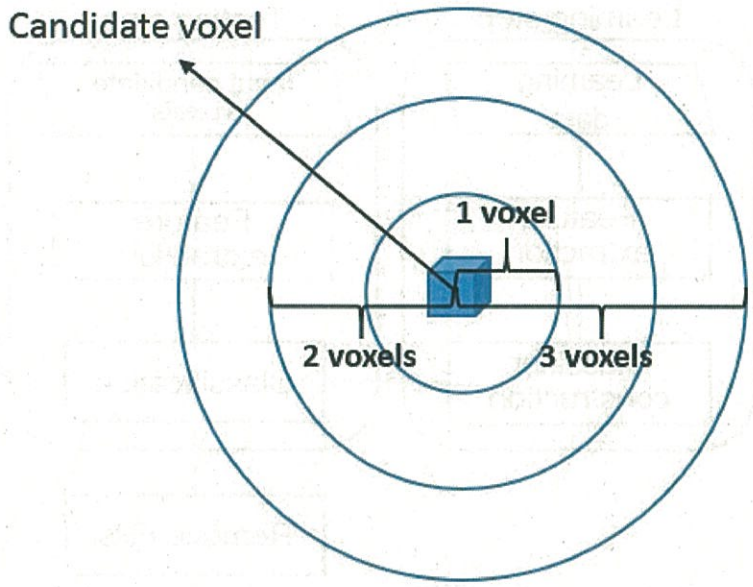

Figure 2.9: Illustration of the local region. The blue cube indicates the candidate voxel, and the area centered on this voxel shows the local region for obtaining the features.

2.2.5 Graph-cut based refinement

We perform the final segmentation process by using the graph-cut technique. The graph cut algorithm is widely used in image segmentation, because it is a powerful optimization technique that can reach the global optimum value of the specified energy function [80]. Given a set of voxels and a set of labels, $\mathcal{L}= \{0, 1\}$, the goal is to assign a label $l_p \in \mathcal{L}$ to each $p \in \mathcal{P}$. The energy function is defined as:

$$E(\mathrm{l}) = \sum_{p \in P} D_P(l_p) + \lambda \cdot \sum_{\{p,q\}} V(p, q), \tag{2.10}$$

where the first and second terms are called data term and boundary term, respectively, and λ is a constant value [81, 82]. In the airway segmentation, first, the remaining candidate voxels after FP reduction are specified as foreground p, and then the thresholded segmentation method is utilized to select the region with intensity higher than -400 H.U., which is considered as background q. Figure 2.12 shows the set of labels in the airway segmentation. In Fig. 2.12, the yellow regions are set as the foreground

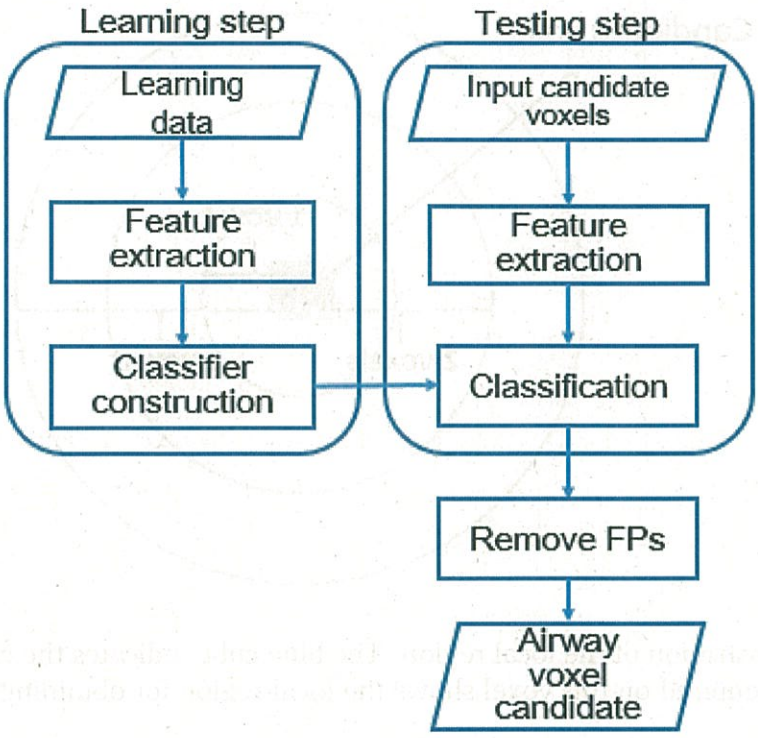

Figure 2.10: Flowchart of FP reduction. It includes the learning step and testing step in the machine learning procedure.

regions, and the red regions represent the background regions.

In the energy function, the first term is called the "data term", which expresses a penalty for assigning label l_p to voxel p. To compute this term, a probability model $P(I_p|l_p)$ is used to estimate the probabilities of the object and background. The general expression of this term is always like the negative log likelihood of the CT intensity value in the volume as follows:

$$D_P(l_p) = -lnP(I_p|l_p), \tag{2.11}$$

where $D_P(l_p)$ measures how much assigning a label l_p to voxel p disagrees with the CT volume intensity I_p.

The second term is called as the "boundary term" which represents the penalty for assigning labels l_p and l_q to the two neighboring voxels p and q, and is defined as follows:

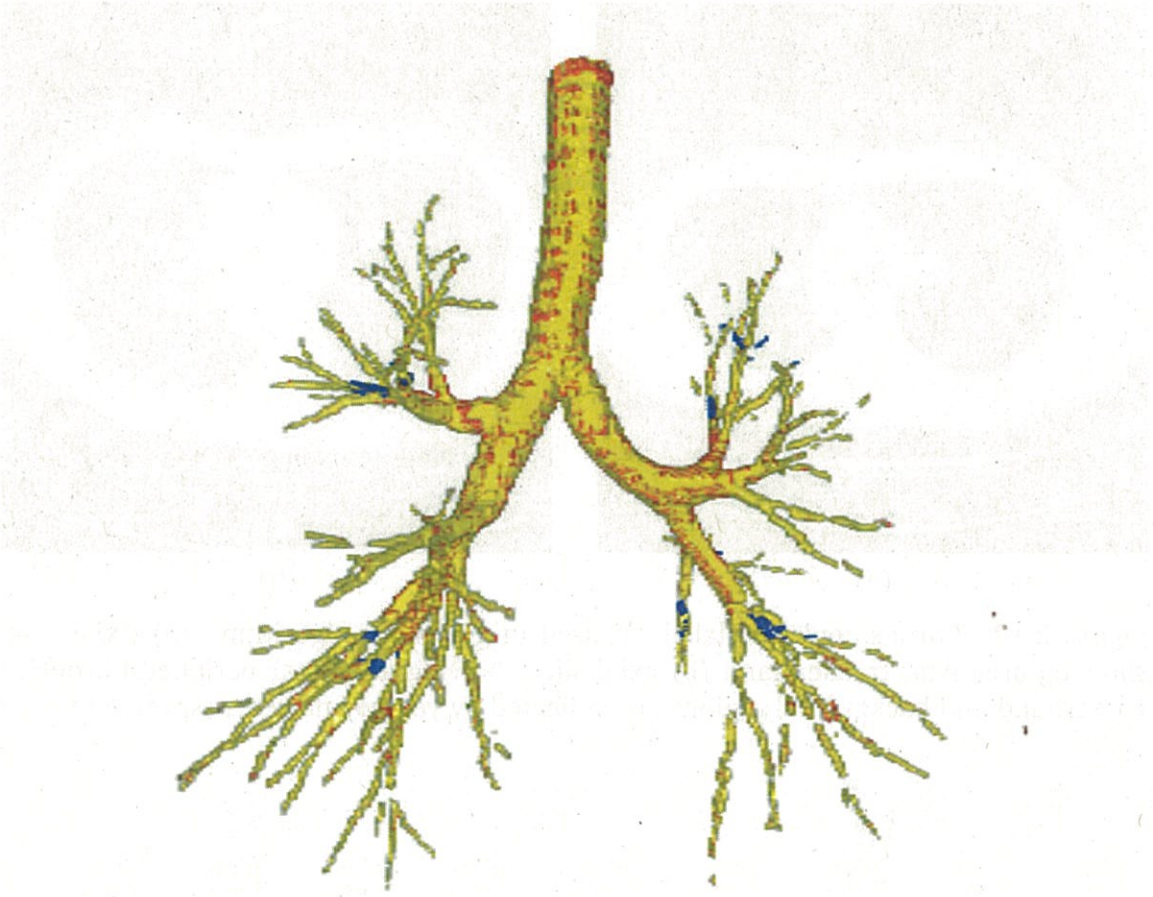

Figure 2.11: One example of segmentation result after FP reduction. Here, yellow regions, red regions and blue regions belong to TP, FP and FN regions, respectively.

$$V(l_p, l_q) = \begin{cases} \gamma & \mathrm{l}_p \neq \mathrm{l}_q \\ 0 & \mathrm{l}_p = \mathrm{l}_q \end{cases} . \tag{2.12}$$

The output of the previous step will be set as the priori knowledge as the "object" seed, and in the process of the graph cut, the voxels will be labeled according to the priori knowledge. By minimizing the energy function, we obtain the best label set l. Figure 2.13 shows one example of results using the graph cut algorithm.

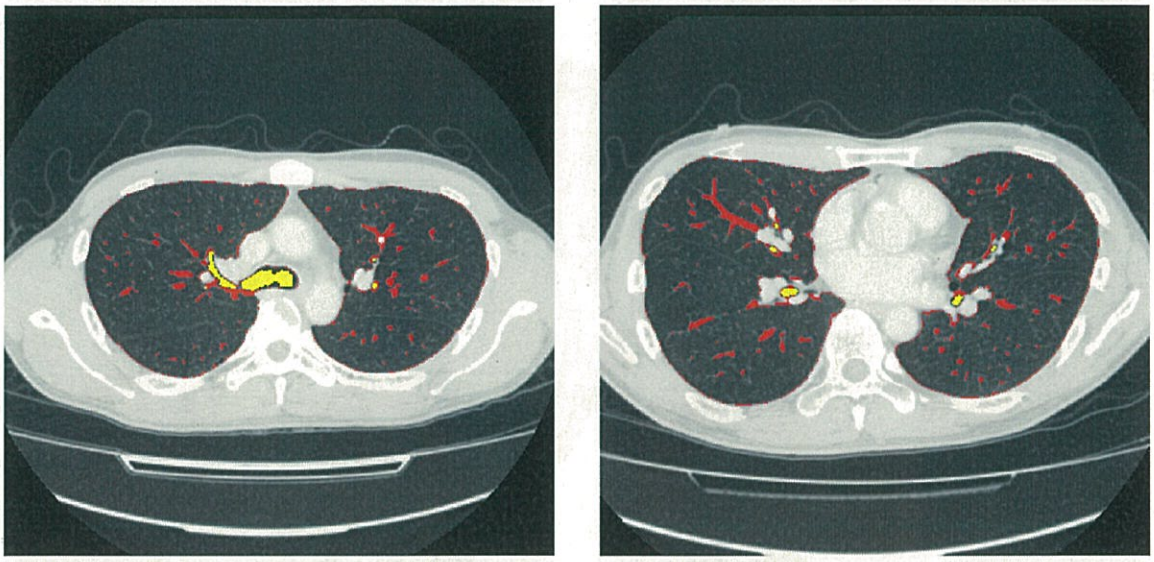

(a) (b)

Figure 2.12: Two examples of label set used in graph cut algorithm. (a) Axial slice showing area near trachea, and (b) axial slice showing area near peripheral bronchi. Foreground and background regions are indicated by yellow and red, respectively.

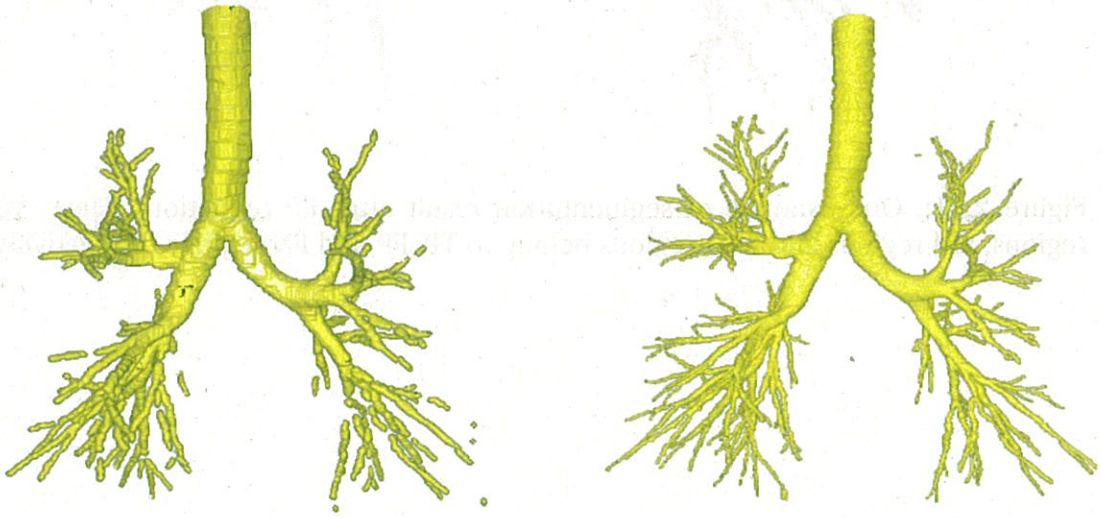

(a) (b)

Figure 2.13: (a) Example of 3D rendered from output of graph-cut, and (b) corresponding ground-truth data.

2.3 Experiments and validation

To evaluate our proposed method, we conducted an experiment using 50 clinical CT scans with standard dose provided by Tokushima University. The size of each slice

Table 2.2: Comparison between proposed method previous methods.

	Dataset 1	Dataset 2
Image size (voxels)	512×512	512×512
Number of slices	239–962	279–537
Pixel spacing (mm)	0.625–0.735	0.625–0.976
Slice spacing (mm)	0.625–1.00	0.625–1.25
Slice thickness (mm)	0.625–2.00	0.625–2.00
Tube voltage (kV)	120	120
Tube current (mA)	70–400	70–400
Convolution kernel	FC01, FC10, FC13	FC01, FC10, FC13

scan was 512×512 pixels with a pixel size in the range of 0.625 - 0.976 mm. There was a different number of slices in each dataset (ranging from 239 to 962 slices) with varying thicknesses from 0.625 to 2.00 mm. In our experiment, the dataset was divided into two groups. In the first dataset, there were 15 high-resolution cases and 10 low-resolution cases. In the second dataset, there were 13 high-resolution cases and 12 low-resolution cases. The specifications of the CT volumes in each group are shown in Table 2.2. We used the first dataset for both trainings to determine the parameters of the proposed method, and also the testing dataset for validation. The second dataset is only used as the testing dataset for validating the segmentation results based on determined parameters. The training dataset and testing dataset are decided randomly with one combination.

To obtain the training data in the machine learning phase and also for the evaluation of the experiment results, we performed manual segmentation of these 50 cases, which were leakage free. Obtaining the ground-truth data for the whole data set was extremely exhausting and time consuming. A ground-truth data was entirely obtained from hand-tracing by multiple human experts on slices. The software used for tracing is developed by the colleagues in our laboratory. Each case takes nearly one day for tracing.

Before performing the experiments, the required initialization for the existing pa-

Table 2.3: Comparison of segmentation results for airway tree in 50 chest CT examination volumes. (Note: The ground truth data was generated manually and BD indicates branch detection.)

Case	Previous method[67]					Proposed method				
	TL	TLD	BD	TPR	FPR	TL	TLD	BD	TPR	FPR
1	60.12	76.6%	99	84.6%	1.3%	68.34	84.8%	108	91.7%	0.05%
2	28.54	80.5%	65	81.3%	0.7%	32.32	87.6%	69	84.0%	0%
3	45.22	80.0%	88	67.7%	0.8%	54.34	94.9%	113	83.8%	0.1%
4	65.32	86.2%	116	67.0%	1.1%	61.58	81.3%	115	66.5%	0.15%
5	32.75	77.4%	56	68.3%	0.6%	29.52	69.8%	43	52.4%	0%
6	64.14	84.2%	87	82.9%	0.5%	58.12	76.3%	75	71.4%	0%
7	60.12	76.6%	88	75.2%	0.6%	65.78	83.8%	92	78.3%	0%
8	53.44	89.7%	101	66.0%	0.8%	55.20	92.7%	125	81.7%	0.1%
9	34.90	85.6%	75	86.2%	0.9%	29.87	62.9%	65	74.7%	0%
10	56.78	74.0%	88	78.6%	0.6%	64.89	84.4%	95	84.8%	0.1%
11	60.98	80.4%	157	72.4%	0.5%	69.98	92.3%	178	82%	0%
12	52.77	76.4%	125	81.7%	0.5%	53.77	77.8%	135	88%	0%
13	49.65	79.2%	143	79.9%	1.2%	53.26	84.9%	141	78.8%	0.1%
14	48.93	79.7%	100	69.9%	0.8%	53.77	78.6%	115	80.4%	0%
15	53.06	68.9%	125	69.1%	1.4%	59.06	76.7%	161	89.0%	0.3%
16	38.52	75.2%	41	42.3%	0.5%	44.79	87.5%	67	69.0%	0%
17	69.56	73.9%	115	67.6%	1.2%	81.49	86.6%	144	84.7%	0.2%
18	56.15	70.0%	106	56.1%	1.5%	71.66	88.9%	174	92.1%	0.2%
19	69.82	88.9%	131	69.3%	1.5%	71.86	91.5%	145	92.4%	0.1%
20	65.97	75.8%	132	61.4%	2.0%	76.13	87.4%	146	67.9%	0.1%
21	53.80	73.4%	93	61.6%	1.2%	61.49	83.9%	126	83.4%	0.1%
22	30.12	74.3%	56	75.7%	0.5%	35.75	88.2%	68	91.9%	0%
23	69.55	74.0%	133	65.5%	1.8%	81.70	87.0%	155	76.4%	0.2%
24	48.20	51.3%	105	80.0%	1.9%	70.21	74.8%	110	84.0%	0.1%
25	50.12	76.8%	89	77.4%	0.6%	53.14	81.4%	92	80.0%	0.1%
AVG1[1]	52.74	76.4%	100.6	72.2%	1.0%	62.51	90.6%	112.8	80.2%	0.08%
26	67.12	88.4%	112	89.6%	1.8%	60.98	80.3%	105	84.0%	0.1%
27	60.70	67.0%	152	80.4%	1.5%	78.24	86.3%	170	89.9%	0.2%
28	66.91	85.7%	125	89.3%	1.3%	58.37	74.8%	112	80.0%	0.1%
29	36.72	79.2%	75	84.3%	0.8%	38.59	83.3%	79	88.8%	0%
30	62.15	55.6%	105	55.0%	0.9%	68.56	61.3%	115	60.2%	0.18%
31	79.15	89.7%	172	68.8%	1.7%	70.34	79.7%	187	74.8%	0.23%
32	78.16	59.8%	169	69.5%	1.8%	85.10	65.1%	180	74.1%	0.22%
33	68.95	68.9%	120	56.6%	1.6%	76.05	76.0%	139	65.6%	0.1%
34	75.88	79.3%	176	72.1%	2.0%	81.05	84.7%	192	78.7%	0.1%
35	90.51	79.2%	175	84.5%	2.2%	98.51	86.2%	187	90.3%	0.2%
36	57.68	79.9%	67	74.4%	0.5%	65.49	90.6%	87	96.7%	0%
37	75.30	69.6%	101	57.4%	1.0%	87.25	80.6%	136	77.3%	0.1%
38	56.13	77.4%	112	78.9%	1.0%	50.08	69.2%	102	71.8%	0.1%
39	55.58	87.6%	95	66.4%	1.1%	51.27	80.8%	102	71.3%	0.15%
40	38.75	75.0%	79	77.5%	0.8%	40.20	77.8%	84	82.4%	0%
41	50.63	74.3%	103	70.1%	1.1%	60.49	88.8%	100	68.0%	0.05%
42	63.53	63.8%	136	78.6%	1.6%	87.56	87.9%	166	96.0%	0.1%
43	35.12	83.4%	69	77.5%	0.6%	38.08	90.4%	75	84.3%	0%
44	57.68	79.9%	130	74.3%	1.7%	65.49	90.6%	139	79.4%	0.15%
45	75.88	80.8%	117	55.2%	1.8%	68.12	72.5%	134	63.2%	0.1%
46	65.12	73.0%	98	64.1%	1.0%	73.37	82.3%	125	81.7%	0.1%
47	25.94	70.6%	55	68.8%	0.6%	28.28	77.0%	65	81.2%	0%
48	52.31	80.1%	114	64.4%	0.9%	58.83	90.1%	129	72.9%	0.25%
49	35.45	82.3%	47	54.0%	0.5%	38.54	89.5%	52	59.8%	0%
50	47.54	88.8%	127	80.4%	1.1%	49.66	92.8%	135	85.4%	0.1%
AVG2[2]	59.16	75.3%	113.2	72.4	1.23%	63.14	80.4%	122.2	78.3%	0.10%
TAVG[3]	55.9	75.8%	106.9	72.3	1.1%	62.83	85.2%	117.5	79.1%	0.09%

[1] The means of the measures for the training dataset.
[2] The means of the measures for the testing dataset.
[3] The means of the measures for all examinations.

Table 2.4: Average branch number, average total length, average number of generation of training data, testing data and 50 total cases for reference.

	Training dataset	Testing dataset	Total
Number of branches	140.8	154.7	148.5
Total length(cm)	78.53	69.00	73.74
Average number of generations	9.3	8.9	9.1

rameters in each phase must be done. In the pre-processing phase, where we have to use LoG, the standard deviation σ was selected as $\sigma = 0.5mm$. This parameter was chosen empirically by applying this filter with different standard deviation values to CT volumes, and we predetermined the parameter in order to reduce noise by visual inspection. Parameter ω was set according to the value of $LoG(\mathbf{p})$. If $LoG(\mathbf{p}) \leq 0$, then ω=0.5, and if $LoG(\mathbf{p})$>0, ω=0.05. In the phase of Hessian analysis, parameters μ and α were set to 1 and 0.25, respectively. The multiple scales σ_h were selected from 0.5 mm to 5 mm with the step size of 0.1 mm; therefore, there are 45 σ_h. The σ_h for which the largest region of $l_h(\mathbf{p})$ results was utilized. For an extracted candidate voxel $\mathbf{p}$, the radii map R_h of the bronchial branch was estimated corresponding to $4\sigma_h$.

The parameter R utilized in CEF was chosen according to the radii map R_h. The parameter R decides the diameters of the cavity that this filter can enhance. By selecting different values of R, the CEF can enhance the airway with different diameters. According to Eq. 2.7 and Fig. 2.6 , one can see that R is longer than the radius of the bronchus, so we defined R_h as $R_h = R + 1$. The radii map is in the range of 2-20. In the airway region, they are distributed into 2, 4, 6, 8, 10, and 20 respectively, indicating the bronchus and small bronchi with different radii. Correspondingly, the parameter R_h was defined as 3, 5, 7, 9, 11, and 21, respectively.

Candidate airway regions obtained by Hessian analysis and multiscale CEF were classified into TP and FP classes using the SVM classifier by local intensity information. In our experiment, we utilized the LIBSVM package (version 3.20). The learning conditions were determined based on the training data set as: w_{SVM}=0.25, C_{SVM}=100, and g_{SVM}=0.825. After the FP reduction, the output was inputted into the graph-cut for final refinement. As there were some remaining FP regions after applying the SVM

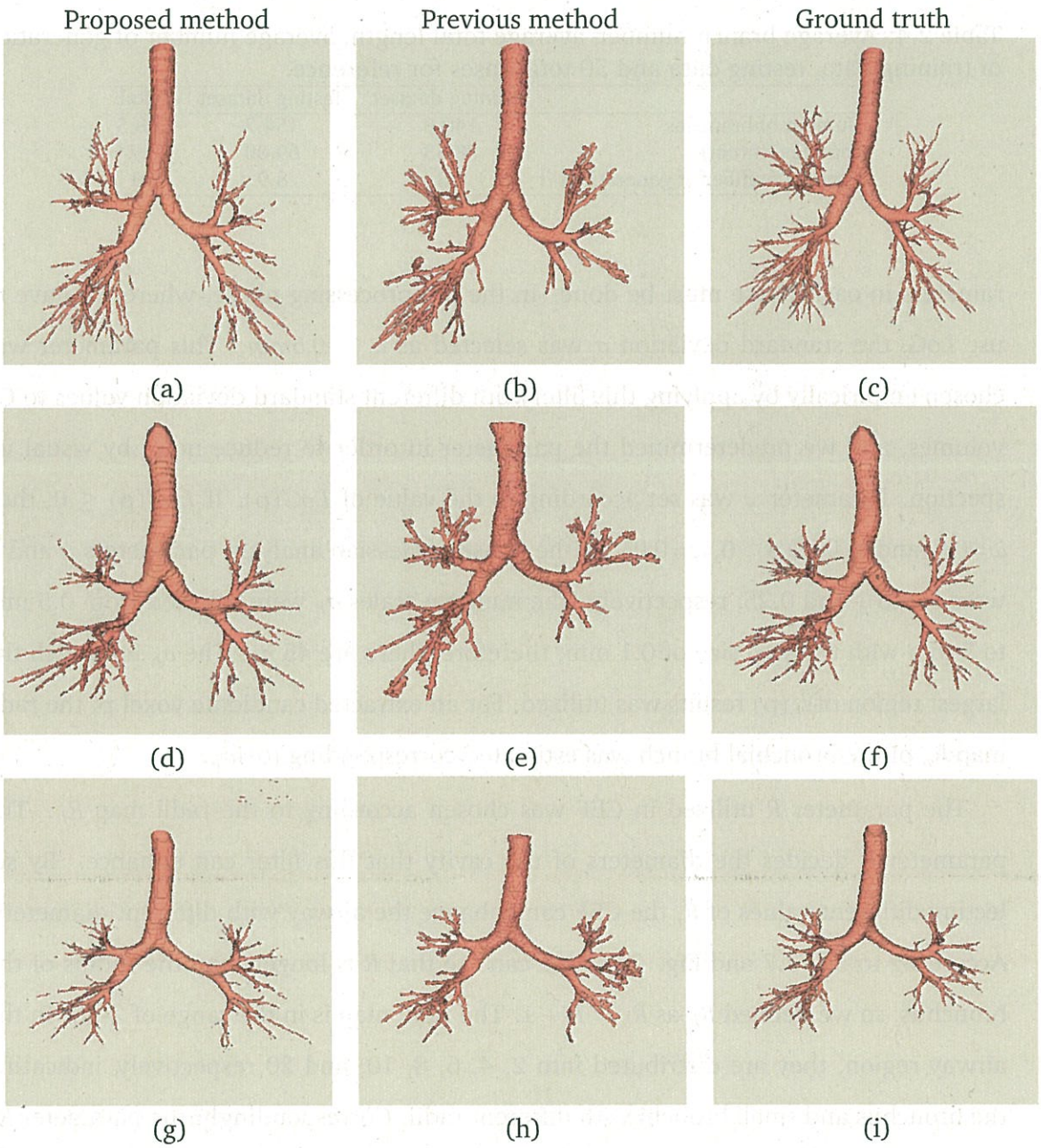

Figure 2.14: Airway extraction results: (a) to (c) good performance, (d) to (f) moderate performance, and (g) to (i) bad performance.

classifier, the accuracy of the label set used in the graph-cut is around 98.5%. The accuracy is calculated by dividing the candidate airway voxels inside the airway regions (true positive candidate airway voxels) by the whole candidate airway voxels obtained by SVM.

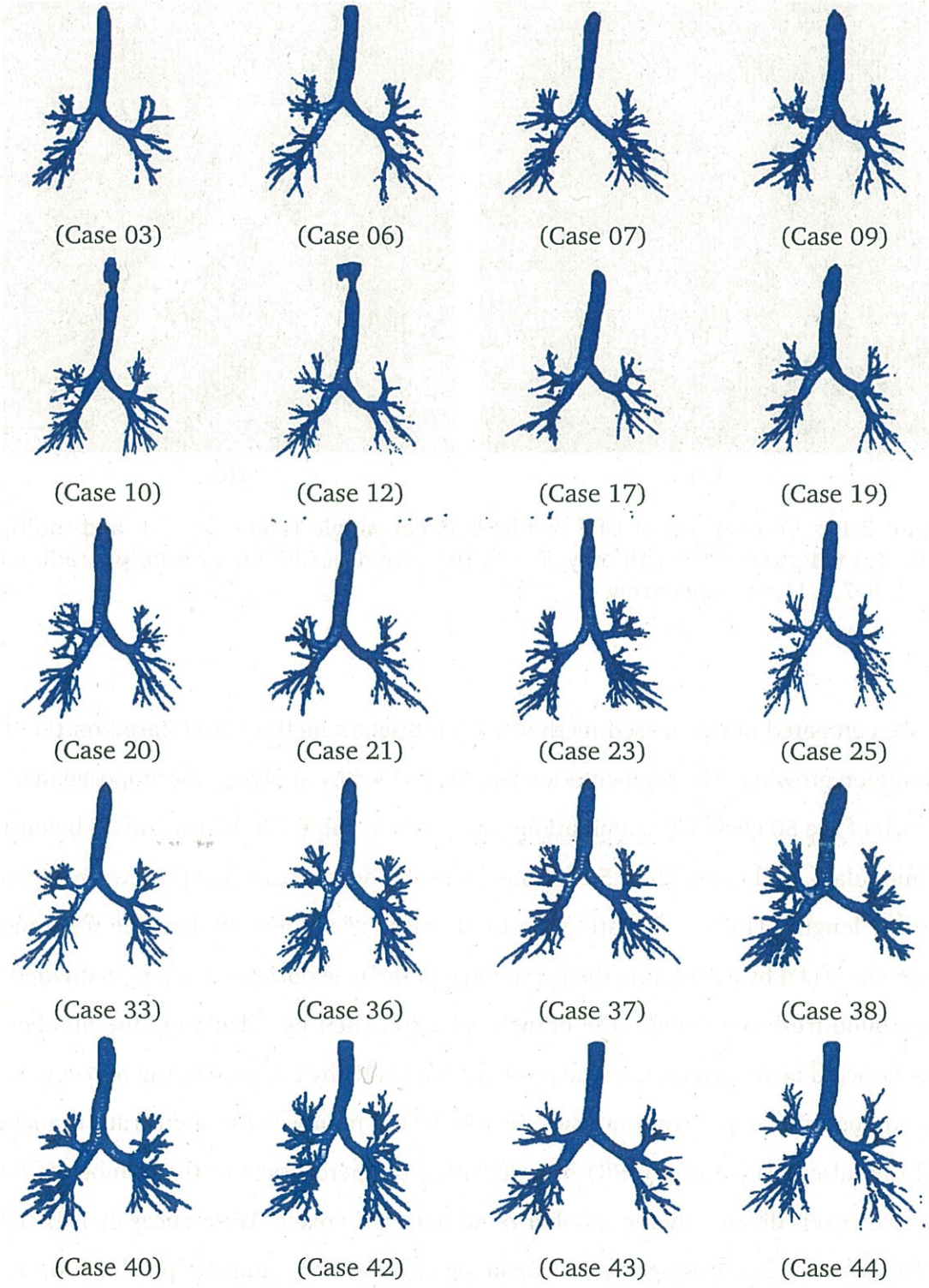

Figure 2.15: Segmentation results for the twenty cases in the test set.

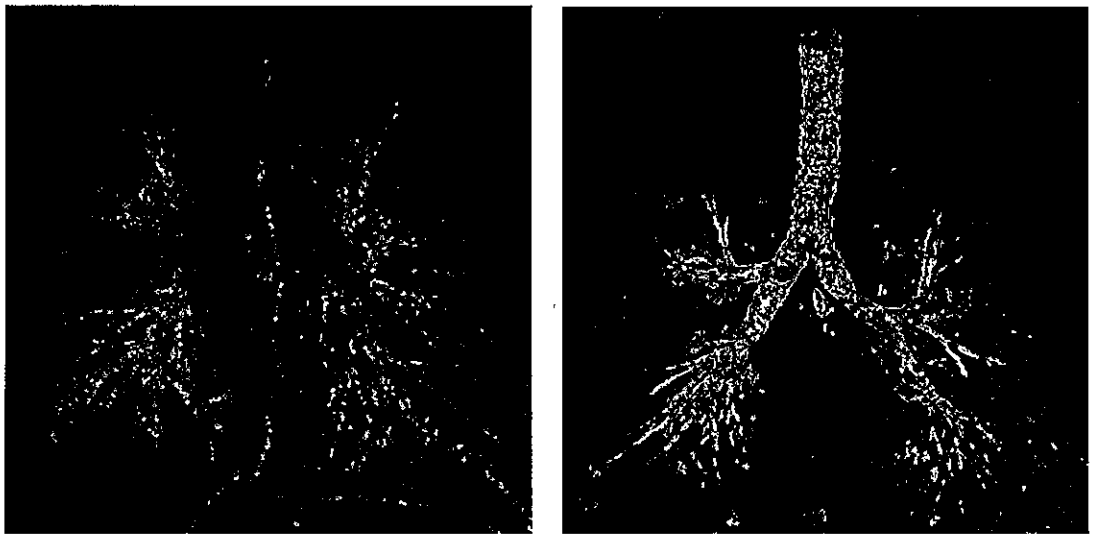

(a) (b)

Figure 2.16: Comparison of CEF results between single radius $R = 3$, and multiple radii. (a) Output of CEF with only $R = 3$, (b) output of CEF under multiple radii with $R = 3, 5, 7, 9, 11, 21$ respectively.

We compared our proposed method with Kitasaka's method [67] based on the VOI and region growing. The segmentation results, yielded by applying our proposed method to each of the 50 chest CT examinations, are given in Table 2.3. Cases 1 to 25 belong to training data, and cases 26 to 50 belong to testing data. For evaluation, we computed the tree length (TL) by calculating the total length of the airway tree, the tree length detection (TLD) by calculating the percentage of the true positive tree length divided by the ground-truth tree length, the branch detection (BD) by calculating the number of the extracted airway trees, the true positive rate (TPR) by calculating the percentage of the number of true positive branches divided by the number of ground-truth branches, and the false positive rate (FPR) by calculating the percentage of the number of false positive voxels divided by the number of all detected voxels. Differences in TLD, TPR, and FPR were tested using the Wilcoxon signed-rank test, and the p-values for TLD, TPR, and FPR are 2×10^{-3}, 1×10^{-5} and 3×10^{-5}, respectively. The significance level was set to $p \leq 0.05$. Table 2.4 shows the average branch number, average tree length and average number of generations of the ground truth in the training dataset, test-

ing dataset and total dataset for reference. Figure 2.14 gives the extraction evaluation results of the proposed method and the comparison with the previous method [67]. Furthermore, for completeness of the paper, the segmentation results of 20 cases are selected for presentation in Figure 2.15.

For the evaluation, the trachea was excluded from any measures related to branch and tree length or count. Furthermore, to measure leakage, the trachea as well as the left and right main bronchi were excluded.

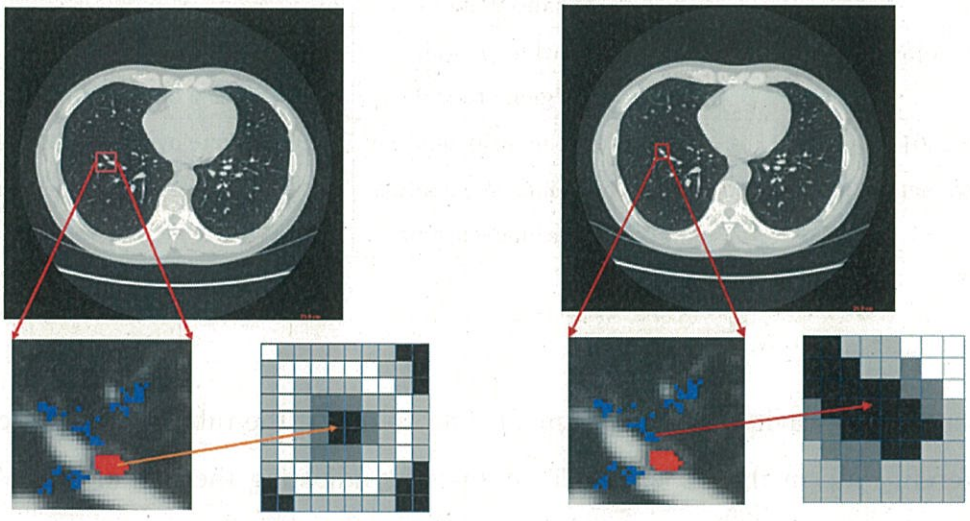

(a) (b)

Figure 2.17: CT intensity distribution of TP region and FP region. (a) Intensity distribution of the TP region, (b) intensity distribution of FP region.

2.4 Discussion

We developed a method to automatically segment the airway tree in the lung region from 3D chest CT volumes by utilizing local intensity analysis, machine learning technique and graph-cut algorithm and evaluated the performance on 50 chest CT volumes. Compared to the previous methods, our proposed method has the following advantages: 1) unlike the previous methods, this method doesn't need to trace the airway tree, and hence does not suffer from leakage. 2) Our proposed method utilized a tube-

Table 2.5: Comparison of proposed method and previous methods.

Author	Number of cases	Method	Performance
Kitasaka[67]	3	VOI region growing	6th generation per case Average for 38% detection rate
Tschirren[56]	22	region growing	27.45±3.75 branches for each case
Feuersteins[68]	20	VOI region growing	sensitivity : 76.5%
Schlathoelter[69]	1	tube-like enhancement filter	7th generation per case
Pechin Lo[59]	15	machine learning region growing	123 branches per case 51.2% detection rate
Yano[60]	4	local intensity analysis	69.5% rate averagely per case
Proposed method	50	local intensity analysis machine learning	79.1% rate averagely per case

like and multiscale cavity-like enhancement filter to detect the tubular-type structures with different radii in the 3D chest CT volumes by adjusting the parameters. Table 2.5 summarizes the performance comparison of our proposed method against other approaches based on several methods that have been developed so far. From the results, it is evident that our proposed method can extract more small bronchial branches without generating more false positive regions. To visually demonstrate the performance of our scheme, we listed a set of segmentation results from three groups: the "high", "moderate", and "poor" performance of our proposed method in Fig. 2.14. It can be seen that our proposed method can extract a more integrated airway tree than Kitasaka's method. The previous method always results in breaks in some branches and is unable to obtain an integrated airway tree; at the same time it always generates some leakage to a certain extent. Compared to these methods, our proposed method can be considered comparable to or better than most of the methods in terms of branch detection number, TPR, and tree length. As one can see in Fig. 2.14, our proposed method can extract more small bronchi branches to form an integrated airway tree.

2.4.1 Effectiveness of local intensity structure analysis

Compared to the region growing-based method, our proposed method is more sensitive to the bronchus-like structure in the lung area and does not suffer from leakage. The Hessian matrix analysis can detect the tube-like structures effectively; however, there are many tissues in the lung area with similar tube-like structure as the airway. To extract the candidate airway and remove these other areas, the adaptive multiscale CEF is utilized here. Compared to the original CEF algorithm, the adaptive multiscale CEF can detect and extract more candidate bronchi branches with different radii as shown in Figure 2.16. Table 2.6 shows the detection rate by changing the radii in the CEF from 3 to 21. The original CEF aimed to detect only the peripheral bronchi branches. From Fig. 2.16 (a), we can see that although the peripheral branch regions have been enhanced well, the trachea and principle bronchi branches are missing. According to Table 2.6 and Fig. 2.16 (b), the detection rate can be increased by adding the radius selection. The table gives the comparison of the detection rate by changing the radii in the CEF. The comparison results between adaptive multiscale CEF and CEF show that the adaptive multiscale CEF has a better performance in extracting both the principle bronchus and different-radii bronchi, which is indeed more feasible for obtaining an integrated airway tree.

2.4.2 Effectiveness of SVM classifier

From the results of the Hessian matrix analysis and adaptive multiscale CEF, it can be clearly seen that there are many FP regions around the airway tree, especially the small bronchi branches. These FP regions belong to the surrounding pulmonary tissue such as the esophagus and the areas under the furcation of blood vessels, which show a partially similar intensity structure to the bronchial region. In these FP areas, the intensity is slightly lower than the surrounding lung parenchyma, which makes them seem to be surrounded by higher intensity objects. However, these regions are not completely the same as the bronchus-like region, as shown in Figure 2.17. The bronchus-like structure

Table 2.6: Detection rate by changing the radii in multiscale CEF from 3 to 21. The detection rate is computed as the ratio between the branch number resulting from segmentation and branch number from ground-truth data.

Radius utilized in CEF	Detection rate
r = 3	53%
r = 3,5	56%
r = 3,5,7	61%
r = 3,5,7,9	69%
r = 3,5,7,9,11	73%
r = 3,5,7,9,11,21	79%

is the one with low-intensity areas surrounded by higher-intensity areas as in Fig. 2.17 (a), and FP region intensity distribution has the structure given in Fig. 2.17 (b) with the dark area partially surrounded by the higher intensity regions. Based on this differential attribute, utilizing the feature based on local intensity structure and SVM classifier, we can classify the TP region and FP region.

2.4.3 Possible improvements

Compared to Kitasaka's method, our proposed method avoids suffering from so many FP regions and seems to obtain more intact results, but in some branches, especially some peripheral ones, Kitasaka's method can extract more candidate branch regions despite suffering from some FP regions. In contrast with his method, our proposed method can extract many thin bronchi branches, but it is sometimes not sensitive enough to very small bronchi. Also, since the decisions are made for each voxel independently, small breaks and holes do occur during the segmentation procedure. These missing parts will affect the accuracy of the segmentation results to a certain extent.

The reason for missing some small peripheral airway branches involves two points: first, many thin bronchi with 1 or 2 voxels in their diameter can't be extracted by adaptive multiscale CEF due to the smallest radius R used to compute the CEF, which is set to 3, and we also gave a threshold value for selecting appropriate candidate voxels. If

we gave the parameter R a very small value, it would generate many FP regions, which would affect the final results. Second, by utilizing the SVM classifier, it is unavoidable to miss some regions that should belong to the TP region and cause some false negatives of the airway tree especially for the peripheral branches.

One way to improve our current work is to combine the local intensity structure with the VOI image. VOI is utilized to divide a given CT image into subimages that contain one part of the bronchial branch in each subimage. Each VOI subimage will be tracked along the airway running direction. The tube-enhancement filter and adaptive multiscale cavity enhancement filter will be utilized for extracting the bronchus-like structures. However, because we limit the utilization of the enhancement filters in a local region, this method can detect more small peripheral bronchial branches without suffering from many FP regions. Another approach to improve results would be to utilize the vessel segmentation result. This is because most of the peripheral bronchi are distributed near the blood vessels and have a similar tree-like structure with a pulmonary vessel tree. By localizing the detection regions, the FP region detection can be decreased.

Another drawback is that our proposed method requires a relatively long computation time. On average, the total required time for each case to segment an integrated airway tree was 4–5 hours on a single CPU with two Intel Xeon X5355 processors (2.66 GHz). Most of the time is spent on Hessian matrix analysis to select tube-like candidate voxels and SVM classifier for removing FP regions for around 2–3 hours. Other procedures such as multiscale CEF and graph-cut will take around 2 hours, respectively. In order to accelerate the computation speed, the usage of parallel processing technologies will be considered in the future.

2.5 Conclusion

This paper presented a segmentation method of an airway tree. The initial segmentation results were obtained by utilizing the enhancement filters based on local intensity

analysis. The machine learning technique is then utilized to remove the false positive regions to get more precise segmentation results. Finally, a graph-cut algorithm is utilized for refining the segmentation results. The results show that our proposed method has better performance than the state-of-the-art methods. The proposed method can extract more peripheral airway branches but the extraction result are not complete, many airway branches are disconnected. How to solve this problem is in the future work.

Chapter 3

Automatic airway segmentation based on volume of interest using gradient vector flow

In this paper, we propose a new airway segmentation method from 3D chest CT volumes based on the volume of interest (VOI) using gradient vector flow (GVF). This method segments the bronchial regions by applying a cavity enhancement filter (CEF) to trace the bronchial tree structure from the trachea and utilizes the CEF in the VOI to segment each branch. Furthermore, a tubular-likeness function based on GVF and the GVF magnitude map in each VOI assists the predictions of both the positions and the directions of the child branches. By calculating the tubular-likeness function based on GVF and the GVF magnitude map, the airway-like candidate structures can be specified and their centerlines can be extracted. Based on the extracted centerlines, we can detect the branch points of the bifurcations as well as the directions of the airway branches in the next level. At the same time, we performed a leakage detection procedure to avoid the leakage in each VOI. The leakage detection procedure analyzes both the pixel and the shape information of the extracted airway candidate regions. Finally, we unified all of the extracted bronchial regions to form an integrated airway tree. We used a test dataset that includes 50 standard-dose human chest CT volumes to evaluate our proposed method. The average extraction rate was approximately 77.90% with the significantly decreased FP rate.

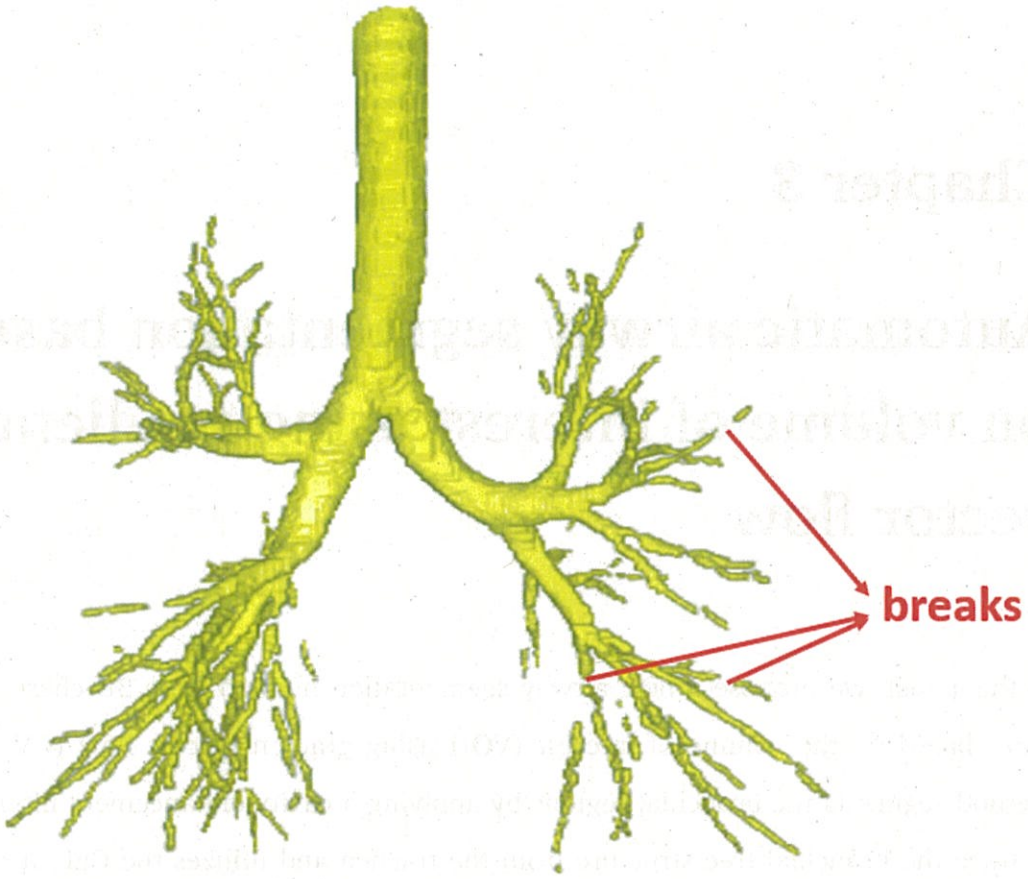

Figure 3.1: One example of the extraction result in the previous method.

The observation of organs and pulmonary tissue is very important in the inspection of the lung disease. During the inspection, the reference of the airway tree segmentation result is helpful. However, obtaining a complete airway tree from the CT volumes makes large burden tasks to a physician. This is because a CT volume usually contains hundreds of slices. Painting on each slice is time-consuming. However, in the Chapter 2, we introduce an airway segmentation method based on local intensity filters and machine learning technique. This method can detect the airway candidate regions effectively, but also cause some false negative regions meanwhile. And the drawback of the method in Chapter 2 is that this method lead to many disconnections in the bronchi branches.

These disconnections effect the inspection of disease for physicians. In order to extract the complete airway tree, the concept of volume of interest (VOI) is introduced. The airway regions are extracted volume by volume along the centerline in the airway tree. During this procedure, a leakage detection function based on shape information is used to reduce the leakage regions in each VOI. The GVF magnitude and tubular-likeness function is used to extract the centerline and detect the branching point. After detecting the branching point, the new VOI in the next level will be established according to this branching point. Finally, all of the airway regions in the VOI are integrated together to form an airway tree. Compare to the previous method, this proposed method utilize the concept of VOI to track the airway tree along the centerline, which promise the integration of the airway extraction and keep the low false positive rate meanwhile. Figure 3.1 shows one example of the volume rendering of airway extraction result. The red arrow point to the breaks in the result.

3.1 Introduction

According to Chapter 1, an airway tree often appears as circular regions in CT image slices. Identification of an integrated airway tree can be transformed by the detection of the circular regions in the 2D slices and reconstructed as a 3D airway tree. Generally, morphological methods effectively detect the shape, size, and intensity of the airways. Such methods consist of two steps: (1) detection of the candidate airway regions in the 2D slices and (2) reconstruction of the airway tree based on the detected candidate airway regions using various morphological operations. For example, Aykac et al. [24] identified the airway regions by applying a threshold to differentiate the reconstructed and original CT images to determine the local extreme. Compared with traditional morphological operations, Fetita et al. [84] proposed a mathematical morphology operator based on the concept of connection cost for a complete airway reconstruction. The connection cost considers three kinds of regions related to airways: (1) lumen, (2) airway walls, and (3) adjacent parenchyma tissue.

Some researchers have studied airway segmentation based on template matching based methods, which use a set of predefined templates (including 2D- and 3D-based ones) to detect airway regions with similar shapes. Due to the tubular shape of airways, the most commonly used templates are 2D circular based ones that are suitable to match the airway regions in each image slice[55, 85]. However, airways only appear in circular shapes in cross-sections when the airways travel perpendicular to the scanning site. Otherwise, since there is a variety of generally elliptical shapes, based on a limited number of shapes, it is difficult to use a template to fully describe the airway shapes in a cross-sectional form. To overcome the limitations of 2D airway templates, a 3D cylinder template obtained airway candidate regions that lead to more accurate results[56, 57, 86].

To capture the underlying probability map and obtain accurate airway candidate regions, machine learning-based methods have been proposed. Lo et al. [58, 87] developed a classifier that uses several image-appearance-based features and k-nearest neighbor (k-NN) classification to differentiate airway and non-airway regions from chest CT volumes at varying scales. Lo et al. [59] improved their approach by a combination of an airway appearance model with a classifier trained with uncompleted manual-traced airway tree segmentation.

Although most conventional approaches extract the main bronchus and the principal bronchi very well, their functionality fails when it comes to extracting the peripheral bronchi. To meet this requirement, the concept of volume of interest (VOI) was introduced that divides a given CT image into subimages, each of which contains a bronchial branch region[67]. Every bronchus branch is sequentially segmented inside the subimage from the trachea by extending the VOI in the bronchus running directions. Ultimately, all the segmented images are unified to form an integrated airway tree. This method extracts the peripherals well, but some bronchus regions, which are affected by the partial volume effects (PVE), aren't completely extracted. Moreover, due to the low contrast of intensity between the airway lumen and the airway wall, the region-growing method inevitably generates leakages.

In this thesis, we propose a new airway segmentation method from 3D chest CT volumes, based on VOIs [67] and using gradient vector flow (GVF) [88]. This method segments the bronchial regions by applying a cavity enhancement filter (CEF) [77] to trace the bronchial tree structure from the trachea. It then utilizes the CEF in the VOI to segment each branch. Tubular-likeness functions based on GVF and GVF magnitude maps in each VOI are used to assist the predictions of both the VOI positions and the directions of the child branches. By calculating the tubular-likeness function based on GVF and the GVF magnitude maps, the airway-like candidate structures can be specified and their centerlines can be extracted. Based on the extracted centerlines, the branch points of the bifurcations can be detected and used for the VOI placement of the next level. At the same time, to avoid leakages, a leakage detection scheme is introduced that analyzes both the pixel information and the shape[89] of the airway candidate regions extracted in the VOI. Finally, we unify all of the extracted bronchial regions to form an integrated airway tree. This paper is an extended version of our work presented at the International Forum on Medical Imaging in Asia (IFMIA) 2017[62].

GVF, which represents a core component of the approach, was originally presented to guide snake-based segmentation [90]. The active contour model, also called snakes, is a framework in computer vision for delineating an object outline from an image. The active contour model, which is popular in computer vision, is often used in such applications as object tracking, shape recognition, and segmentation and is categorized into two groups: (a) edge-based models [91, 92] and (b) region-based models [93, 94]. In our proposed method, we use GVF, which is an anisotropic edge-preserving gradient diffusion method, to detect tubular objects and extract centerlines.

3.2 Method

3.2.1 Overview

Our proposed algorithm consists of seven steps: (1) trachea extraction and VOI setting, (2) pre-processing, (3) airway candidate extraction from VOI image, (4) leakage de-

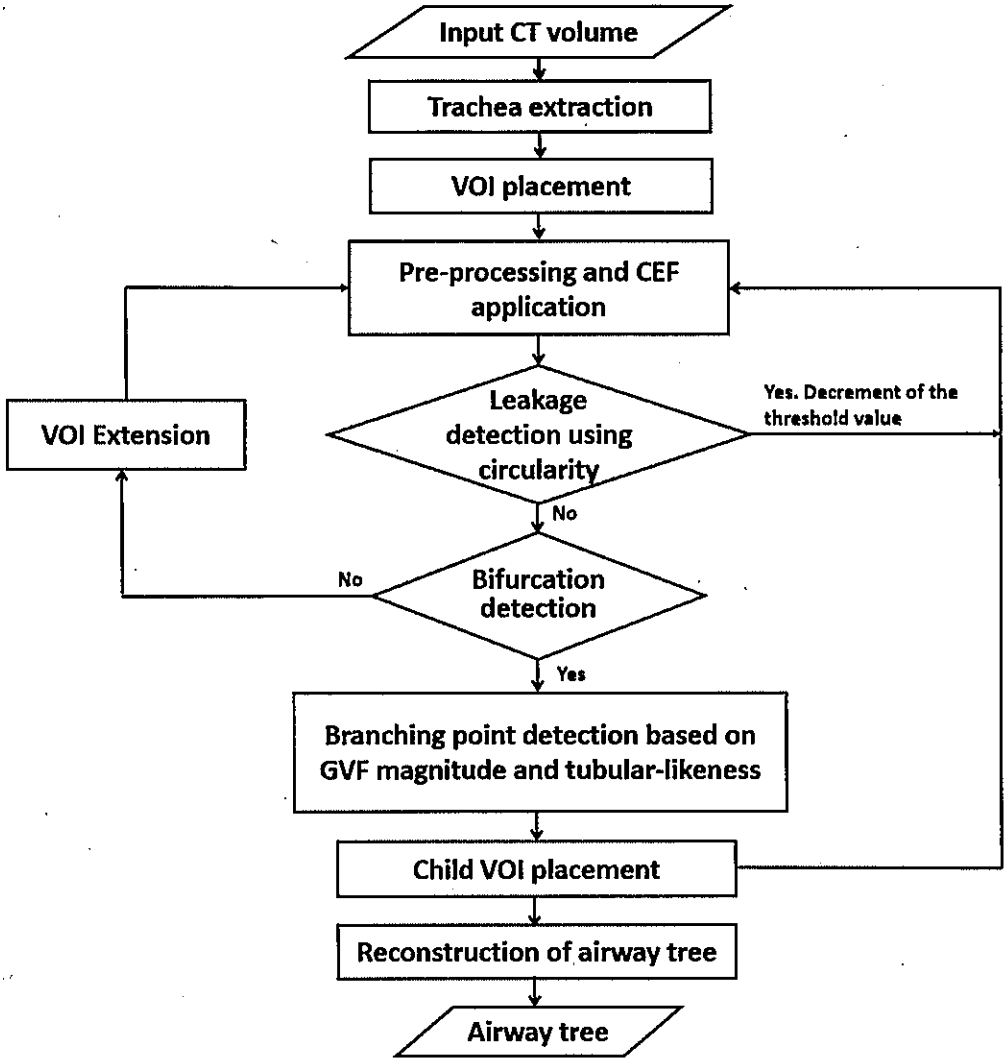

Figure 3.2: Flowchart of proposed method

tection, (5) bifurcation detection and child VOI placement, (6) VOI extension, and (7) reconstruction of airway tree. Our proposed algorithm is an improved and modified version of Kitasaka's algorithm [67]. Its main modifications are Steps (3) to (5). Fig. 3.2 shows a flowchart of it:

3.2.2 Placement of VOI for trachea and trachea extraction

A trachea region is roughly segmented by an airway segmentation algorithm that was previously developed by Mori et al. [65] based on a predefined threshold value T. This trachea region is used to place the initial VOI. A seed point is manually selected on a slice including the trachea region and without lung regions. After the seed point is selected, the trachea regions are extracted from a slice containing the seed point in 20 slices of typical chest CT scans. Then an initial VOI is placed based on the seed point. A VOI is a cuboid that can be specified by the centers of top plane S_1 and bottom plane S_2 that are denoted as P_1 and P_2 (Fig. 3.3) and three basis vectors, e_1, e_2 and e_3. We set the initial VOI for the trachea. Center point P_1 of the VOI is translated to coincide with the seed point. The VOI's size is denoted by width W, height H, and depth D. The direction of e_3 is aligned to the running direction of an airway branch (equal to the direction from center point Q_1 of the airway region on the first slice to center point Q_2 of the airway region on the last slice). Tri-cubic interpolation is utilized for generating a subimage from the original CT image. The image circumscribed by a VOI is called a VOI image. A method for calculating e_1, e_2, and e_3 is described in Section 3.2.7.

The edge length of the VOI (W and H) is set to four times the trachea radius, which was calculated as $r_{top} = \sqrt{A/\pi}$, where A is the area (number of pixels) of the trachea region on the top slice of a chest CT volume. The initial VOI depth (D), which was set to 20 voxels, is extended one voxel by one voxel until the VOI reaches bifurcation that can be detected. For each VOI extension, the trachea region inside the VOI is extracted again based on the selected seed point. The orientation of the VOI, e_3, is adjusted to equal the direction from center point Q_1 of the airway region on the first slice to center point Q_2 of the airway region on the last slice.

3.2.3 Pre-processing and CEF application to VOI image

Whenever a new VOI image is generated, a sharpening filter based on the Laplacian of Gaussian[67] must be utilized to enhance the bronchial wall affected by the partial

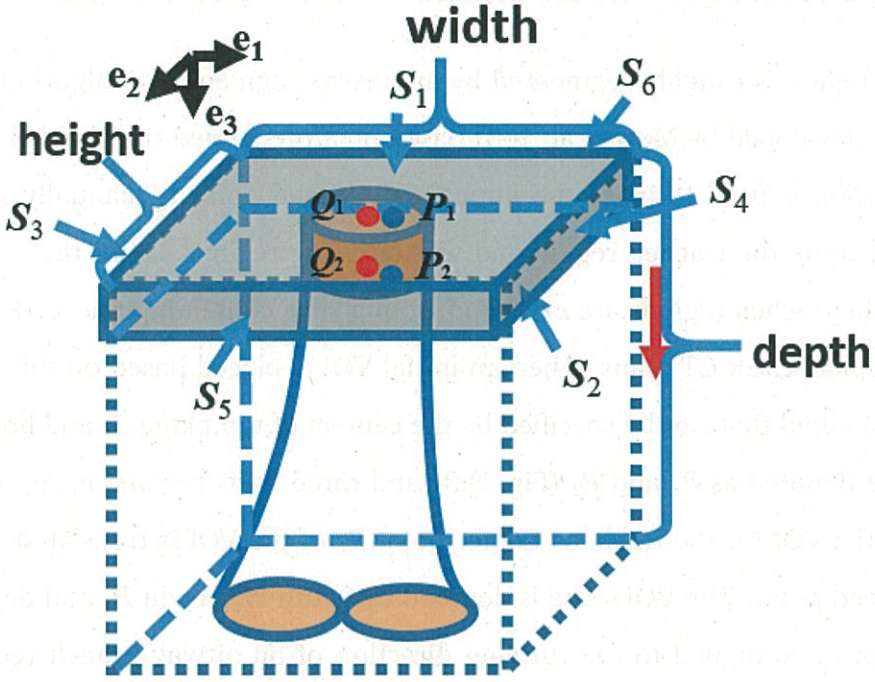

Figure 3.3: Illustration of VOI setting. Red points indicate center points of trachea regions on first and last slices in VOI, and red arrow indicates VOIs extension direction.

volume effects (PVEs). Parameter β used in the Laplacian of Gaussian is a coefficient of the sharpening operation. The sharpening filter is formulated as:

$$\mathbf{V}' = \mathbf{V} - \beta LoG_{\sigma}(\mathbf{V}), \tag{3.1}$$

where $\mathbf{V}$ and $\mathbf{V}'$ are respectively the input and output VOI images and β is a weight that controls the effects of the sharpening operation.

After pre-processing, CEF is used in each VOI to extract the airway regions in the higher branching levels (above the second level), where level denotes the branching

order of the airway branches. CEF [77] is defined as follows:

$$g_{x,y,z} = \sum_{i,j,k\in\{-1,0,1\}} \max_{\substack{r_1=1,\ldots,R_v \\ r_2=1,\ldots,R_v}} \{L_{x,y,z}(i,j,k,r_1,r_2) - P_{x,y,z}(i,j,k,r_1,r_2)\}, s.t.\ 9k+3j+i<0 \quad (3.2)$$

$$L_{x,y,z}(i,j,k,r_1,r_2) = f_{x-ir_1,y-ir_1,z-ir_1} - 2f_{x,y,z} + f_{x+ir_2,y+ir_2,z+ir_2} \quad (3.3)$$

$$P_{x,y,z}(i,j,k,r_1,r_2) = f_{x-ir_1,y-jr_1,z-kr_1} - f_{x+ir_2,y+jr_2,z+kr_2}, \quad (3.4)$$

where $f_{x,y,z}$ is the intensity value of a voxel located at (x,y,z) and $g_{x,y,z}$ is the CEF output. Eq. 3.2 defines CEF. Eqs. 3.3 and 3.4 express the first and second terms in Eq. 3.2. r_1 and r_2 denote the filters radii. R_v is an important parameter in CEF. Eq. 3.3 ($L_{x,y,z}$) calculates the CT intensity value difference between the airway wall and regions, and Eq. 3.4 ($P_{x,y,z}$) is a penalty function that suppresses the CEF output when a high CT intensity value exists only on one side of the voxel (x,y,z) in each direction. Set $\{(x-i,y-j,z-k)|i,j,k=0,\pm1;9k+3j+i<0\}$ is half of the 26-neighborhood of a voxel (x,y,z).

Figure 3.4 shows the CEF illustration in a VOI image. This filter enhances the cavity regions with a diameter of $2R_v$. Therefore, R_v is chosen by the radius of the candidate airway region. In our proposed algorithm, R_v is set to half of the width of the current VOI image. Because the airway regions have lower intensity values than the bronchus wall regions, we define threshold T_{CEF} for the CT intensities to select the regions with a lower intensity than the airway walls (>800H.U.) in the VOI. The CEF filter is only applied to the area lower than T_{CEF}. Then all of the CEF outputs larger than zero ($g_{x,y,z}$>0) are considered candidate voxels of the airway region. Fig. 3.5 shows the CEF result in a VOI image.

3.2.4 Leakage detection

After obtaining the airway candidate regions in a VOI, some leakage regions may exist in it. Leakage regions denote the outer-airway regions. To reduce such regions, we analyze the number of connected components in the VOI by a 3D labeling process and select the largest connected component. Basically, since the airway region in the VOI is

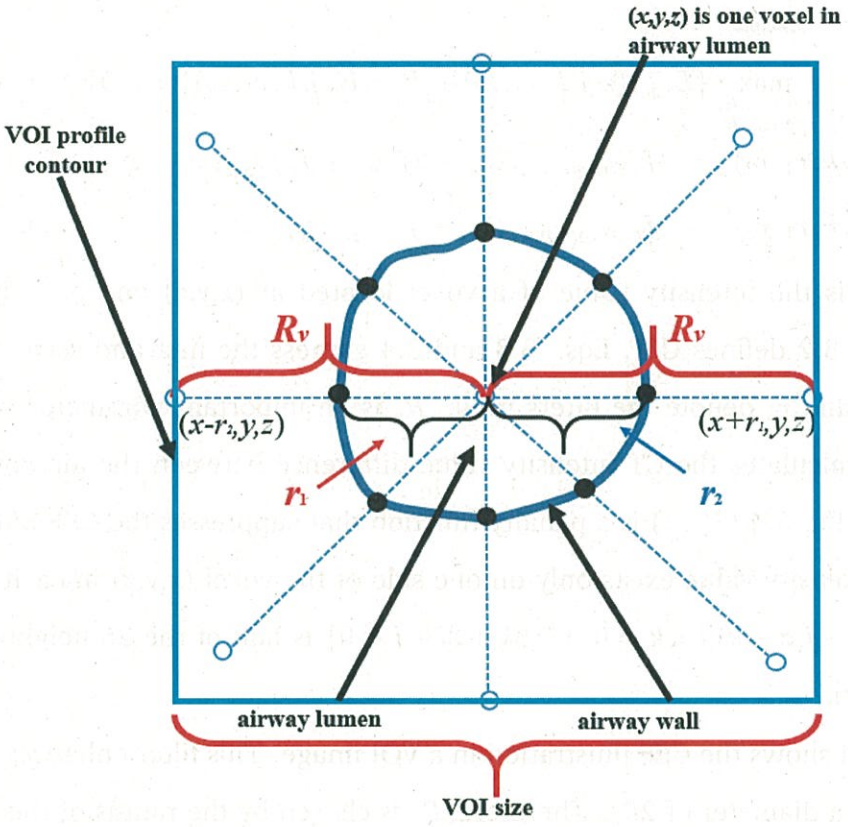

Figure 3.4: CEF illustration used in a VOI image

the largest component in it, we keep the largest connected component and remove the smaller ones.

However, the selected area still has some leakage regions caused by PVE, as shown in Fig. 3.5. In such cases, we need to adjust parameter T_{CEF} of the CEF and perform the same CEF enhancement procedure. We detect the leakage regions by the following two metrics: (a) S_{ratio} between the extracted airway area on the VOI surface and all six VOI surface areas, and (b) the contour circularity of the airway regions on the front surface of the VOI, called T_s. If any of these two parameters exceed the given thresholds (shown below), we assume that the leakage regions occurred in the VOI. We find empirically that $S_{ratio} \leq 1/3$ if the airway regions are correctly extracted. If leakage regions exist

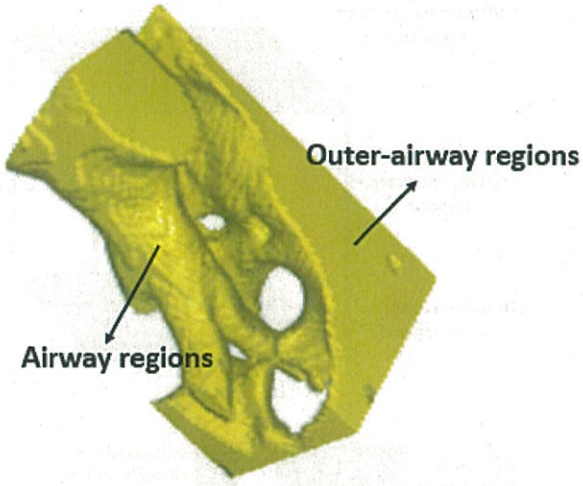

Figure 3.5: Example of CEF extraction result in a VOI image. Volume rendering shows CEF result. This example has leakage.

in a VOI, this ratio increases. Fig. 3.6 shows a calculation of S_{ratio}. Fig. 3.6(a) shows the airway extraction result in a VOI and (b) shows the airway extraction result on the surface. If the airway regions are extracted correctly, the sum of the extracted airway area on the VOI surface does not exceed the area of the two faces in a VOI cube. Therefore, S_{ratio} does not exceed 1/3. The contour circularity is used to simultaneously estimate the shape of the airway candidate region contour on the VOI's front surface [89]. If no leakage regions occurred in the VOI, the contours shape is almost circular. Otherwise, the shape of the airway candidate contour is irregular. The circularity is calculated using $C{=}\frac{A}{P^2}$, where P is the perimeter and A is its internal area. A unit circle has circularity $\left(C_0 = \frac{\pi r^2}{(2\pi r)^2} \simeq 0.0796\right)$. Figure 3.7 represents the extracted contour projection of the branch regions to the surface perpendicular to the extension direction, (a) to (d) show the contour changes along the bronchi running direction, and (e) shows the contours of the airway regions and the leakage.

We found empirically that if the bronchus regions are correctly extracted, bronchus area ratio S_{ratio} will not exceed 1/3. If leakage occurs, the ratio will increase. The circularity of the contours is calculated using $C{=}\frac{A}{P^2}$, where P is the perimeter of the contour and A is its internal area. A unit circle has circularity $\left(C_0 = \frac{\pi r^2}{(2\pi r)^2} \simeq 0.0796\right)$. Therefore, a circularity value far from C_0 indicates an irregular shape. We define threshold value

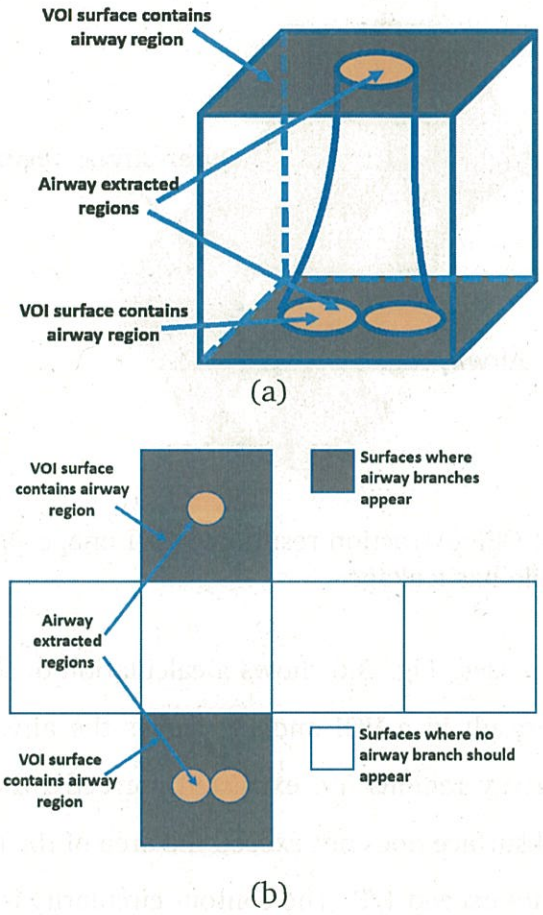

Figure 3.6: Illustration of calculating ratio S_{ratio} between extracted airway area on VOI surface and all six VOI surface areas: (a) airway extraction result in a VOI, and (b) airway extraction result on surface. Orange areas are airway candidate regions on VOI surface, and gray areas are two faces of a VOI.

T_s, which justifies the presence of the leakage.

If leakage is detected by the leakage detection procedure, the threshold value in CEF is decreased. This new threshold value is utilized in CEF to extract the bronchus region again until no leakage occurs in the VOI.

3.2.5 Furcation detection

The furcation regions are detected by analyzing the number of connected components appearing on the surface of the VOI image[67]. Some noise usually occurs in the CT volume. Although the CEF result will be affected by the noise, the airway extraction

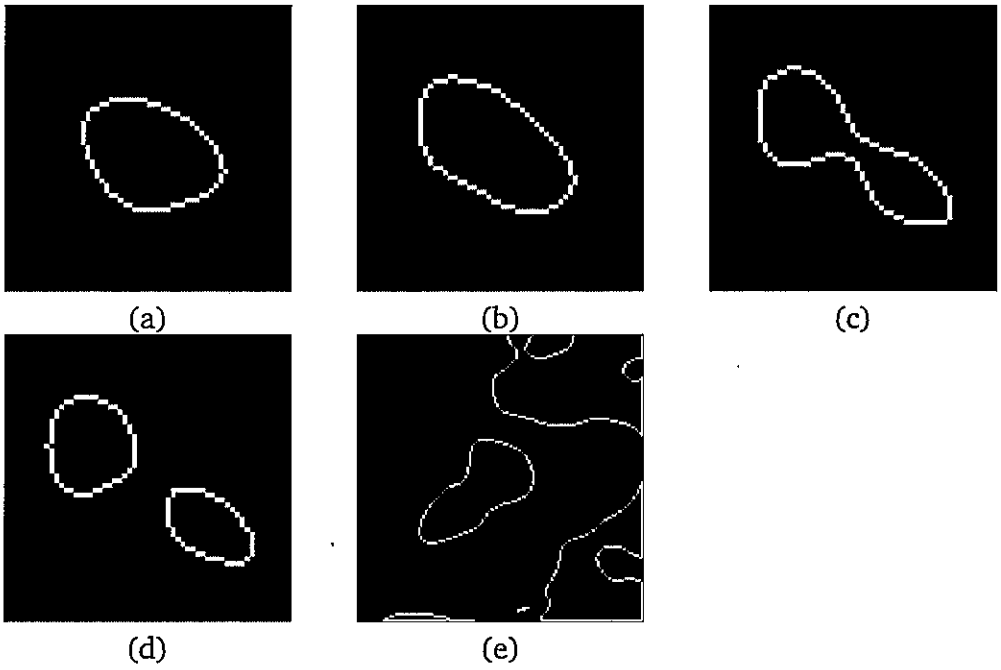

Figure 3.7: Examples of contours of airway region cross-section in different VOI volumes: (a) to (d) indicate concrete contours of airway region and (e) indicates leakages in VOI volumes.

result in the VOI will not be affected, because we use CEF to enhance the airway regions in one VOI regardless whether noise exists. Leakage is caused by the similar intensity distribution of the peripheral region not by the noise. We classify the extracted voxels on the surface using a 3D labeling process and measure the number of voxels of each label $S_i(1 \leq i \leq N_c)$. The 3D labeling process is the 26-neighborhood connected component labeling process, which computes the connected components on the VOI surface, and its height axis is 1. The following conditions are checked iteratively in each VOI:

- $\mathrm{N_c} = 0$

  In this VOI, since no bronchus region was detected, the tracing is terminated.

- $\mathrm{N_c} = 1$

  In this VOI, no furcation was detected, but the bronchial region continues to be traced.

- $\mathrm{N_c} = 2$ or 3

  In this VOI, both bifurcation and trifurcation were detected.

If no bifurcation occurs, the VOI is extended until bifurcation occurs or no airway branch occurs. If there are high-curvature branches, a new VOI will be established during the tracking procedure and the position and direction will be adjusted based on the segmented result.

3.2.6 VOI extension

The length of the VOI is extended by one voxel, and the CEF result is re-calculated. The leakage and bifurcation detections are processed again.

3.2.7 Branching-point detection and child VOI placement

3.2.7.1 Gradient Vector Flow

If a bifurcation or a trifurcation is detected in a VOI, child VOIs are generated for further tracing of the airway tree. The branching-point must be detected to place the new child VOIs. If we just apply a thinning process to search for the branching-point, some spurious branches are generated that complicate its appropriate and stable detection. In the proposed algorithm, the GVF [88] in the 3D space is utilized to detect the branching-point because it is sensitive to the centerline region of the tubular structure. Let V be the original VOI volume. Considering GVF, inverted local derivatives $\vec{F(\mathrm{x})} = -\nabla(G_{\sigma_g} * V(\mathrm{x}))$, which is the convolution of G_{σ_g} and $V(\mathrm{x})$, are computed for every voxel $\mathrm{x} = \{x, y, z\}$, where G_{σ_g} is a Gaussian filter kernel at scale σ_g. The normalized initial vector is obtained as follows:

$$\mathbf{F^n}(\mathrm{x}) = \begin{cases} \frac{\mathbf{F(x)}}{|\mathbf{F(x)}|} & if|\mathbf{F}(\mathrm{x})| \geq F_{\mathbf{max}} \\ \frac{\mathbf{F(x)}}{\mathbf{F_{max}}} & otherwise, \end{cases} \tag{3.5}$$

where n denotes the normalization and F_{max} is the maximum value of the gradient field, which controls the normalization. After obtaining the initial vector field, the GVF is calculated, which is defined as $\vec{U}(\mathrm{x})$ that minimizes

$$E(\mathbf{U}) = \iiint_{\Omega} \mu |\nabla \mathbf{U}(\mathrm{x})|^2 + |\mathbf{F^n}(\mathrm{x})|^2 |\mathbf{U}(\mathrm{x}) - \mathbf{F^n}(\mathrm{x})|^2 \, \mathrm{dx}, \tag{3.6}$$

where $\vec{U}(\mathrm{x})$ is the GVF result and μ is a weighting constant of the two terms. The GVF magnitude is computed based on the result as $M(\mathrm{x}) = \left|\tilde{\mathrm{U}}(\mathrm{x})\right|$. After computing the magnitude of GVF, we normalize it as $M^n(\vec{x})$ in equation 3.7, where $M_{max}(\mathrm{x})$ is the maximum value in the VOI, and $M_{min}(\mathrm{x})$ is the minimum value in the VOI. Then we calculate the GVF magnitude map as $M_{map}(\vec{x}) = M^n(\vec{x}) * 1000$. Figure 3.8 shows a GVF result $\vec{U}(\mathrm{x})$ using a 2D cross-section in each slice of an airway branch and the corresponding magnitude map $M_{map}(\vec{x})$. Each cross-section is obtained from the slice in each VOI, because the VOI is aligned with the running direction of each airway branch.

$$M^n(\mathrm{x}) = \frac{M(\mathrm{x}) - M_{min}(\mathrm{x})}{M_{max}(\mathrm{x}) - M_{min}(\mathrm{x})}. \tag{3.7}$$

3.2.7.2 Tubular-likeness function

To extract the airway centerline and identify the branching-point of each bifurcation, a tubular-likeness function is computed in each point of the VOI image. For this purpose, a circle is fitted to the data in the cross-sectional slice in the VOI. Fig. 3.9(a) illustrates the tubular-likeness, and Fig. 3.9(b) represents the tubular-likeness result. The tubular-likeness function, which computes the mean flow through a circle of radius r, is given as [88] on each slice:

$$T(\mathrm{x}, r) = \frac{1}{2\pi r} \int_{\alpha=0}^{2\pi} \langle \tilde{\mathrm{U}}_{\mathrm{x}}(\alpha, r), \tilde{\mathrm{D}}(\alpha) \rangle d\alpha, \tag{3.8}$$

where $\vec{U}_{\mathrm{x}}(\alpha, r)$ represents the GVF vector at voxel x and $\vec{D}(\alpha)$ defines a normal vector on the circle pointing toward its center shown in Fig. 3.9(a). We compute the inner product between $\vec{U}_{\mathrm{x}}(\alpha, r)$, and $\vec{D}(\alpha)$ and sum them up over 32 discrete points on the circle. For the initialization of the circle fitting, we set the radius to 1 pixel. During the fitting procedure, the radius is gradually increased until the circle touches the edge of the object. We set a threshold value to -400 H.U. If any voxel intensity on the circle exceeds -400 H.U., the edge of the object is touched, and r stops increasing. After computing the tubular-likeness, we normalize it as $T^n(\vec{x}, r)$ in Eq. 3.9, where $T_{max}(\mathrm{x})$ is the maximum value in the VOI and $T_{min}(\mathrm{x})$ is the minimum value in it. Then we calculate tubular-likeness result $T_{li}(\vec{x})$ as $T_{li}(\vec{x}, r) = T^n(\vec{x}, r) * 100$. Fig. 3.9(a) illustrates

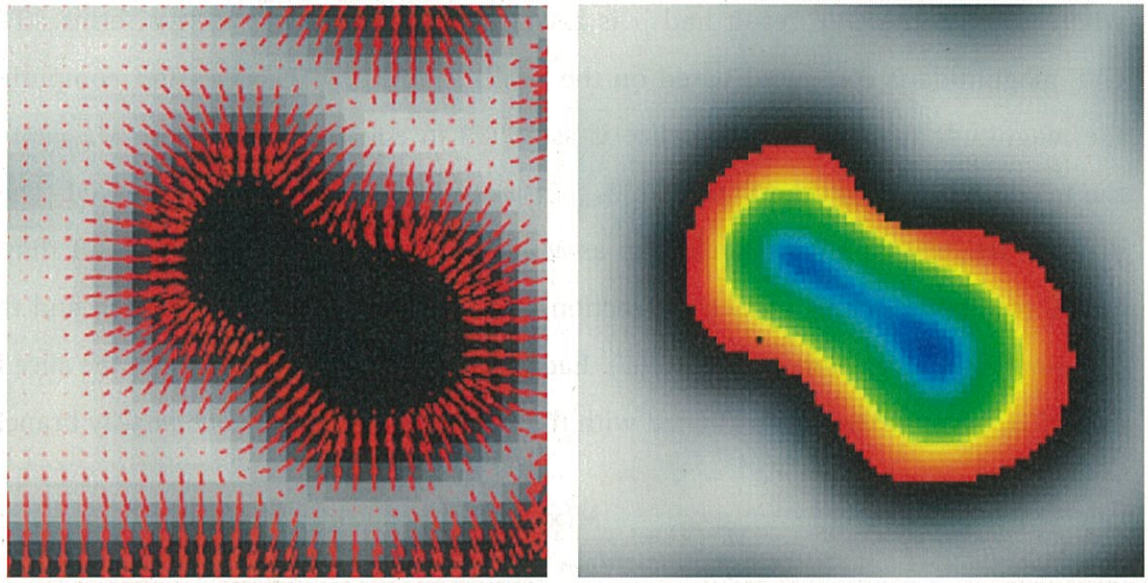

(a) (b)

Figure 3.8: GVF illustration using a 2D cross-section of airway structure: (a) result of GVF field $\vec{U}(\mathrm{x})$ where red arrows indicate vector direction and (b) result of GVF magnitude map $M_{map}(\vec{x})$, where red indicates higher value, and blue indicates lower value.

the computation of a tubular-likeness and (b) shows corresponding tubular-likeness result $T_{li}(\mathrm{x}, r)$:

$$T^{n}(\mathrm{x}, r) = \frac{T(\mathrm{x}, r) - T_{\min}(\mathrm{x}, r)}{T_{max}(\mathrm{x}, r) - T_{\min}(\mathrm{x}, r)}. \tag{3.9}$$

3.2.7.3 Branching-point detection and child VOI placement

On the edge of the tubular structures, GVF has a strong vector flow, which weakens in the central areas. Therefore, the GVF magnitude map can generate higher outputs near the edges and lower values inside the tubular structures. The tubular-likeness outputs generate higher values in the central areas of the tubular structure due to the duality of the vector flow. According to Figs. 3.8(b) and 3.9(b), the center area of the airway is enhanced both in GVF magnitude and tubular-likeness. In Fig. 3.8(b), while the central area has a lower GVF magnitude, its peripheral area has higher values. Moreover, as seen in Fig. 3.8(b), the central area shows high tubular-likeness, whereas its periph-

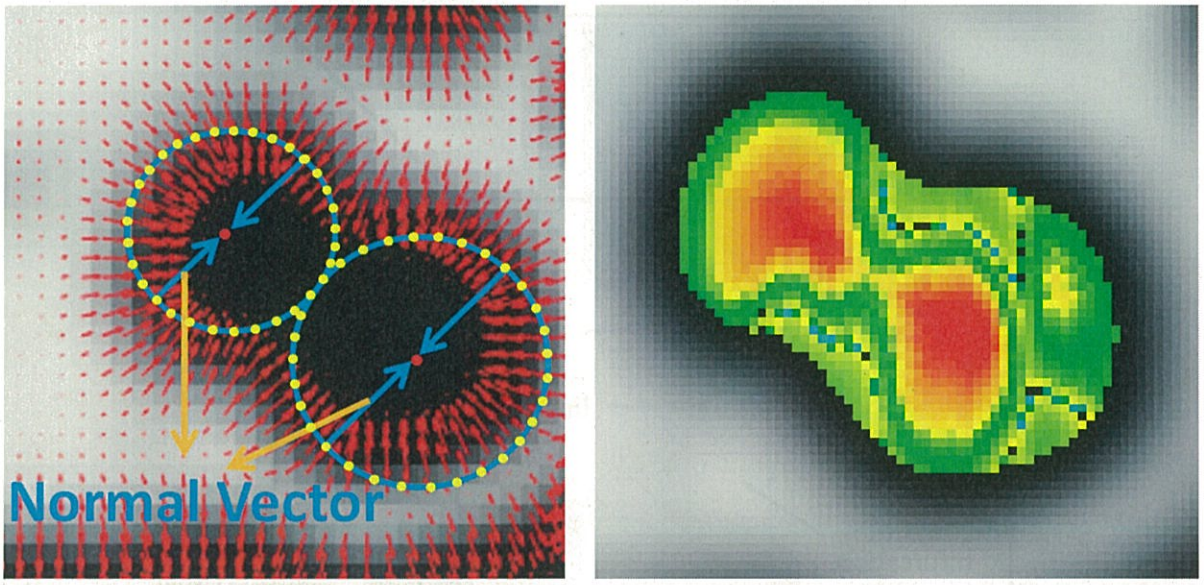

(a) (b)

Figure 3.9: Result of tubular-likeness based on GVF: (a) tubular-likeness concept: sum of inner product of gradient vector flow (red arrows) and normal vector (blue arrows) over 32 discrete points on the circle, and (b) tubular-likeness result, where red areas show higher tubular-likeness value, and green areas show lower tubular-likeness value.

eral area has lower values. To extract the centerlines, two threshold values, T_m and T_l, are both used on the GVF magnitude and tubular-likeness for extracting the candidate central area. We selected the regions for which the GVF magnitude map is less than T_m and more than T_l as the centerline candidate region. A thinning process extracts the centerline from the candidate region[95]. The centerline is extracted using a thinning process [95]. The branching-point detection approach is applied to the thinning centerline result to find the branching-point[96].

A centerline is expressed as a set of voxels, each voxel can be classified into the following three categories: (1) terminal voxel (a voxel connected to only one voxel in 26-neighnorhood), (2) line voxel (a voxel connected to only two voxels in 26-neighnorhood), and (3) branching voxel (a voxel connected to three or more voxels in 26-neighnorhood)[97]. There are some unavoidable false branching voxels in the centerline. To remove them, the structure of the bifurcation is used to classify the branching voxel. A bifurcation has the structure as shown in Fig. 3.10 when aligned with the current VOI: only one line-

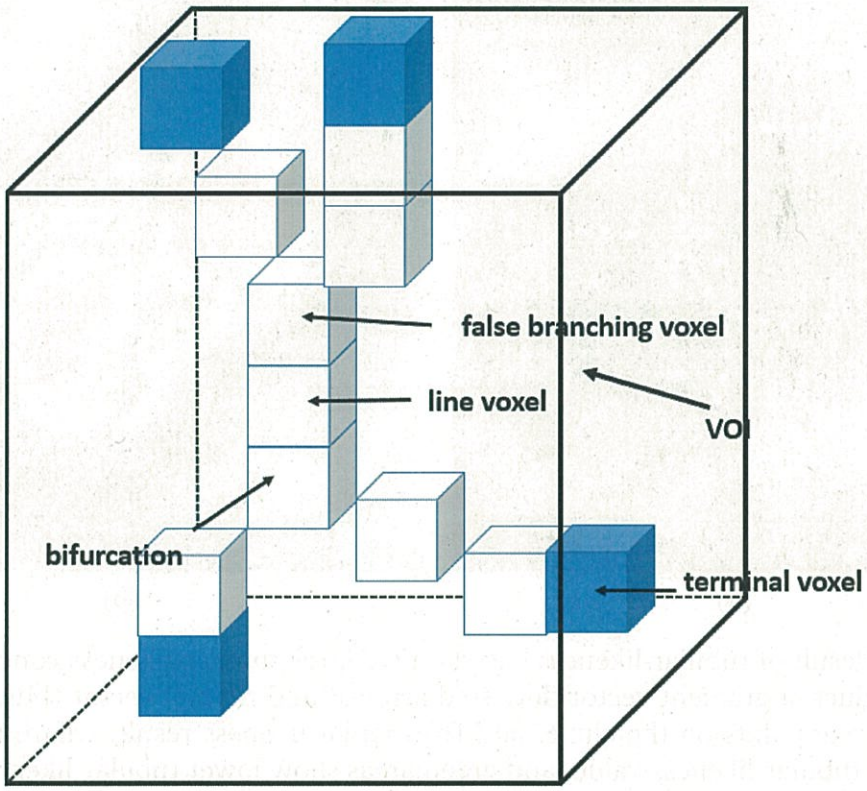

Figure 3.10: Illustration of different kinds of voxels in centerline.

point in the proximal (upper layer) and more than two neighbors in the distal (lower layer). This definition holds if we defined proximal equals to "parent node", distal equals to "child node" with respect to the axis traversal "parent" to "child" at the same time. Figure 3.10 shows the structure of the branching voxel which is not bifurcation, which has more than two neighbors in the proximal and only one neighbor in the distal. If such a structure is detected, the branching-point is considered as false and removed.

If the branching-point is detected, the child VOIs are placed to further trace the airway tree, as shown in Fig. 3.11 [67, 68]. Point g is the detected branching-point, and g_1 and g_2 are the center points of the components on the VOI surface. The VOI is oriented from furcation point g to center of gravity g_i of the child branch. Center point P_1 on plane S_1 of child VOI is coincident with point g, and center point P_2 on plane S_2 is coincident with point g_1 or g_2. The width and the height of a child VOI are set to four

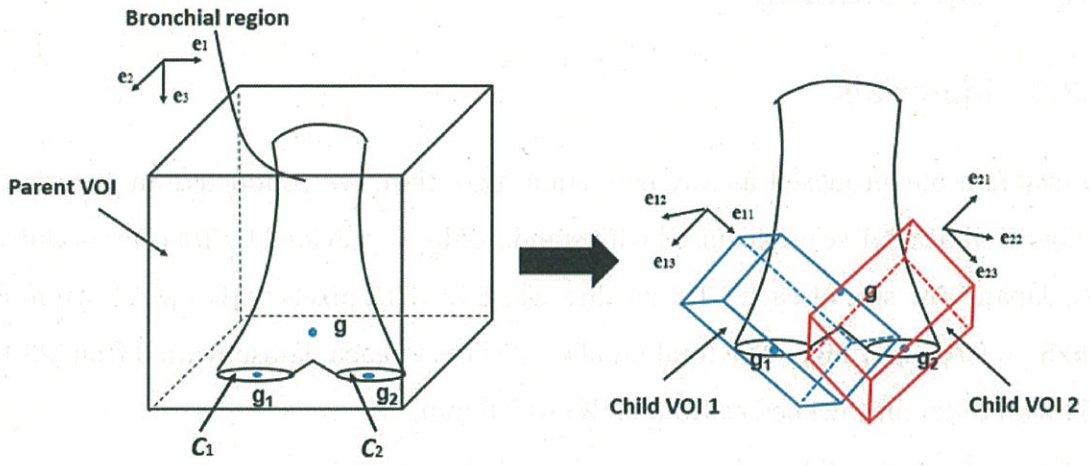

Figure 3.11: Generation of child VOIs: Each child VOI is oriented along a line from detected furcation point g to center of gravity g_i of child branches. g_1 and g_2 are center points of components C_1 and C_2 on VOI surface. Width and height of a child VOI are set four times the size of child branch radius.

times the size of the radius of the child branch, which is calculated from C_1 or C_2. The coordinate system of the child VOI, (e_{i1}, e_{i2}, e_{i3}), is calculated by

$$e_{i3} = \frac{g_i - g}{\|g_i - g\|}, \tag{3.10}$$

$$q = (1, \frac{e_3 \times e_{i3}}{\|e_3 \times e_{i3}\|}) \tag{3.11}$$

$$e_{i1} = q \bullet e_1, \tag{3.12}$$

$$e_{i2} = e_{i3} \times e_{i1}, \tag{3.13}$$

$$e_{i1} = e_{i2} \times e_{i3}, \tag{3.14}$$

where q denotes the quaternion from e_3 to e_{i3}, "$\times$" denotes the outer product of the vectors, and "$\bullet$" denotes the rotation of the vectors. Then the bronchial region in a child VOI is updated.

3.2.8 Reconstruction of airway trees

Finally, we reconstruct airway trees by projecting the bronchial regions inside all of the VOI images into the original CT images using interpolation.[67]

3.3 Experiments

3.3.1 Materials

To evaluate our proposed airway extraction algorithm, we conducted an experiment using 50 clinical CT scans acquired with standard doses provided by Tokushima University, Japan. The size of each CT scan slice was 512×512 pixels with a pixel size in the 0.625 - 0.976 mm range. The total number of slices in each dataset varied from 239 to 962 with different thicknesses from 0.625 to 2.0 mm.

We performed validation on two separate groups of datasets: one group used a development set for tuning the parameters with 25 cases, and the other used a test set with 25 cases. Each group had both high- and low-resolution cases. The development and test sets were decided randomly with one combination.

To evaluate the experiment results, we performed manual segmentation of these 50 leakage free cases. Obtaining the ground-truth data for the whole dataset was extremely exhausting and time-consuming. All of the ground-truth data of the slices were obtained by hand-tracing by multiple human experts with tracing software developed in our laboratory. Each case took nearly one day of tracing.

The parameter settings in this study are listed in Table 3.1. Before the experiments, the required initialization for the existing parameters in each phase had to be done. In the pre-processing phase, where we have to use LoG, standard deviation σ was selected as $\sigma = 0.5mm$, and parameter β was set to 0.05. These two parameters were chosen empirically by applying this filter with different standard deviation values to the CT volumes and the best ones were chosen. Parameter T_{CEF} in CEF was chosen based on the intensity of the airway regions in the CT volume. Leakage detection ratio S_{ratio} between the extracted airway area on the VOI face and all of the surface areas in a VOI did not exceed $1/3 \approx 0.33$. Leakage detection threshold T_s was selected empirically as 0.5. By selecting these two thresholds in the leakage detection, the false positive regions in each VOI were reduced. Gaussian filter kernel σ_g used as the initial vector in GVF was selected as 0.5 mm to allow a clear GVF magnitude distribution map in Fig. 3.8(b) and

Table 3.1: Parameter setting for proposed algorithm

Parameter	Value
Pre-processing Gaussian scale σ	0.5 mm
Pre-processing weighting factor β	0.05
Trachea extraction threshold T	-750 H.U.
CEF extraction threshold T_{CEF}	-800 H.U.
Decrement of CEF extraction threshold ΔT	10 H.U.
Leakage detection ratio S_{ratio}	0.33
Leakage detection threshold T_s	0.5
Gaussian filter kernel σ_g	0.5 mm
GVF magnitude threshold T_l	500
Tubular-likeness threshold T_m	50

a tubular-likeness result in Fig. 3.9(b). GVF was computed using an iterative update scheme with 500 iterations [90]. The GVF magnitude distribution ranged from 0 to 1000 due to the normalization process, as shown in Section 2.7.1. The middle value of 500 was selected as T_l. The tubular-likeness distribution ranged from 0 to 100, and the middle value of 50 was selected as T_m.

3.3.2 Evaluation of proposed algorithm

We compared our proposed algorithm with two previous algorithms, Kitasaka's algorithm [67], which is the previous method of our proposed method based on VOI and region-growing without local intensity analysis and GVF (our proposed method is an extension of the Kitasakas algorithm), and Meng's algorithm, which is the state-of-the-art using local intensity analysis and a machine learning technique to process whole CT scans without VOI [61].

The segmentation results by these algorithms are summarized in Table 3.2. In our evaluation, we computed the tree length (TL) by calculating the total length of the airway tree, the tree length detection (TLD) by calculating the percentage of the true positive tree lengths divided by the ground-truth tree lengths, the branch detection (BD) by calculating the number of extracted airway trees, the true positive rate (TPR) by calculating the percentage of true positive branches divided by the ground-truth

branches, and the false positive rate (FPR) by calculating the percentage of false positive voxels divided by the detected voxels. The airway has a tree-like structure, and the radii of different branches of different levels vary. Most conventional airway segmentation methods can extract the main and principle bronchus (lower than six levels). These results have almost 80% volume overlapping compared with the ground-truth dataset. The improved methods can extract more peripheral airway branches, which have smaller radii. Therefore the volume only slightly increases, even though the number and total length of the extracted airway branches increase significantly. Therefore, we computed TL, TLD, BD, and TPR instead of the overlap of the volumes (e.g., dice scores). In airway segmentation, the false positive regions are presented as "leakage" regions (without regular shape and size), which are not branches. Therefore, we calculated the percentage of false positive voxels as FPR.Table 3.4 shows the average results of the proposed method on different voxel sizes and thicknesses. The results are not correlated with the thicknesses and voxel sizes. We examined the differences in TL, TLD, BD, TPR, and FPR using the Wilcoxon signed-rank test. The corresponding p-values of the proposed algorithm and two previous algorithms are found in the last row of Table 3.2. The significance level was set to $p \leq 0.05$. The box plots of TL, TLD, BD, TPR, and FPR are presented in Fig. 3.13. Fig. 3.14 also shows the extraction evaluation results of the proposed algorithm and a comparison with the previous algorithm [61, 67]. Fig. 3.15 compares the airway segmentation results of Kitasaka's algorithm [67], Meng's algorithm [61], and our proposed algorithm in different cross-sections in a VOI. Fig. 3.16 shows an example of a sequence of the airway candidate region with different T_{CEF}, after decreasing T_{CEF}, where the leakage regions decreased. Fig. 3.17 compares the results of directly thinning the airway candidate regions detected by CEF and the central areas detected by GVF. Fig. 3.18 compares the child VOI placement based on the branching-point detection of previous and proposed algorithms.

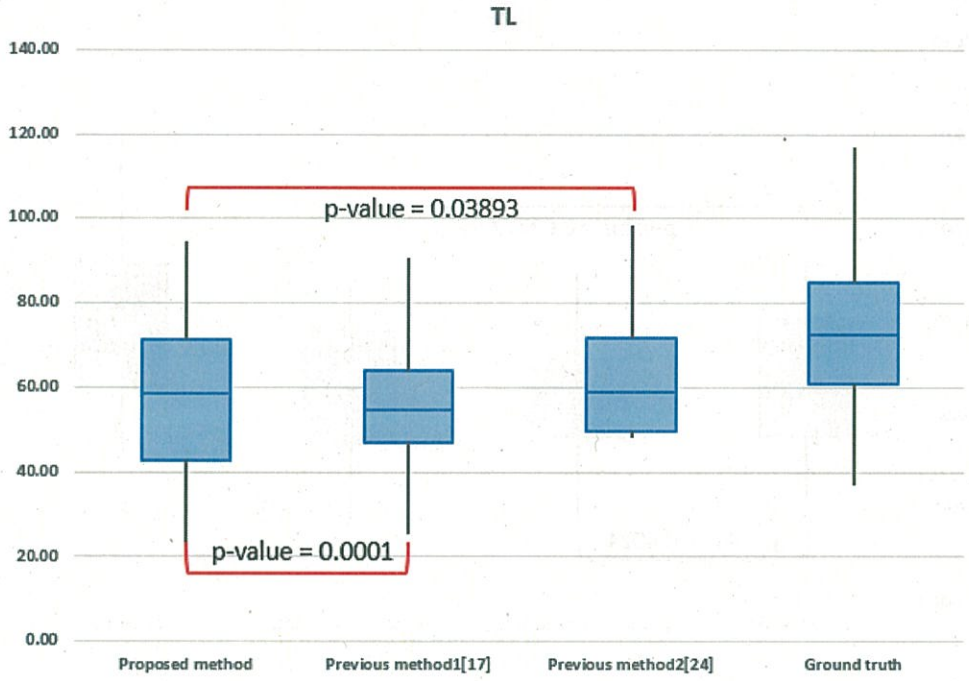
TL
140.00
120.00
100.00
80.00
60.00
40.00
20.00
0.00
p-value = 0.03893
p-value = 0.0001
Proposed method
Previous method1[17]
Previous method2[24]
Ground truth

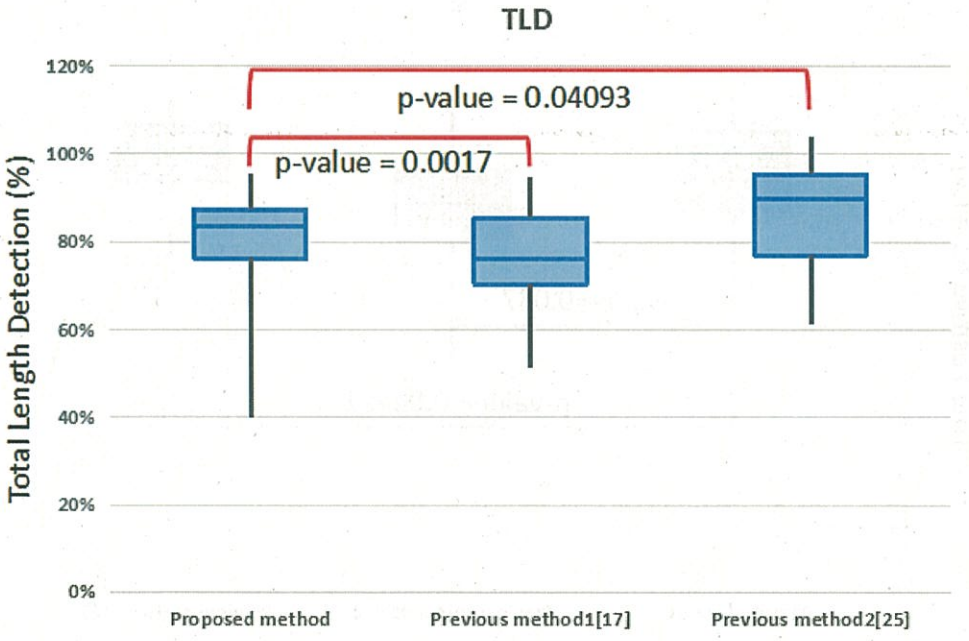
TLD
Total Length Detection (%)
120%
100%
80%
60%
40%
20%
0%
p-value = 0.04093
p-value = 0.0017
Proposed method
Previous method1[17]
Previous method2[25]

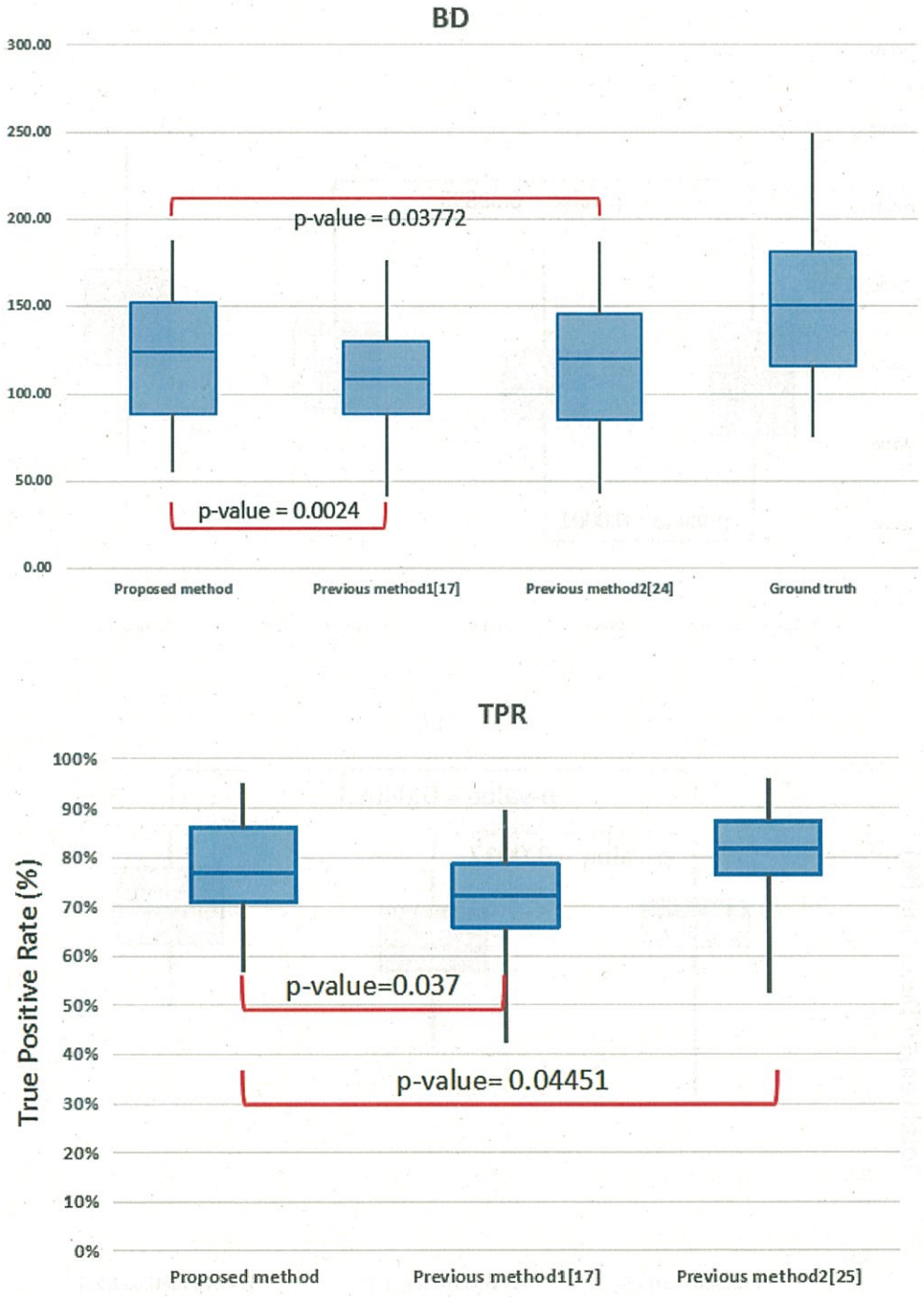

Figure 3.12: Box plots of TL, TLD, BD, TPR, and FPR

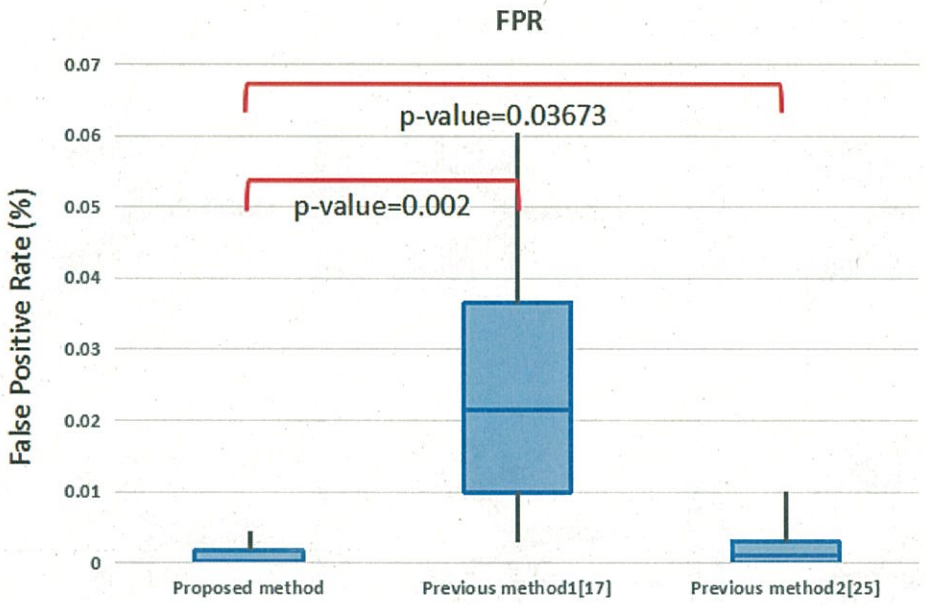

Figure 3.13: Box plots of TL, TLD, BD, TPR, and FPR. Boxes show variance distribution of results of proposed method (TL, TLD, BD, TPR, and FPR), previous method 1 [67], previous method 2 [61], and corresponding ground-truth data.

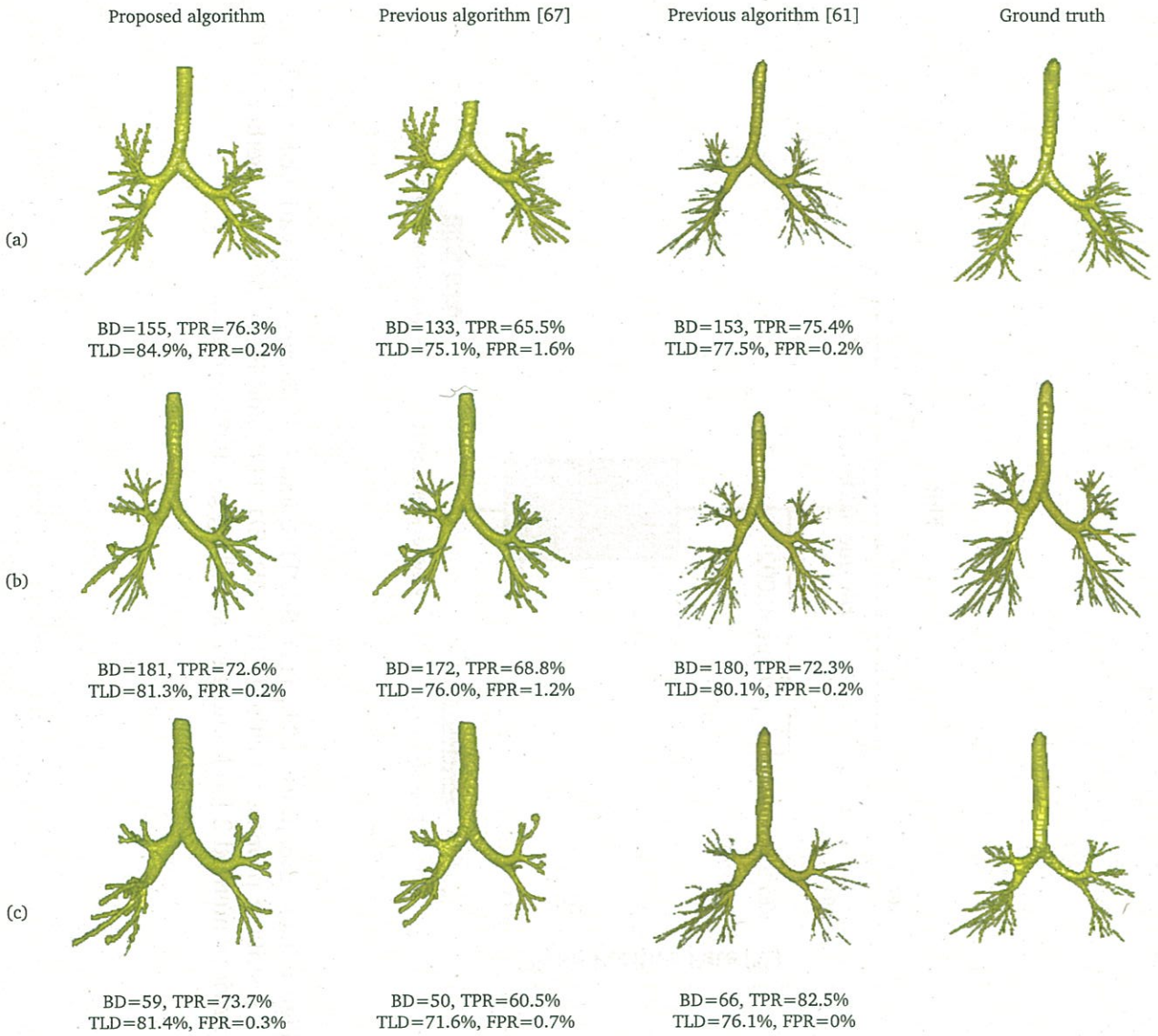

Figure 3.14: Airway extraction results of proposed method, two previous methods [61, 67], and corresponding ground-truth dataset: (a) proposed method result with high performance and correspondence comparison, (b) proposed method result with moderate performance and correspondence comparison, and (c) proposed method result with poor performance and correspondence comparison.

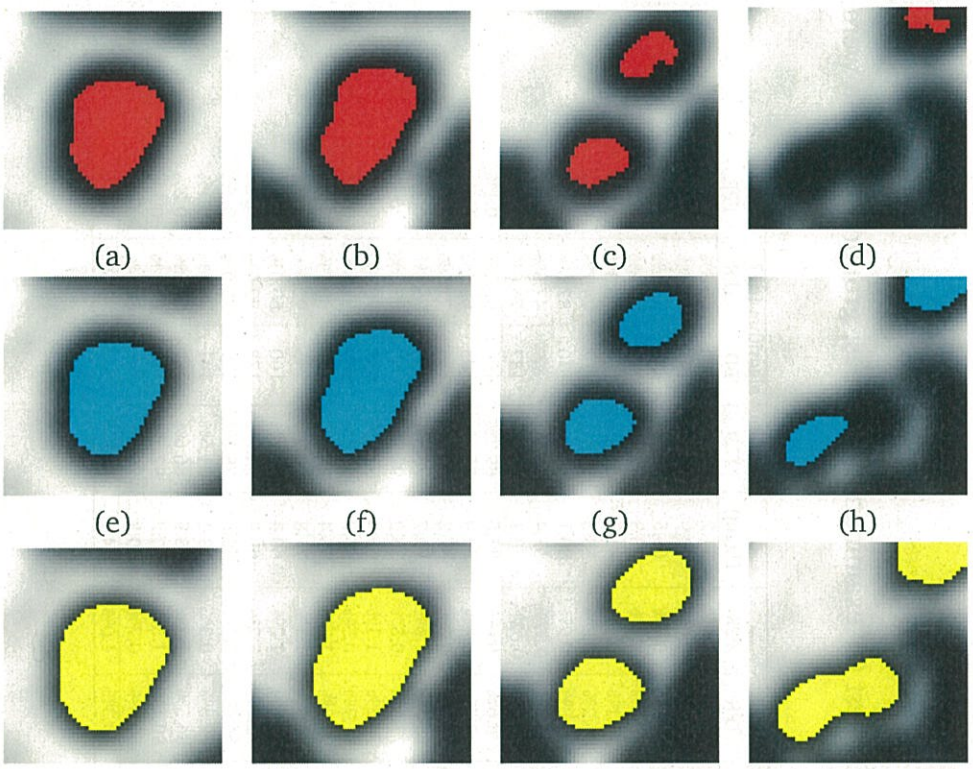

Figure 3.15: Comparison of airway segmentation results of cross-sections of a VOI: (a) to (d) show segmentation results in VOI in previous algorithm [67], (e) to (h) show segmentation results in previous algorithm [61], and (i) to (l) show segmentation results in proposed algorithm.

Table 3.2: Comparison of segmentation results for airway tree in 50 chest CT examination volumes; ground-truth data were generated manually and BD indicates branch detection.

Case	Proposed algorithm				Previous algorithm [67]				Previous algorithm [61]			
	TL(cm)	TLD	BD	TPR	FPR	TL(cm)	TLD	BD	TPR	FPR	TL(cm)	TLD	BD	TPR	FPR
1	58.3	83.8%	107	73.2%	0.3%	55.5	79.8%	95	66.4%	1.8%	51.2	73.7%	102	69.8%	0.15%
2	69.3	86.6%	162	82.5%	0.2%	64.1	80.0%	143	73.3%	0.6%	43.9	54.8%	145	51.4%	0%
3	78.3	91.9%	119	60.7%	0.1%	52.1	61.3%	105	54.9%	0.7%	68.5	80.4%	115	58.4%	0.2%
4	83.5	81.3%	181	72.6%	0.2%	78.1	76.0%	172	68.8%	1.3%	82.3	80.1%	180	73.2%	0.2%
5	88.6	69.8%	188	76.8%	0.2%	75.8	59.7%	176	72.1%	0.7%	81.0	63.8%	180	72.3%	0.2%
6	73.5	76.3%	143	95.1%	0.1%	66.9	69.4%	125	86.2%	0.8%	58.3	60.5%	112	74.7%	0.1%
7	78.6	83.8%	153	78.7%	0.2%	60.7	64.7%	115	60.8%	0.9%	80.1	85.4%	170	87.6%	0.5%
8	73.4	92.7%	142	83.7%	0.2%	58.7	74.1%	138	74.5%	0.37%	65.4	82.6%	87	47.5%	0%
9	65.3	62.9%	151	68.6%	0.2%	70.3	67.7%	172	68.8%	0.62%	78.1	75.2%	187	76.0%	0.2%
10	79.5	84.4%	150	92.7%	0.1%	63.5	67.4%	136	78.6%	0.6%	87.5	89.7%	166	98.2%	0.1%
11	71.5	92.3%	128	91.0%	0%	67.1	86.6%	112	89.6%	0.4%	60.9	78.6%	105	62.1%	0.6%
12	91.3	77.8%	160	90.9%	0%	75.3	70.1%	101	57.3%	0.3%	87.2	81.2%	136	77.3%	0.1%
13	78.5	84.9%	155	76.3%	0.2%	69.5	75.1%	133	65.5%	1.6%	71.7	77.5%	153	75.4%	0.2%
14	28.8	78.6%	59	65.8%	0%	35.1	95.9%	69	77.5%	0.5%	38.0	92.5%	75	83.3%	0%
15	65.7	91.7%	156	89.1%	0.1%	57.6	80.4%	130	74.2%	1.1%	65.4	91.3%	139	79.4%	0.2%
16	63.7	93.4%	134	88.5%	0.2%	53.4	78.5%	125	81.7%	0.5%	55.2	81.2%	125	82.8%	0.1%
17	45.7	71.6%	81	70.7%	0%	50.1	78.5%	89	77.3%	1.7%	53.4	83.7%	92	80.7%	0.1%
18	63.7	88.9%	138	87.9%	0.1%	64.8	90.4%	131	82.9%	1.1%	71.8	94.2%	145	92.4%	0.1%
19	45.4	71.5%	95	65.5%	0.1%	50.6	80.0%	103	70.0%	1.2%	60.4	94.8%	100	69.0%	0.5%
20	57.1	77.4%	168	77.4%	0.1%	60.9	82.5%	157	72.3%	2.2%	69.9	94.7%	178	82.0%	0%
21	62.3	83.9%	132	76.5%	0%	52.3	69.1%	114	64.4%	1.1%	58.8	78.6%	129	75.0%	0.3%
22	57.4	88.2%	153	83.2%	0%	49.6	76.2%	143	79.8%	0.3%	53.1	81.6%	141	76.6%	0.1%
23	94.4	83.0%	183	86.4%	0.2%	90.5	79.6%	175	84.5%	1.4%	98.5	86.6%	187	88.2%	0.2%
24	41.5	54.8%	96	71.4%	0%	48.2	63.7%	105	80.1%	1.5%	70.2	92.7%	110	82.1%	0.1%
25	32.4	81.4%	59	73.7%	0.3%	28.5	71.6%	50	60.5%	0.7%	30.3	76.1%	66	82.5%	0%
AVGT[1]	65.9	81.3%	134.2	78.5%	0.1%	60.0	69.3%	120.6	73.3%	1.0%	64.1	80.8%	132.0	77.5%	0.2%

Case	Proposed algorithm					Previous algorithm [67]					Previous algorithm [61]				
	TL(cm)	TLD	BD	TPR	FPR	TL(cm)	TLD	BD	TPR	FPR	TL(cm)	TLD	BD	TPR	FPR
26	65.7	83.6%	140	77.4%	0%	53.0	67.4%	125	69.0%	1.6%	59.0	75.1%	161	89.0%	0.3%
27	61.4	88.9%	116	75.8%	0%	52.8	76.4%	98	64.0%	1.4%	53.7	77.7%	135	88.0%	0%
28	56.1	91.4%	126	88.1%	0.1%	48.9	79.6%	100	69.9%	1.2%	52.7	86.4%	115	80.4%	0%
29	83.5	83.1%	151	70.2%	0%	65.9	65.9%	132	61.4%	0.9%	76.1	76.1%	146	66.5%	0.1%
30	41.4	80.1%	88	84.4%	0.2%	38.7	77.5%	79	77.4%	0.6%	40.2	80.0%	84	80.8%	0%
31	61.1	84.3%	160	84.5%	0.2%	56.1	77.4%	112	78.8%	1.8%	66.6	91.9%	134	94.3%	0.2%
32	33.5	53.8%	89	76.1%	0%	25.4	40.8%	93	79.4%	1.8%	23.9	51.2%	65	55.6%	0%
33	42.8	91.6%	59	66.4%	0%	35.4	75.8%	47	54.0%	1.8 %	38.4	82.2%	52	85.4%	0%
34	51.2	95.6%	143	90.5%	0.1%	47.5	88.6%	121	76.5%	2.2%	49.6	92.5%	135	87.9%	0.1%
35	42.3	85.4%	76	92.0%	0%	25.9	52.3%	65	81.2%	2.4%	31.5	63.6%	73	80.7%	0.2%
36	48.4	85.8%	95	70.1%	0%	45.2	80.1%	88	67.6%	0.7%	51.9	92.0%	109	88.0%	0.7%
37	61.2	80.8%	168	73.1%	0%	56.4	74.5%	116	67.0%	1.2%	61.6	81.4%	154	50.6%	0.5%
38	39.3	93.1%	65	76.3%	0%	32.7	77.5%	56	68.2%	1.2%	29.5	69.9%	43	80.7%	0%
39	49.0	76.1%	69	78.5%	0%	54.1	84.0%	75	86.2%	1.3%	53.7	83.4%	71	86.6%	0.1%
40	41.3	80.7%	55	56.7%	0%	38.5	75.2%	41	42.2%	0.9%	40.2	78.5%	84	84.7%	0%
41	75.3	80.1%	123	72.4%	0%	69.5	73.9%	115	67.6%	1.3%	81.4	86.6%	144	92.1%	0.6%
42	61.5	76.1%	158	67.2%	0.1%	56.1	69.4%	106	56.0%	1.5%	71.6	88.6%	174	80.6%	0.2%
43	28.9	62.0%	73	78.6%	0%	30.2	64.8%	67	74.4%	0.8%	32.7	70.2%	75	83.4%	0%
44	59.3	67.2%	115	76.2%	0%	53.8	61.0%	93	61.5%	1.8%	61.4	69.6%	126	80.0%	0.1%
45	43.6	70.2%	83	92.0%	0%	36.7	59.0%	75	84.2%	1.6%	35.8	57.6%	72	90.6%	0%
46	33.7	63.5%	67	89.8%	0%	30.1	56.7%	56	75.6%	1.2%	35.7	67.2%	68	89.7%	0.2%
47	62.7	75.9%	93	79.5%	0%	60.1	72.8%	88	75.2%	0.7%	65.7	79.5%	105	81.7%	0.5%
48	70.1	78.7%	108	70.6%	0.2%	65.1	73.1%	101	66.1%	0.8%	73.3	81.9%	125	60.8%	0.1%
49	61.4	83.4%	128	60.4%	0%	58.5	78.8%	117	55.1%	0.4%	58.8	79.8%	129	78.4%	0.1%
50	51.2	79.0%	79	68.2%	0.2%	47.0	72.5%	88	78.5%	1.2%	48.2	74.4%	91	79.5%	0.2%
AVG2[2]	53.0	79.6%	103.6	77.6%	0.04%	47.6	71.0%	94.0	66.7%	1.4%	51.7	77.5%	107.7	79.1%	0.2%
TAVG[3]	59.5	80.5%	118.9	78.1%	0.07%	53.8	71.2%	109.0	70.0%	1.2%	57.9	79.2%	119.2	78.3%	0.2%
p-value	-	-	-	-	-	0.0001	0.0017	0.0024	0.0030	0.0020	0.0487	0.0409	0.0377	0.0445	0.0367

[1] Means of measurements for development dataset.
[2] Means of measurements for testing dataset.
[3] Means of measurements for all examinations.

Table 3.3: Literature comparison of proposed and previous methods. (These references are using different datasets.)

Author	Number of cases	Method	Performance
Tschirren [56]	22	region-growing	27.45±3.75 branches for each case
Feuerstein [68]	20	VOI region-growing	sensitivity: 76.5%
Schlathoelter [69]	1	tube-like enhancement filter	7th generation per case
Lo [59]	15	machine learning region-growing	123 branches per case 51.2% detection rate
Yano [60]	4	local intensity analysis	69.5% rate averagely per case
Kitasaka[67]	3	VOI region-growing	6th generation per case Average for 38% detection rate
Meng [61]	50	machine learning local intensity analysis	Average 79.2% detection per case
Proposed method	50	VOI local intensity analysis	78.1% rate averagely per case

(a) (b) (c)

Figure 3.16: Airway extraction results in a VOI by changing T_{CEF}: (a) -800 H.U. threshold, (b) -810 H.U. threshold, and (c) -820 H.U threshold. When leakage regions are detected in a CEF extraction result, the threshold used in CEF decreased.

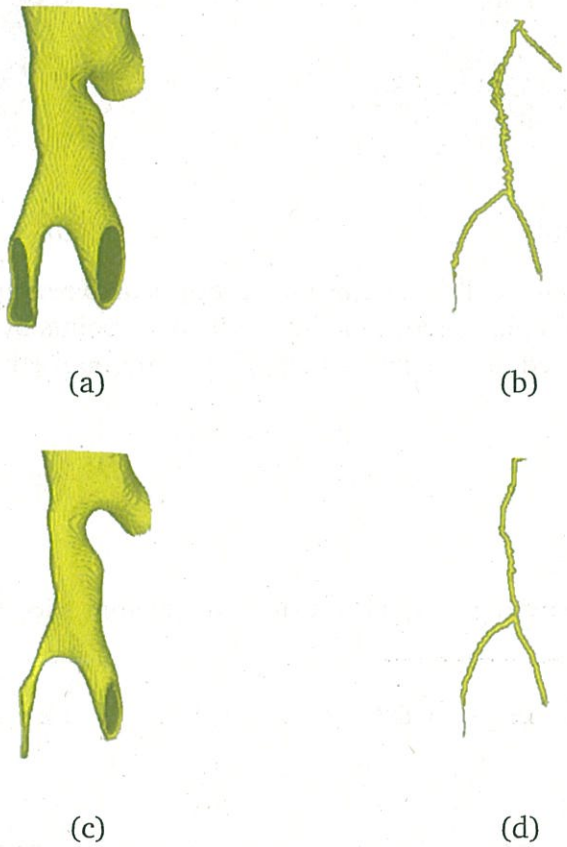

Figure 3.17: Comparison results: (a) one example of CEF extraction result in a VOI after leakage removal, (b) corresponding thinning result of CEF extraction result, (c) central area detected by GVF magnitude and tubular-likeness, and (d) corresponding thinning result of central area.

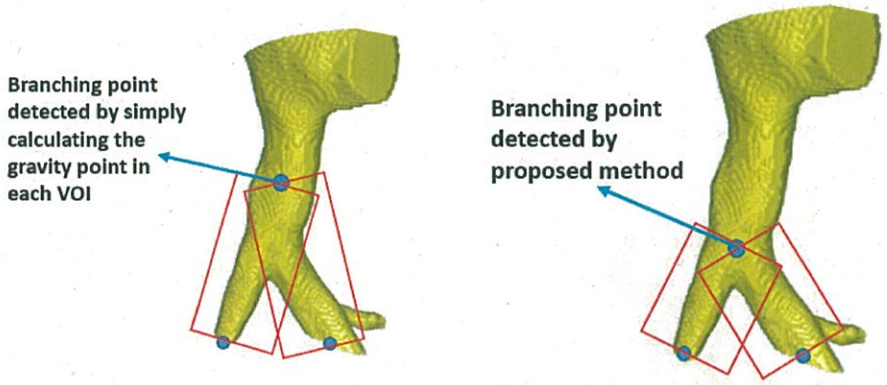

(a) (b)

Figure 3.18: Comparison of child VOI placement results between previous and proposed algorithms: (a) child VOI placement based on branching-points by gravity [67] and (b) child VOI placement based on branching-points by proposed method.

Table 3.4: Average airway segmentation results in different slice thicknesses and pixel sizes

Thickness (mm)	0.625–1.00	1.00–1.25	1.25–2.00
BD	118.5	119.7	119.1
TPR	77.6%	78.3%	77.9%
TL (cm)	58.4	60.7	59.1
TLD	85.1%	88.5%	86.1%
FPR	0.1%	0.07%	0.1%
Voxel size (mm)	0.625–0.750	0.750–0.875	0.875–0.976
BD	119.2	118.8	119.3
TPR	78.0%	77.7%	78.1%
TL (cm)	57.2	60.7	59.4
TLD	83.4%	88.5%	86.6%
FPR	0.1%	0.1%	0.1%

Table 3.5: Literature comparison of proposed and previous algorithms. These references use different datasets. Methods 1, 3, 5, 6, 7, 8 and 9 experimented on private datasets, and methods 2 and 4 experimented based on EXACT'09.

Number	Author	Number	Algorithms	Performance
1	Tschirren [56]	22	Region-growing	27.45±3.75 branches for each case
2	Feuerstein [68]	20	VOI Region-growing	Branch-detection rate: 76.5% Tree length detection: 73.3% False positive rate: 15.56%
3	Schlathoelter [69]	1	Tubular enhancement filter	7th generation per case
4	Bauer [88]	20	Gradient vector flow	Branches detection rate: 63.0% Tree length detection: 58.4% False positive rate: 1.44%
5	Lo [2]	15	Machine learning Region-growing	TPR based on volume overlapping: 98.68% False discovery rate: 24.94%
6	Yano [60]	4	Local intensity analysis	69.5% rate averagely per case
7	Kitasaka[67]	3	VOI Region-growing	6th generation per case Average for 38% detection rate
8	Meng [61]	50	Machine learning Local intensity analysis	Average 78.1% detection per case Average 79.2% rate length detection per case False positive rate: 0.2%
9	Proposed algorithm	50	Volume of interest Local intensity analysis	Average 77.9% rate detection per case Average 80.5% rate length detection per case False positive rate: 0.07%

3.4 Discussion

3.4.1 Advantages of proposed algorithm

We developed an algorithm to automatically segment airway trees in the lung region from 3D chest CT volumes and evaluated its performance on 50 chest CT volumes utilizing the local volume of interest, the local intensity analysis, the airway contour circularity, and the GVF. Compared to the previous algorithms, this algorithm has the following advantages: 1) unlike the traditional region-growing algorithm, our proposed algorithm uses VOI to wrap the airway regions for precise segmentation of the airway tree, which avoids extensive leakages in the lung area; 2) our proposed algorithm utilizes CEF instead of the region-growing algorithm to extract the airway region in each VOI and detects tubular structures more effectively; 3) we use a leakage region detection scheme that utilizes two metrics to detect the leakage and effectively avoids the leakage regions. Our proposed algorithm can extract more peripheral bronchi, which the previous algorithm [67] failed to do. Moreover, it inevitably generated leakage due to the partial volume effect (PVE) in it. Considering Table 4.2, our proposed algorithm outperformed the previous work based on VOI and region-growing-based work [67] in terms of BD, TPR, TL, and FPR. From Table 4.2, our proposed algorithm showed better results than the previous algorithm based on local intensity analysis and machine learning [61] in terms of TL and FPR. To visually demonstrate the performance of our scheme, we listed a set of segmentation results from each group as "high," "moderate," or "poor" levels of performance and compared them with two previous methods [61, 67] and the ground-truth data (Fig.3.14). According to Fig. 3.14, the previous method results in some disconnections in the airway extraction results and incomplete airway tree reconstruction [61]. Since our proposed method solved this problem, it is indispensable for such clinical applications as bronchoscope navigation.Table 3.5 summarizes the literature comparisons of our proposed algorithm against other approaches based on several algorithms that have been developed so far. Table 3.3 shows an indirect way to compare the performance of our scheme with other approaches. Compared

with these methods, our scheme tended to be comparable to or better than most in terms of the airway branch-detection and airway length-detection rates, although we emphasize that our results are based on a different, private dataset.

3.4.2 Effectiveness of local intensity structure analysis

Compared to the previous algorithm, which uses local intensity analysis and machine learning [61], our proposed algorithm can extract connected airway branches without generating any disconnections. CEF effectively detects cavity-like structures and is robust to the clinical noise levels we observed in our CT volumes. In pre-processing, any noise was reduced by sharpening filter based on the Laplacian of Gaussian. Fig. 3.15 shows the cross-section slices in a VOI image with three different results: region-growing result in a VOI, local intensity analysis and selected by a machine learning technique, and the CEF in a VOI. According to Fig. 3.15, the CEF-based algorithm extracts more airway regions in a VOI than the two previous algorithms [61, 67] and more complete airway regions than the previous method [61].

3.4.3 Effectiveness of leakage detection function and GVF

Compared to the previous algorithm [67], our proposed algorithm uses a leakage region detection scheme that effectively removes the leakage regions in each VOI. The proposed leakage region detection scheme is not only based on calculating the ratio between the extracted area of the airway regions on the VOI surface and the total VOI area; it also considers the shape information of the airway contours. By considering the contour circularity of the airway branches, this scheme can more precisely detect the leakage regions in each VOI. As seen in Fig. 3.16, the leakage regions can be removed by decreasing the threshold in CEF after detecting the leakage region in the VOI. This shows that an adaptive threshold value adjustment of T_{CEF} adequately prevented the leakage region and maximized the airway region.

We use GVF in branching-point detection. One GVF property is that it is sensitive for extracting the central areas of tubular structures. Furthermore, we utilized the tubular-

Table 3.6: Average smoothness of centerline obtained in each VOI by proposed and previous methods

Method	Previous method [67]	Proposed method
Mean curvature	0.21	0.18

likeness function, which is based on GVF, to extract the candidate center region and a thinning process on the extracted candidate center area to obtain the centerline and branching-points. Since this algorithm is more precisely based on the anatomical knowledge of airway branches than simply calculating the gravity of each airway area in each VOI, it gives a more accurate starting point of the child VOIs for the next level. From Fig. 3.17, the centerline obtained by our proposed algorithm is obviously smooth, and bifurcation points can be detected more easily from the centerline obtained by it. Some spurious branches are omitted by the proposed algorithm, and the centerline becomes much smoother. We calculated the smoothness by computing the local mean curvature [99]. Table 3.6 shows the smoothness of the centerline obtained by the proposed and previous methods. The mean curvature of the proposed method decreased more than the proposed method, which means that the smoothness of the centerline in the proposed method is higher than in the previous method. According to Fig. 3.18, the child VOI placement of the previous algorithm is less accurate than the proposed algorithm because the proposed algorithm uses GVF for centerline extraction and generated a natural centerline. After obtaining a smooth centerline, it is easy to obtain a more precise branching-point than simply computing the airway regions gravity region. With a precise branching-point, the direction of the child VOI becomes more accurate.

3.5 Conclusion

We developed a method to extract bronchus regions from 3D chest CT volumes using the structural features of the bronchus. This method extracted each bronchial branch by tracing the bronchial tree by VOIs. During the tracking, a leakage detection function,

which uses airway contour circularity, prevented leakage occurrence in each VOI. For the generation of VOIs in the next level, we basically used GVF to extract the centerline area. Subsequently, we used a thinning process to obtain the centerline and the next branching-points. This guides the extraction of branches in the next level. Although our proposed method shows promising extraction performance with significantly decreased FP regions, FP regions remain. Future work will use the segmentation results to support a bronchoscope navigation system. This proposed method can extract the complete airway candidate branches but the extraction rate is not so high. How to extract the peripheral airway branches is in the future work.

Chapter 4

Tracking and segmentation of the airways in chest CT using a fully convolutional network

Based on the work in Chapter 3, it can be seen that this method can extract the peripheral airway branches, but the detection rate is not improved significantly. To increase the detection rate, the fully convolutional network is used combined with the VOI-based airway segmentation method to extract the peripheral airway branches.

This paper introduces a method that combines 3D deep learning with image-based tracking in order to automatically extract the airways. Our method is driven by adaptive cuboidal volume of interest (VOI) analysis using a 3D U-Net model. We track the airways along their centerlines and set VOIs according to the diameter and running direction of each airway. After setting a VOI, the 3D U-Net is utilized to extract the airway region inside the VOI. All extracted candidate airway regions are unified to form an integrated airway tree. We trained on 30 cases and tested our method on an additional 20 cases. Compared with other state-of-the-art airway tracking and segmentation methods, our method can increase the detection rate by 5.6 while decreasing the false positives (FP) by 0.7 percentage points. This paper is published in International Conference on Medical Image Computing and Computer Assisted Intervention (MICCAI) 2017

During the bronchoscope navigation surgery, the guidance for the physician is quite important. Therefore, the complete extraction of the airway tree is very essential. The

previous method track the airway tree along the centerline in VOI and integrated them as an complete airway tree. However, the previous method can extract most of the airway region, there are still some false negative regions. The extraction of the airway regions in the next level rely on the extracted region in the VOI in the last level. If the bronchus regions are not extracted well in the last level, the tracking of the airway tree will stop. In the proposed method, we used the deep learning technique to replace the region growing and cavity enhancement filter to extract the airway regions in each VOI. The 3-D U-Net is very sensitive to the peripheral region than the traditional region growing method and enhancement filter.

4.1 Introduction

In recent years, fully convolutional networks (FCN) have outperformed the state-of-the-art in many segmentation tasks [100]. U-Net is one example that consists of a contracting encoder part to analyze the whole image and a successive decoder part to generate an integrated segmentation result [101]. 3D U-Net is the 3D extension of U-Net that replaces all 2D operations with their 3D counterparts [102].

In this paper, we build upon a method to segment the airway by using FCN within the VOI tracking framework [67]. The main contribution of our proposed work includes the implementation of 3D U-Net in the selected VOI tracking along the centerlines of the airway. At the same time, the segmentation results can be used to predict airway extraction in the next branching level. Compared to other state-of-the-art airway tracking and segmentation methods, our proposed method can increase the detection rate and reduce the false positive (FP) rate.

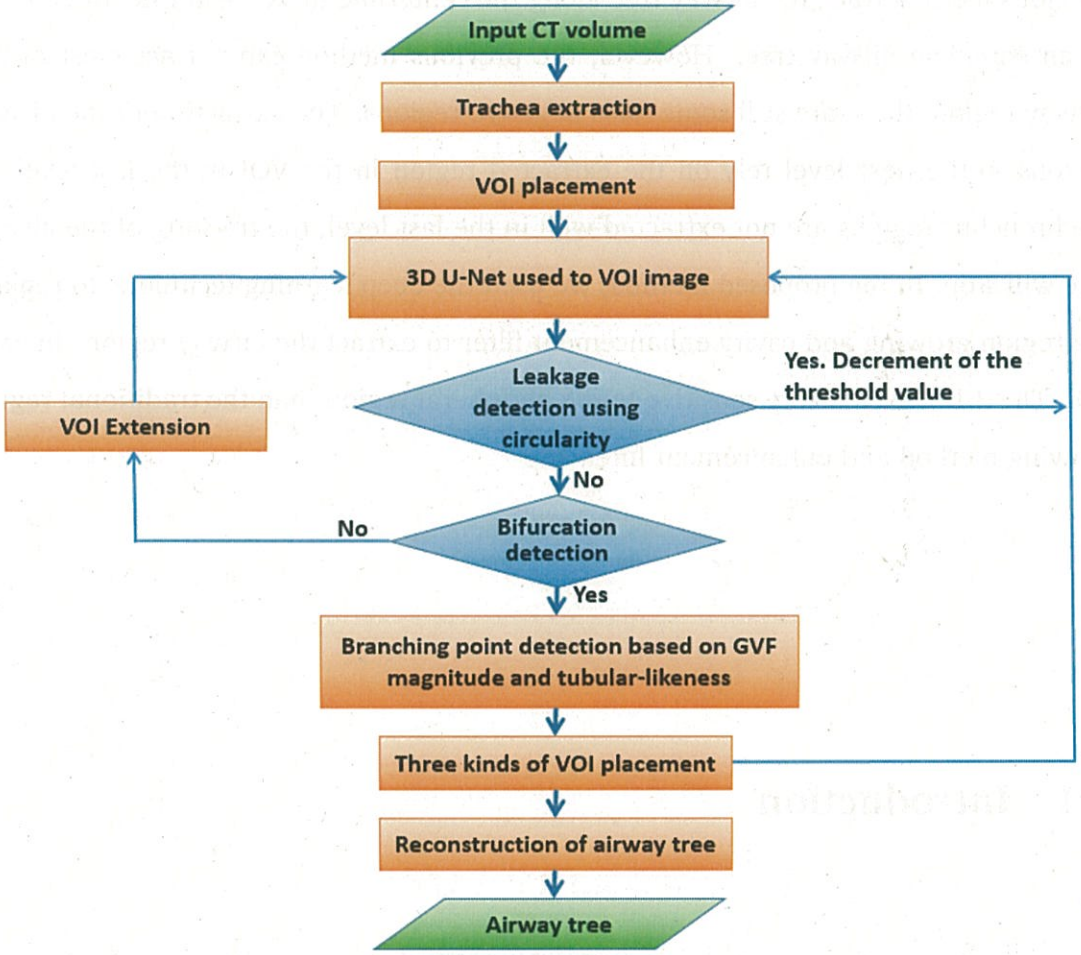

Figure 4.1: Flowchart of the proposed method

4.2 Methods

4.2.1 Overview

Figure 4.1 shows the workflow of our method. Firstly, we segment the trachea region by region growing by a predefined threshold value. After obtaining the initial trachea regions, the initial VOI based on the segmented result was established. After setting the initial VOI, 3D U-Net is then used to segment the airway region sequentially. The different VOIs for each level were set according to some rules. To implement the 3D U-Net to obtain the bronchus regions, three different kinds of VOI of different sizes are

set. Two of them were used as the input and output of the 3D U-Net. And one of the VOIs is used in the airway tracking algorithm. The size of the input volume of the network is $132 \times 132 \times 116$ voxels. The output volume is $44 \times 44 \times 28$ voxels. The size of the VOIs is dynamically adjusted in the airway tracking algorithm depending on the diameter of the bronchi.

4.2.2 3D U-Net based airway tracking algorithm

The employed network architecture is the 3D extension of U-Net proposed by Ronneberger et al [101], which was initially utilized for biomedical image analysis. While U-Net is an entirely 2D architecture, the network utilized in this paper applied all the operations in their 3D version, such as 3D convolutions, 3D max pooling, and 3D up-convolutions [102]. We use the open source[1] implementation of 3D U-Net developed in Caffe [103]. The 3D U-Net architecture consists of an analysis and a synthesis path with four resolution levels each. Each resolution level in the analysis path contains two $3 \times 3 \times 3$ convolutional layers, each followed by rectified linear units (ReLu), and then a $2 \times 2 \times 2$ max pooling with strides of two in each dimension. In the synthesis path, the convolutional layers are replaced by up-convolutions of $2 \times 2 \times 2$ with strides of two in each dimension. These are followed by two $3 \times 3 \times 3$ convolutions each with a ReLu. Furthermore, 3D U-Net employs shortcut (or skip) connections from layers of equal resolution in the analysis path in order to provide higher-resolution features to the synthesis path [102]. The last layer contains a $1 \times 1 \times 1$ convolution that reduces the number of output channels to the number of class labels which is K = 2 in our specialized airway extraction case. The model can be trained to minimize a newly introduced weighted voxel-wise cross-entropy loss:

$$\mathcal{L} = \frac{-1}{N}\left\{\lambda \times \left(\sum_{x \in N_0} \log\left(\hat{p}_k(x)\right)\right) + (1-\lambda) \times \left(\sum_{x \in N_1} \log\left(\hat{p}_k(x)\right)\right)\right\}, \tag{4.1}$$

where $\hat{p}$ are the softmax output class probabilities.

λ is a weight factor, N are the total number of voxels x, and $k \in [0, 1]$ indicates

[1] http://lmb.informatik.uni-freiburg.de/resources/opensource/unet.en.html

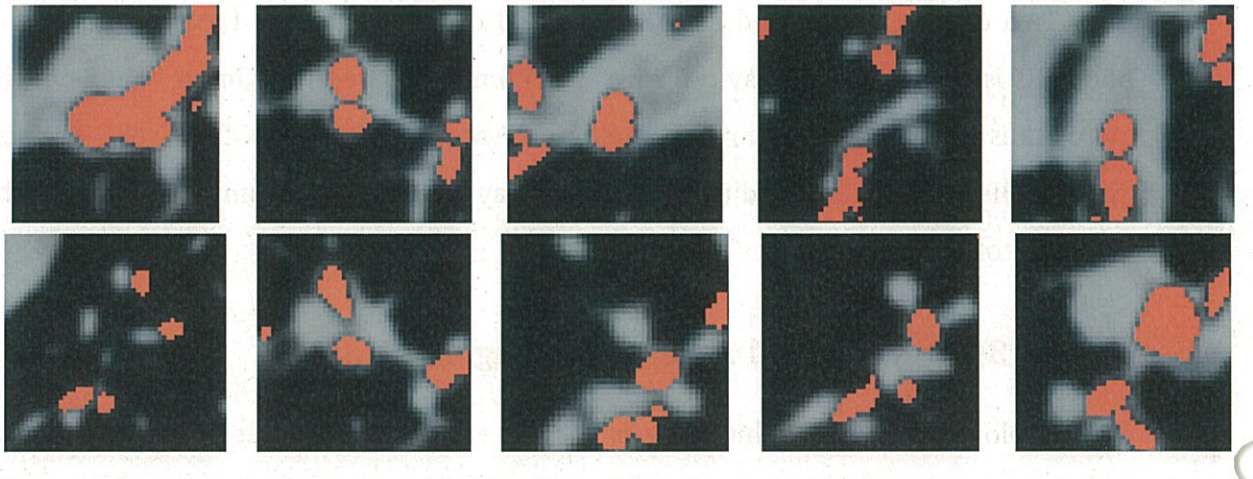

Figure 4.2: Extraction results by 3D U-Net.

the lung tissue label of the airway region and the ground truth of the airway regions. The input to this loss function are real valued predictions $x \in [-\infty, +\infty]$ from the last convolutional layer. We apply weight λ to the loss function (Eq. 4.1) in order to balance the lung tissue as background with respect to the airway regions as foreground. We choose λ with $\lambda = \frac{N_1}{N}$, where N is the number of voxels for the lung region, and N_1 corresponds to the number of airway (foreground) voxels. Fig. 4.2 shows examples of airway region extraction by 3D U-Net.

4.2.3 VOI placement

Due to the requirement of 3D U-Net, three kinds of VOIs are defined. Figure 4.3 shows the three kinds of VOI. One is the V_{TRACK} which is set to contain a bronchial branch in the airway tracking algorithm. Since the 3D U-Net requires a constant size of images as input, we prepare two wider VOIs, V_{SEG} and V_{3DU}. The V_{SEG} of 3D U-Net with a size of $44 \times 44 \times 28$ voxels is used to save the segmentation output of 3D U-Net. The V_{3DU} is used as the input of 3D U-Net for training and testing with a size of $132 \times 132 \times 116$ voxels. The height of the VOI is 28 voxels, and the length and width is twice the average diameter of the airway regions. We resample the segmentation result from V_{SEG}, save it in V_{TRACK}, and reconstruct all of the candidate airway regions sequentially to form

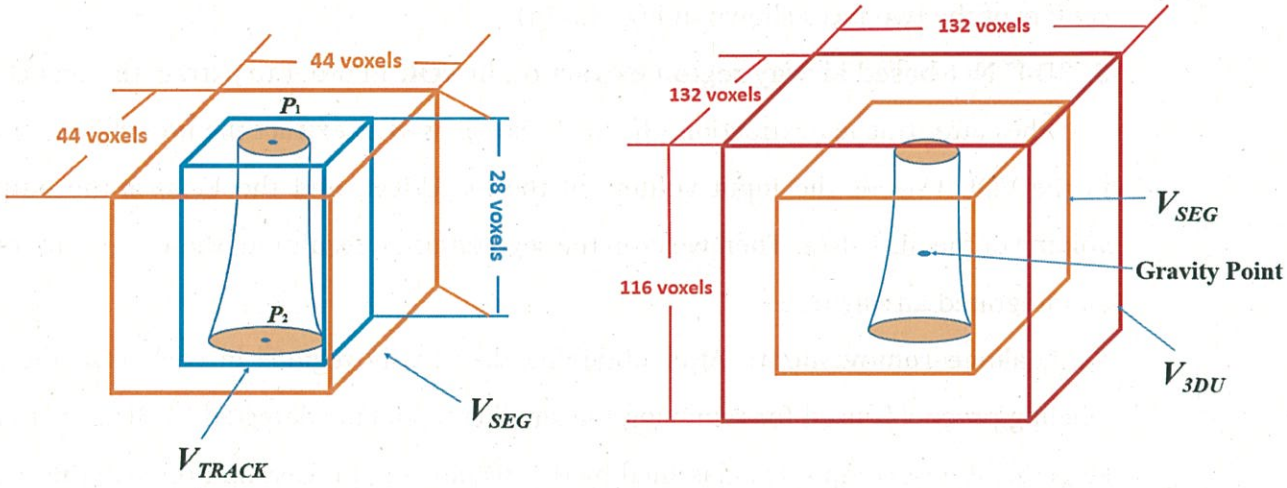

(a) (b)

Figure 4.3: Illustration of three different kinds of VOI. (a) shows that V_{SEG} and V_{TRACK} have the same original point. The orange VOI is V_{SEG}, and the blue VOI is the V_{TRACK}. (b) shows that V_{3DU} corresponds to V_{SEG}. The red VOI is V_{3DU}.

an integrated airway tree.

4.2.4 Airway tracking algorithm

We introduce the 3D U-Net in VOI-based airway tracking algorithm (3DU-VOI) in this section. The airway tracking algorithm starts to place a VOI at the trachea and the airway trees are segmented to place child VOIs from the root along the centerline. In each VOI, an airway region is extracted by 3DU-VOI. The size of each VOI is determined according to the diameter of airway regions. The VOI direction is determined by the centerline extracted in the last VOI. The explanation of the airway tracking algorithm is outlined as follows:

1. Trachea extraction: A trachea region is roughly segmented by a method similar to [65]. The threshold value used in the region growing method is manually determined to extract the trachea region.

2. VOI placement: A VOI is defined as a cuboid with eight vertices and two points: original point $\mathbf{P}_1$, which determines the position of the VOI, and $\mathbf{P}_2$, which are the

centers of the two faces shown in Fig. 4.3 (a).

3. 3D U-Net-based airway region extraction in VOI: In order to extract the bronchial branches after trachea extraction, the 3D U-Net is used to extract the bronchial regions in the VOI. V_{3DU} is the input volume of the 3D U-Net, and the V_{SEG} is the output volume of the 3D U-Net. Then we crop the segmentation result into the V_{TRACK} to form an integrated airway tree.

4. Leakage removement: After obtaining the airway regions in each VOI, the 3D labeling process is used for removing the small components detected by 3D U-Net. We keep the largest component classified by the 3D labeling process and remove the small components.

5. Furcation detection: The furcation regions are detected by analyzing the number of the connected components on the VOI image surface. The number of connected components indicates the number of furcations. The following conditions will be checked iteratively in each VOI:

- $N_c = 0$ In this VOI, there is no bronchus region to be detected, and the tracing will be terminated.
- $N_c = 1$ In this VOI, furcation hasn't been detected, but the bronchial region is continued to be traced.
- $N_c = 2$ or 3 In this VOI, the bifurcation and trifurcation has been detected.

6. VOI extension: We extend the VOI to the bronchus running direction by one voxel. After that the Step (3) is processed again.

7. Branching point detection: We apply the gradient vector flow (GVF) magnitude and tubular-likeness function based on GVF to extract the centerline [88]. The branching point is detected based on this centerline.

8. Child VOI placement: After the branching point detection, the child VOIs V_{TRACK} are placed based on the branching point detected and the center points of the components on the VOI surface. Except for V_{TRACK}, the V_{3DU} and V_{SEG} are placed for the 3D U-Net. After the child VOI placement, the extraction procedure is repeated [62].

Table 4.1: Comparison of segmentation results for airway tree in 20 chest CT examination volumes between the sliding-window-based U-Net and tracking-based U-Net in a sliding-window fashion.

DSCs	SW U-Net	Tracking U-Net
Mean	68.7%	86.6%
Std	20.6%	5.9%
Min	22.4%	75.9%
Max	83.6%	98.6%
FPR	SW U-Net	Tracking U-Net
Mean	0.209%	0.017%
Std	0.075%	0.013%
Min	0.077%	0.001%
Max	0.403%	0.053%

9. **Airway tree reconstruction:** Finally, we reconstruct all of the candidate bronchus region to form an integrated airway tree.

4.3 Experiment & Results

To evaluate our proposed method, we used 50 clinical CT scans acquired with standard dose. The size of each slice scan was 512×512 pixels with a pixel size in the range of 0.625 - 0.976 mm. The number of slices in each dataset ranged from 239 to 962 slices with varying thicknesses from 0.625 to 2.00 mm. The data set was randomly divided into two groups: the training data set which contains 30 cases and the testing data set containing 20 cases. We performed two comparisons. A comparison between the results of airway tracking algorithm with 3D U-Net and the results of only using 3D U-Net in a sliding-window approach without the tracking information. Sliding-window U-Net method means randomly generating the sliding window around the candidate regions obtained by dilating the ground-truth data by ten voxels. Two indices are used for evaluation: (a) Dice Similarity Coefficients (DSCs) , (b) false positive rate (FPR), the number of extracted voxels which were not bronchial voxels according to ground truth. The results are given in Fig. 4.4 and Table. 4.1.

We also compared our proposed method with two methods, one is Kitasaka's method [67] based on the VOI and region growing, and the other is Meng's method based on

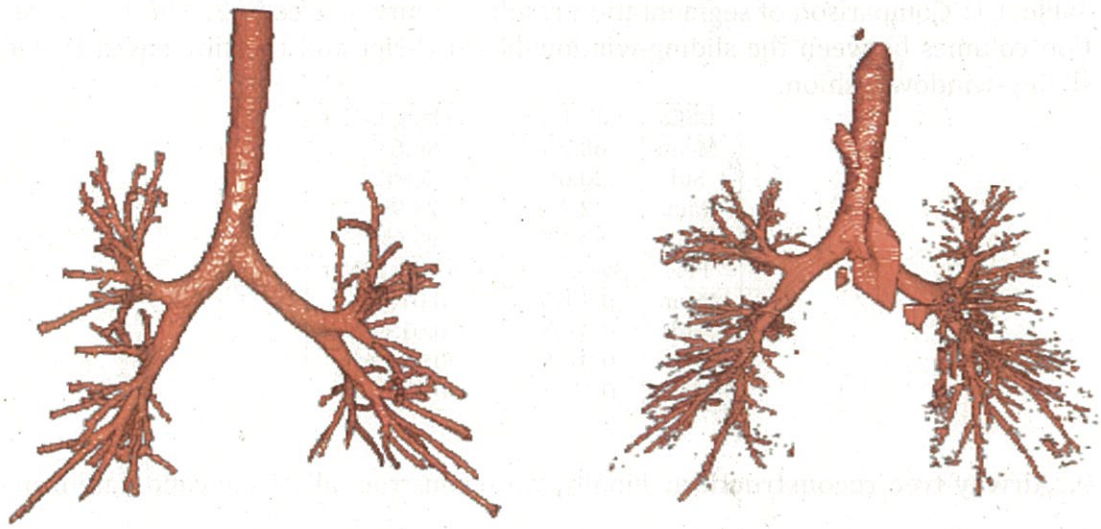

(a) (b)

Figure 4.4: Comparison between the result of airway tracking algorithm with 3D U-Net and the result of only using 3D U-Net.

local intensity analysis and machine learning technique [61].The segmentation results, yielded by applying our proposed method to each of the 20 chest CT examinations, are provided in Table 4.2.

We measured three indices for evaluation: (a) number of branches extracted, (b) true positive rate (TPR), the ratio of extracted branches and total number of branches and (c) computing the false positive rate (FPR), the false branches which don't belong to ground truth, (d) Dice Similarity Coefficients (DSCs).

Training : In the training phase, we input both of the 3D CT volumes selected from the lung area and the corresponding ground truth data sets. We dilated the ground truth data by ten voxels as the candidate regions, and randomly selected the subvolume images inside the candidate regions. Data augmentation with random 3D rotations at 360 degree was done on-the-fly, which results in 35 k images simulating tracking iterations. Training on 30 cases took 2 days for 35 k iterations on a NVIDIA GeForce GTX TITAN X with 12 GB memory, and one iteration generates one subvolume image.

Testing : We obtained the V_{3DU} in the airway tracking algorithm. After fixing the

Table 4.2: Comparison of segmentation results for airway tree in 20 chest CT examination volumes. Here, TPR and FPR denotes the true positive and false positive rate of detected branches, respectively. DSCs is the Dice similarity score. (Note: The ground truth data was generated manually and BD indicates branch detection.)

Case	Proposed method				Kitasaka et al. [67]				Meng et al. [61]			
BD	TPR	FPR	DSCs	BD	TPR	FPR	DSCs	BD	TPR	FPR	DSCs	
1	114	85.1%	0.3%	86.7%	110	82.1%	1.8%	85.9%	116	86.6%	0.2%	58.9%
2	71	80.7%	0.2%	92.2%	58	65.9%	0.6%	79.7%	68	77.3%	0%	81.0%
3	142	71.7%	0.1%	89.3%	137	72.9%	0.7%	89.0%	140	70.7%	0.2%	78.4%
4	106	88.3%	0.2%	97.0%	97	80.8%	1.3%	85.1%	103	85.8%	0.2%	85.1%
5	82	96.5%	0.2%	87.2%	77	90.6%	0.7%	82.5%	80	94.1%	0.2%	82.6%
6	98	89.1%	0.1%	85.1%	85	77.3%	0.8%	85.1%	92	83.6%	0.1%	95.5%
7	95	72.5%	0.2%	80.2%	88	67.2%	0.9%	69.5%	91	69.5%	0.5%	95.2%
8	36	73.5%	0.2%	91.4%	30	61.2%	0.4%	80.2%	28	57.1%	0%	84.8%
9	'58	77.3%	0.2%	86.8%	55	73.3%	0.6%	86.8%	54	70.1%	0.2%	86.9%
10	153	89.5%	0.1%	76.8%	149	87.1%	0.6%	80.7%	151	88.3%	0.1%	85.1%
11	101	84.2%	0%	75.9%	98	81.7%	0.4%	75.9%	102	85.0%	0.6%	70.1%
12	92	77.3%	0%	90.9%	95	79.8%	0.3%	90.9%	93	78.2%	0.2%	96.2%
13	89	68.9%	0.2%	87.5%	93	72.1%	1.6%	89.6%	91	70.5%	0%	80.2%
14	111	87.4%	0%	83.2%	108	85.0%	0.5%	85.1%	106	83.5%	0.2%	95.4%
15	54	90.0%	0.1%	80.3%	48	80.0%	1.1%	72.0%	52	86.7%	0%	85.1%
16	37	82.2%	0.2%	82.4%	31	68.9%	0.5%	70.3%	33	67.3%	0.2%	82.6%
17	33	67.3%	0%	98.6%	28	57.1%	1.7%	98.9%	30	61.2%	0.1%	96.7%
18	80	66.7%	0.1%	85.5%	76	63.3%	1.1%	85.5%	75	62.5%	0.1%	91.4%
19	81	61.8%	0.1%	88.3%	75	57.3%	0.3%	88.3%	82	62.6%	0.1%	98.9%
20	57	82.6%	0%	86.3%	52	75.4%	1.4%	86.3%	55	79.7%	0.5%	85.5%
AVG	84.5	79.6%	0.1%	86.6%	79.5	74.0%	0.8%	83.3%	82.1	76.0%	0.2%	86.0%
p-value	-	-	-	-	0.0027	0.0126	0.0015	0.011	0.0014	0.0013	0.0375	0.045

size and direction of the V_{3DU}, we input V_{3DU} into the trained network to obtain the candidate airway areas and save them into V_{SEG}. After that, we re-sampled the V_{TRACK} used in the airway tracking algorithm by cubic spline interpolation.

Figure 4.5 shows the evaluation results by the proposed method, as well as comparison with two other methods [67] and [62].

4.4 Discussion

According to the Fig. 4.4 and Table. 4.1, it can be seen that the result of 3D U-Net in sliding-window can extract many peripheral bronchi but also generate many false positive (FP) regions as well. It is apparent that the proposed method can extract many peripheral bronchi and avoid the FP regions effectively. The 3D U-Net is effective to detect the peripheral bronchi in the chest CT images, however it produces many FP detections when applied in a straight-forward sliding window approach as proposed

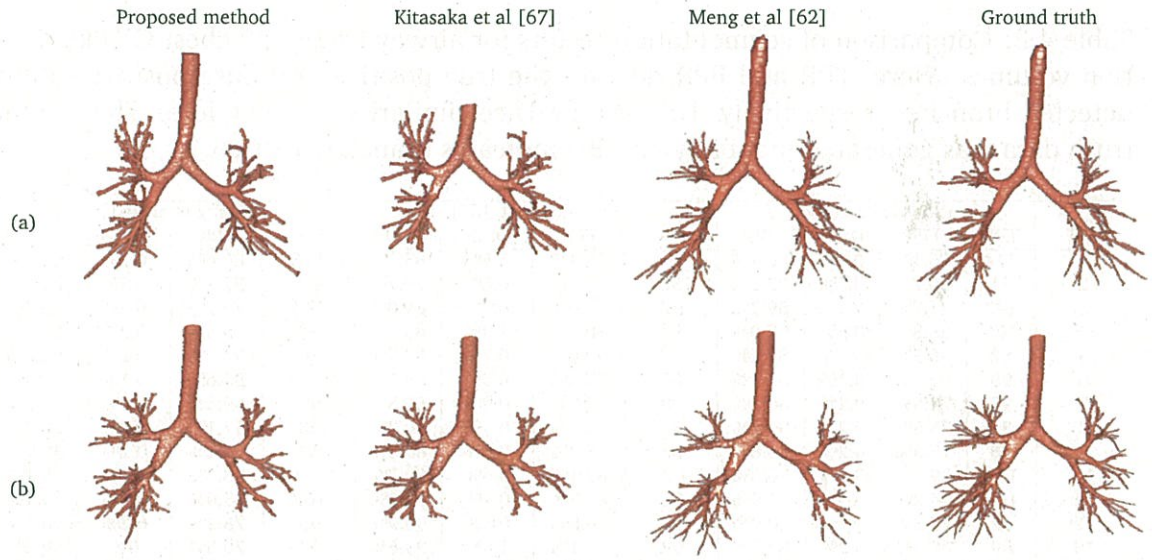

Figure 4.5: Comparison of airway segmentation results of the proposed, previous methods [67],[62], and ground truth. Upper and lower rows show the results of Case 3 and 8, respectively.

in [102]. After combining the 3D U-Net with the airway tracking algorithm, the false positive regions can be decreased significantly. Table 4.2 and Fig. 4.5 demonstrate that our proposed method outperforms the the other two methods. To further illustrate the application results of our proposed method, we show a set of automatic airway segmentations in Fig. 4.5, which illustrates that our proposed method can extract more peripheral bronchi than the method by Kitasaka et al. [67] and can extract more integrated branches than Meng et al. [62]. Our proposed method utilizes 3D U-Net to extract the airway region in each VOI, which effectively extracts the bronchus region and avoids leakage.

4.5 Conclusion

This paper introduced an effective integration of 3D U-Net into airway tracking and segmentation in combination with VOI-based algorithm. The proposed method was possible to improve segmentation accuracy significantly. Due to the memory restriction of the GPU, the input volume size to the network is fixed. In the future, networks with

dynamic input sizes can be explored.

Chapter 5

Conclusions and future works

This chapter concludes the accomplishments that the previous three chapters have discussed. Then, the benefits and limitations of these three proposed methods are discussed in section 5.2. Finally, we discuss some promising directions for future work to further address the development of the chest CAD system.

5.1 Summary

This dissertation introduced an automated segmentation method of airway segmentation. Then, four different parts were described in this dissertation.

(1) Chapter 1 presented a brief introduction on the background of the medical context that motivates this thesis, which includes the main medical background of our research includes lung anatomy, airway anatomy, and the corresponding CAD and CAS system for the assistance of treatment. At the same time, the history of airway segmentation method development is introduced, and each disadvantage of each method is analyzed. An outline of the thesis and a list of contributions were also given in the end of this chapter.

(2) This dissertation has described a filter-based and machine learning-based methodology for segmentation of airway tree (Chapter 2). This method utilized the line enhancement filter and multi-scale cavity enhancement filter successively to extract the airway-like structure in the chest CT volume. These two enhancement

filters have good performance in detection of candidate airway tree regions, but usually generate many FPs. The goal of using the machine learning technique is to reduce the false positive regions to provide low number of FPs per case with keeping high sensitivity. Since the FPs mainly occur at the regions among the blood vessel and other tissues which has a similar intensity distribution with the airway area, the key point is how discriminate the false positive regions with the bronchus regions. To deal with such problem, the proposed method incorporates the support vector machine (SVM) technique to reduce the FPs. After the false positive regions are removed, the graph-cut algorithm is used to refine all of the candidate regions selected.

The results using clinical chest CT images (50 CT images with 25 training cases and testing cases) showed that the proposed method is sufficient to extract the airway tree.

(3) This dissertation has described a novel method for the automated segmentation of airway tree based on volume of interest and gradient vector flow (Chapter 3). This is the paper that introduces an airway segmentation method based on the volume of interest (VOI) using gradient vector flow (GVF). The proposed method utilizes the cavity enhancement filter (CEF) in the VOI to segment each branch. Then, a tubular-likeness function based on GVF and GVF magnitude map in each VOI to assist the position and direction of the next VOI. Based on the GVF magnitude map and tubular-likeness function, a center-line is extracted. Based on this extracted centerline, we can detect the branch points of the bifurcations as well as the directions of the airway branches in the next level. During the process of the extraction in each VOI, a leakage detection process is performed based on both of the pixel and the shape information of the extracted airway candidate regions. By applying the proposed methods to 50 CT images, very promising airway segmentation results were obtained.

(4) This dissertation has described a novel method for the airway tree segmentation based on both volume of interest and fully convolutional network (FCN). This is the first paper that combines the deep learning technique and the airway tracking algorithm. In recent years, deep learning based methods, especially fully convolutional networks (FCN), have improved the state-of-the-art in many segmentation tasks. 3D U-Net is an example that optimized for 3D bio-medical imaging. While 3D U-Net can be trained for any 3D segmentation task, its direct application to airway segmentation is challenging due to differently sized airway branches. In this work, we combine 3D deep learning with airway tracking algorithm to extract the integrated airway tree automatically. Our method is driven by adaptive cuboidal volume of interest(VOI) analysis using a 3D U-Net model. We track the airways along their centerlines and set VOIs according to the diameter and running direction of each airway. After setting a VOI, the 3D U-Net is utilized to extract the airway region inside the VOI. All extracted candidate airway regions are unified to form an integrated airway tree. We trained on 30 cases and tested our method on an additional 20 cases. Our proposed method shows very promising airway segmentation results.

5.2 Benefits and limitations

5.2.1 Benefits

(1) **Airway segmentation based on local intensity filter and machine learning:** Our research on the automatic airway segmentation based on local intensity filter and machine learning technique is more sensitive to the bronchus-like structure in the lung area and does not suffer from leakage. The Hessian matrix analysis and multi-scale cavity enhancement filter can detect the tube-like structures effectively; however, there are many tissues in the lung area with similar tube-like structure as the airway. The multi-scale cavity enhancement filter can detect the airway regions effectively. Due to the similar intensity distribution of the tissues

in the surrounding lung parenchyma, there are many FPs in the extraction results of the Hessian matrix analysis and the adaptive multi-scale CEF. To remove these FPs, machine learning technique can be used to remove the FPs. Based on the differential attribute of these two different regions, utilizing the local intensity structure-based features and the SVM classifier, we can remove the FP regions effectively. This paper extract the airway candidate regions well and also delete the false positive regions effectively.

(2) **Airway segmentation from 3D chest CT volumes based on volume of interest using gradient vector flow:**

This paper introduces a method that combines the volume of interest and cavity enhancement filter to extract the integrated airway tree. In this paper, the volume of interest is used to wrap the airway region for extracting airway branches. The shape information is used to reduce the leakage regions in each VOI effectively. The shape of airway region contour on the front surface of VOI is effective to identify the false positive regions in each VOI. At the same time, the GVF magnitude map and the tubular-likeness function based on GVF are utilized to extract the center-line and the branching point, which can predict the position and direction of child branches. The experimental results confirmed that the proposed airway segmentation method can extract the airway tree with high accuracy and integrated branches, this solve the problem and drawback in the first method. This method can extract the complete airway branches.

(3) **Tracking and segmentation of the airways in chest CT using a fully convolutional network:**

This paper introduces a method that combines the volume of interest and deep learning technique to extract the airway. By utilizing the enhancement filter, the peripheral airway branches can be extracted, but not complete. This method is an advanced version of second method. It utilizes the 3D U-Net to track the airways along the centerline, and integrated them into a completed airway tree. The ex-

perimental results confirmed that the proposed method can extract more peripheral branches than the second method. This method can extract more complete and peripheral airway branches.

5.2.2 Potential limitations

Although the proposed methods introduced in this dissertation provides various significant improvements over previous methods, all of the segmentation methods have their own limitations.

5.2.2.1 Limitations of the first method

The proposed segmentation methods have three main limitations as follows:

(1) This proposed method needs to use the ground-truth dataset to train the classifier, without the ground-truth dataset, the proposed method can't delete the false positive regions automatically. And due to the utilization of the SVM classifier, some of the bronchial regions are deleted, which makes the branches have many breaks and the airway tree in-completed.

(2) The proposed method fails to extract some of the peripheral bronchi with diameter of only 1 or 2mm. The reason for missing some small peripheral airway branches involves: many thin bronchi with 1 or 2 voxels in their diameter cant be extracted by adaptive multiscale CEF due to the smallest radius R used to compute the CEF, which is set to 3, therefore the thin bronchi with 1 or 2 voxels in their diameter can not be extracted properly. And we also gave a threshold value for selecting appropriate candidate voxels, some of the candidate bronchi regions are also deleted.

5.2.2.2 Limitations of the second method

The proposed airway extraction method based on volume of interest have several potential limitations as follows:

Acknowledgements

Although the pursuit of a doctorate degree is generally an enjoyable experience, it is also a lengthy, rigorous, and often painful process with bitterness, hardships, and frustration. Fortunately, so many people intervene with this process by providing their encouragement, trust, and kind assistance to me. Despite that it will never be sufficient to express my gratitude in words to all those people who assisted me, I would still like to give deep and sincere thanks to all of those people during my almost four years journey in Nagoya.

I would like to express my great appreciation to my supervisor, Prof. Dr. Kensaku Mori, who makes my study in Japan possible. Without his instruction, encouragement, and support, I will not finish my doctoral course. He is a good instructor and give me a lot of suggestions and makes the great effort to make me obtain lots of progress. Meanwhile, his knowledge in computer-aided detection/diagnosis and abundant undergo have given many assistance to me and we have had lots of discussions on my doctoral topics. Warm thanks are given to Assistant Prof. Dr. Masahiro Oda for his advises of my work.

Then I also give my thank to Prof. Dr. Hiroshi Murase for his willing to be my thesis reviewer. I also feel grateful to Prof. Dr. Hirokai Kudo who gave many useful and practical comments and also would like to review my thesis.

I owe my sincere gratitude to Prof. Dr. Takayuki Kitasaka for his helpful advices and discussion since 2014. Without his help, I can't finish my doctoral course.

I would like to thank the secretaries of Mori laboratory, Rie Ohashi and Yumiko Kobayashi for their hard work in my conference trips. I want to give all of my appreciation to all my colleagues in Mori laboratory.

I also thank to all the organizations, which gave me sponsoring, including the top

Global University Project and JASSO scholarship. With their financial help, I can finish my doctoral thesis completely and successfully.

Finally, I want to thank my mother, Xiaoxia Meng, and my ex-boyfriend, Dr. Wang who gave the support to me at the beginning of my study. Also for their big love, thorough understanding, endless patience, and never failing faith in me.

Publications

[J1] **Qier Meng**, Takayuki Kitasaka, Yukitaka Nimura, Masahiro Oda, Junji Ueno, Kensaku Mori. *Automatic segmentation of airway tree based on local intensity filter and machine learning technique in 3D chest CT volume*, International Journal of Computer Assisted Radiology Surgery (2017), Vol.12, No. 2, pp 245261, DOI: 10.1007/s11548-016-1492-2. SCI Index

[J2] **Qier Meng**, Takayuki Kitasaka, Masahiro Oda, Junji Ueno, Kensaku Mori. *Airway segmentation from 3D chest CT volumes based on volume of interest using gradient vector flow*, Medical Imaging Technology (2018)

[C1] **Qier Meng**, Holger Roth, Takayuki Kitasaka, Masahiro Oda and Kensaku Mori. *Tracking and segmentation of the airways in chest CT using a fully convolutional network*, International Conference on Medical Image Computing and Computer-Assisted Intervention (MICCAI 2017), LNCS 10434, pp.198-207, Quebec, Canada, 11-13 September 2017. SCI Index

[C2] **Qier Meng**, Takayuki Kitasaka, Masahiro Oda and Kensaku Mori. *Airway segmentation from 3D chest CT volumes based on volume of interest using gradient vector flow*, International Forum on Medical Imaging in Asia 2017, IFMIA Poster Session P2-18, pp.266-268, January 19-20, 2017.

[C3] **Qier Meng**, Takayuki Kitasaka, Masahiro Oda and Kensaku Mori. *Airway extraction from 3D chest CT volumes based on iterative extension of VOI enhanced by cavity enhancement filter*, In Proceedings of SPIE Medical Imaging 2017. Vol.10134, pp.101370M-1-101370M-9, DOI: 10.1117/12.2216670. EI Index

[C4] **Qier Meng**, Takayuki Kitasaka, Yukitaka Nimura, Masahiro Oda and Kensaku Mori. *Accurate Airway Segmentation Based on Intensity Structure Analysis and Graph-cut*, In Proceedings of the SPIE on Medical Imaging 2016, Vol.9784, pp.97842G-1-97842G-9, DOI: 10.1117/12.2254233 EI Index

[C5] **Qier Meng**, Takayuki Kitasaka, Yukitaka Nimura, Masahiro Oda and Kensaku Mori. *A Study on Improvement of Airway Segmentation using Hybrid Method*, The 3rd IAPR Asian Conference on Pattern Recognition (ACPR2015), November 3-6, 2015, p.225-229, ALOFT KUALA LUMPUR SENTRAL HOTEL, Kuala Lumpur, Malaysia SCI Index

[M1] **Qier Meng**, Takayuki Kitasaka, Yukitaka Nimura and Kensaku Mori, *A New Image Similarity Measure for Bronchoscope Tracking Based on Image Registration*, In Proceedings of the Tokai-Section Joint Conference on Electrical and Related Engineering 2014 (2014/10)

[M2] **Qier Meng**, Takayuki Kitasaka, Yukitaka Nimura, Yoshihoko Nakamura, Masahiro Oda and Kensaku Mori, *A study on bronchus segmentation based on machine learning method from chest CT Image*, MI workshop,Technical Report of IEICE 2015, MI2015-23, Vol.115, No.25, pp.121-126, 2015/05/15 (2015/05)

[M3] **Qier Meng**, Takayuki Kitasaka, Hirohisa Oda, Yukitaka Nimura, Yoshihiko Nakamura, Masahiro Oda and Kensaku Mori. *A preliminary study on false positive reduction of bronchus segmentation using SVM*, In Proceedings of 28th Meeting of the Japanese Society of Medical Imaging Technology, JAMIT 2015, PP30, 2015/07/31 (2015/07)

[M4] **Qier Meng**, Takayuki Kitasaka, Hirohisa Oda, Yukitaka Nimura, Masahiro Oda and Kensaku Mori, "Robust Airway Segmentation Based on Multiscale Cavity Enhancement Filter and Machine learning," In Proceedings of the 19th Meeting of the Japan Society of Computer Assisted Surgery, JSCAS2015, Vol.17, No.3, 15(VI)-4, pp.206-207 (2015/11/22)

References

[1] World Health Organization, Cancer, Fact sheet N297, 2011. [Online] URL http://www.who.int/mediacentre/factsheets/fs297/en/index.html.

[2] Lo P, Ginneken B, Reinhardt J, Yavarna T, Jong P, Irving B, Fetita C, Ortner M, Pinho R, Sijbers J, Feuerstein M, Fabijanska A, Bauer C, Beichel R, Mendoza C, Wiemker R, Lee J, Reeves A, Born R, Weinheimer O, Rikxoort E, Tschirren J, Mori K, Odry B, Naidich D, Hartmann I, Hoffman E, Prokop M, Pedersen J, Bruijne M, "Extraction of Airways From CT (EXACT'09)." IEEE Transactions on Medical Imaging 31(11):2093-2107, 2012.

[3] Kuhnigk JM, Hahn H, Hindennach M, Dicken V, Krass S, Peitgen HO, "Lung lobe segmentation by anatomy-guided 3D watershed transform." Proceeding of SPIE on Medical Imaging 5032:1482-1490,2003.

[4] Mori K, Nakada Y, Kitasaka T, Suenaga Y, Takabatake H, Mori M, Natori H, "Lung lobe and segmental lobe extraction from 3D chest CT datasets based on figure decomposition and Voronoi division." Proceeding of SPIE on Medical Imaging 6914:69144K-1-12, 2008.

[5] Hu S, Hoffman E, Reinhardt J, "Automatic lung segmentation for accurate quantitation of volumetric X-ray CT images." IEEE Transactions on Medical Imaging 20 (6):490-498, 2001.

[6] Lee Y, Hara T, Fujita H, Itoh S, Ishigaki T, "Automated detection of pulmonary nodules in helical CT images based on an improved template-matching technique." IEEE Transactions on Medical Imaging 20(7):595-604, 2001.

[7] Chen B, Kitasaka T, Honma H, Takabatake H, Mori M, Natori H, and Mori K, "Automatic segmentation of pulmonary blood vessels and nodules based on local intensity structure analysis and surface propagation in 3D chest CT images." International Journal of Computer Assisted Radiology and Surgery 7(3):465-482, 2012.

[8] Li B, Christensen GE, Hoffman EA, McLennan G, Reinhardt JM, "Pulmonary CT image registration and warping for tracking tissue deformation during the respiratory cycle through 3D consistent image registration." Medical Physics 35 (12):5575-5583, 2008.

[9] Kiraly AP, Higgins WE, McLennan G, Hoffman EA, Reinhardt JM, "Three dimensional human airway segmentation methods for clinical virtual bronchoscopy." Academic Radiology 9(10):1153-1168, 2002.

[10] National Cancer Institute (NCI) at the National institutes of Health (NIH, US),"Metastatic Cancer: Questions and Answers," NCI FactSheet, Retrieved 2011. [Online]
URL http://www.cancer.gov/cancertopics/factsheet/Sites-Types/metastatic

[11] N. Howlader, A.M. Noone, M. Krapcho, N. Neyman, R. Aminou, W. Waldron, S.F. Altekruse, C.L. Kosary, J. Ruhl, Z. Tatalovich, H. Cho, A. Mariotto, M.P. Eisner, D.R. Lewis, H.S. Chen, E.J, Feuer, K.A. Cronin, B.K. Edwards (eds)., "SEER Cancer Statistics Review," 1975-2008, National Cancer Institute, 2011.
URL http://seer.cancer.gov/csr/1975_2008/

[12] National Cancer Institute (NCI) at the National institutes of Health (NIH, US), "What You Need To Know About^{TM} *LungCancer*," NIH Publication No. 07-1553, 2007. [Online]
URL http://www.cancer.gov/cancertopics/wyntk/lung

[13] M. C. Stoppler, "Lung Cancer, causes, types, and treatment," retrieved from

MedicineNet Inc., 2009. [Online]
URL http://www.medicinenet.com/lung_cancer, 2009.

[14] Xiongbiao Luo, Takayuki Kitasaka, and Kensaku Mori. "Externally Navigated Bronchoscopy Using 2-D Motion Sensors: Dynamic Phantom Validation" IEEE Transactions on Medical Imaging,32(10):1745-1764, 2013

[15] J.D. Minna, J.H. Schiller, "Harrison's Principles of Internal Medicine (17th ed.)." McGraw-Hill, 551-562, 2008.

[16] J.G. Fletcher, W. Luboldt, "CT colonography and MR colonography: current status, research directions and comparison," European Radiology, 10:786-801, 2000.

[17] D.J. Vining, D.W. Gelfand, "Noninvasive colonoscopy using Helical CT scanning, 3D reconstruction, and virtual reality,"The 23rd Annual Meeting of the Society of Gastrointestinal Radiologists, 1994.

[18] D. Bielen, G. Kiss, "Computer-aided detection for CT colonography: update 2007,"Abdominal Imaging, 32(5):571-581, 2007.

[19] Chen, Bin. "Automated Segmentation of Lung Nodules and Pulmonary Blood Vessels and Follow-up Analysis of Lung Nodules from 3D CT Images", NAGOYA Repository, 2012.

[20] URL http://www.icadmed.com/products/mammography/secondlookdigital.htm

[21] R.F. Brem, J.A. Rapelyea, G.Zisman, J.W. Hoffmeister, M.P. Desimio, "Evaluation of breast cancer with a computer-aided detection system by mammographic appearance and histopathology, Cancer, 104(5):931-935, 2005.

[22] S. Ciatto, N. Houssami, D. Gur, R. Nishikawa, R. Schmidt, C. Metz, J. Ruiz, S. Feig, R. Birdwell, M. Linver, J. Fenton, W. Barlow, J. Elmore, "Computer-aided screening mammography," The New England Journal of Medicine (NEJM), 357(1):83-85, 2007.

[23] Pratt W(1991) Digital Image Processing, 2nd Edition, Wiley, New York

[24] D. Aykac, E. Hoffman, G. McLennan, and J. Reinhardt. Segmentation and analysis of the human airway tree from three-dimensional X-ray CT images. IEEE Transactions on Medical Imaging, 22(8):940-950, 2003.

[25] C. Bauer, T. Pock, H. Bischof, and R. Beichel. Airway tree reconstruction based on tube detec Proc. of Second International Workshop on Pulmonary Image Analysis, pages 203-213, 2009.

[26] A. Fabijanska. Results of applying two-pass region growing algorithm for airway tree segmentation to MDCT chest scans from EXACT database. In Proc. of Second International Workshop on Pulmonary Image Analysis, pages 251-260, 2009.

[27] C. Fetita, M. Ortner, P.-Y. Brillet, F. Preteux, and P. Grenier. A morphological-aggregate approach for 3D segmentation of pulmonary airways from generic MSCT acquisitions. In Proc. of Second International Workshop on Pulmonary Image Analysis, pages 215-226, 2009.

[28] URL:explore encyclopedia britannica:www.britannica.com

[29] J.B. West, "Respiratory physiology– the essentials." Baltimore: Williams & Wilkins, 1-10, 2000.

[30] G. Agam, S. G. Armato III, and C. Wu. Vessel tree reconstruction in thoracic CT scans with application to nodule detection. IEEE Transactions on Medical Imaging, 24(4):486-499, April 2005.

[31] Y. K. Lee, Y.-M. Oh, J.-H. Lee, E. K. Kim, J. H. Lee, N. Kim, J. B. Seo, S. D. Lee, and K. O. L. D. S. Group. Quantitative assessment of emphysema, air trapping, and airway thickening on computed tomography. Lung, 186(3):157-165, 2008.

[32] URL:wikipedia: https://en.wikipedia.org/wiki/Bronchus

[33] Giger ML, Huo Z, Kupinski MA, Vyborny CJ, "Computer aided diagnosis in mammography". In: Fitzpatrick JM, Sonka M, editors. The handbook of medical imaging, 2:915-1004, 2000.

[34] B.J. Erickson, B. Bartholmai, "Computer-aided detection and diagnosis at the start of the third millennium," Journal of Digital Imaging, 15(2):59-68, 2002

[35] R.M. Summers, "Road maps for advancement of radiologic computer-aided detection in the 21st century," Radiology, 229(1):11-3, 2003.

[36] K. Doi, "Computer-aided diagnosis in digital chest radiography," Advances in Digital Radiography, RSNA categorical course in Diagnostic Radiology: Physics Syllabus. Oak Brook, IL: RSNA, 2003:227-36, 2003.

[37] K Doi, "Current status and future potential of computer-aided diagnosis in medical imaging," British Journal of Radiology, 78(1):S3-s19, 2005.

[38] J.S. Tang, R.M. Rangayyan, J. Xu, I.E. Naqa, Y.Y. Yang, "Computer-Aided Detection and Diagnosis of Breast Cancer With Mammography: Recent Advances,"IEEE Transactions on Information Technology in Biomedicine, 13(2):236-251, 2009.

[39] E.D. Pisano, C.A. Gatsonis, M.J. Yaffe, R.E. Hendrick, A.N.A. Tosteson, D.G. Fryback, L.W. Bassett, J.K. Baum, E.F. Conant, R.A. Jong, M. Rebner, C.J. D'Orsi, "American college of radiology imaging network digital mammographic imaging screening trial: Objectives and methodology," Radiology, 236(2):404-412, 2005.

[40] J. Wei, B. Sahiner, L. Hadjiiski, H. Chan, N. Petrick, M. Helvie, M. Roubidoux, J. Ge, and C. Zhou, "Computer aided detection of breast masses on full field digital mammograms," Medical Physics, 32(9):2827-2837, 2005.

[41] G. Paone, E. Nicastri, G. Lucantoni, R. D. Lacono, P. Battistoni, A. L. DAngeli, and G. Galluccio. "Endobronchial ultrasound-driven biopsy in the diagnosis of peripheral lung lesions." Chest, 128(5):3551-3557, 2005.

[42] D. P. Steinfort, M. Finlay, and L. B. Irving. "Diagnosis of peripheral pulmonary carcinoid tumor using endobronchial ultrasound." Annals of Thoracic Medicine, 3(4):146-148, 2008.

[43] M. Gomez and G. A. Silvestri. "Endobronchial ultrasound for the diagnosis and staging of lung cancer." The Proceedings of the American Thoracic Society, 6:180-186, 2009.

[44] P. Lee and H. G. Colt. "Bronchoscopy in lung cancer: appraisal of current technology and for the future." Journal of Thoracic Oncology, 5(8):1290-1300, 2010.

[45] L. Serra, T. Poston, W. L. Nowinski, B. C. Chua, H. Ng, and P. K.Pillay. "The brain bench planner and trainer for minimal access surgery." In Proceedings of the ACM Symposium on Virtual Reality Software and Technology, pages 191-192, 1996.

[46] L. Hong, A. Kaufman, Y. C. Wei, A. Viswambharan, M. Wax, and Z. Liang. "3D virtual colonoscopy." In Proceedings Biomedical Visualization, pages 26-32, 1995.

[47] K. Mori, J.ichi Hasegawa, J.ichiro Toriwaki,et al., "Recognition of bronchus in three-362dimensional X-ray CT images with applications to virtualized bronchoscopy system." Proceedings of the 13th International Conference on Pattern Recognition3, 25-29, 1996.

[48] T. Schlatholter, C. Lorenz, I. C. Carlsen, S. Renisch, and T. Deschamps, "Simultaneous segmentation and tree reconstruction of the airways for virtual bronchoscopy," in SPIE Medical Imaging, pp. 103-113, 2002.

[49] C. I. Fetita, F. Pre teux, C. Beigelman-Aubry, and P. Grenier, "Pulmonary airways: 3-D reconstruction from multislice CT and clinical investigation," IEEE Trans. Med. Imaging 23(11), pages 1353-1364, 2004.

[50] Inoue, Tsutomu, Yoshiro Kitamura, Yuanzhong Li, and Wataru Ito. "Robust airway extraction based on machine learning and minimum spanning tree", Medical Imaging 2013 Computer-Aided Diagnosis, 2013.

[51] W. Park, E. A. Hoffman, and M. Sonka, "Segmentation of intrathoracic airway trees: a fuzzy logic approach," IEEE Trans. Med. Imaging 17(4), 489-497, 1998.

[52] L. Fan and C. W. Chen, "Reconstruction of airway tree based on topology and morphological operations," in SPIE Medical Imaging, 46-57, 2000.

[53] T. Kitasaka, K. Mori, J. Hasegawa, and J. Toriwaki,"A method for extraction of bronchus regions from 3D chest X-ray CT images by analyzing structural features of the bronchus,"Lect. Notes Comput. Sci., 603-610, 2003.

[54] M. Sonka, W. Park, and E. A. Hoffman, "Rule-based detection of intrathoracic airway trees," IEEE Trans. Med. Imaging 15(3), 314-326, 1996.

[55] D. Mayer, D. Bartz, J. Fischer, S. Ley, A. del Rio, S. Thust, H. U. Kauczor, and C. P. Heussel, "Hybrid segmentation and virtual bronchoscopy based on CT images," Acad. Radiol. 11(5), 551-565, 2004.

[56] J. Tschirren, E. A. Hoffman, G. McLennan, and M. Sonka, "Intrathoracic airway trees: segmentation and airway morphology analysis from low-dose CT scans," IEEE Trans. Med. Imaging 24(12), 1529-1539 ,2005.

[57] W. B. van Ginneken, W. Baggerman, and E. M. van Rikxoort, "Robust segmentation and anatomical labeling of the airway tree from thoracic CT Scans," Med Image Comput Comput Assist Interv. 11(pt 1), 219-226, 2008.

[58] Lo P, de Bruijne M, "Voxel classification based airway tree segmentation." Proceeding of SPIE on Medical Imaging 6914: 69141K, 2008.

[59] Lo P, Sporring J, Ashraf H, Pedersen J, and Bruijne M, "Vessel-guided airway tree segmentation: A voxel classification approach." Medical Image Analysis 14(4):527-538, 2010.

[60] Yano H, Feuerstein M, Kitasaka T, and Mori K, "Study on bronchus region extraction from 3D chest CT images using local intensity structure analysis and CT value distribution feature." IEICE, MI2009-13:69-74, 2009.

[61] Q. Meng, T. Kitasaka, Y. Nimura,et al., "Automatic segmentation of airway tree based on424local intensity filter and machine learning technique in 3D chest CT volume," Internationa Journal of Computer Assisted Radiology Surgery 12(2), 245-261, 2017.

[62] Q. Meng, T. Kitasaka, M. Oda,et al., "Airway segmentation from 3D chest CT volumes based on volume of interest using gradient vector flow," International Forum on Medical Imaging in Asia (IFMIA), 192-195, 2017.

[63] Q. Meng, H. Roth, T. Kitasaka, M. Oda, J Ueno, K. Mori, "Tracking and segmentation of the airwaysin chest CT using a fully convolutional network" Medical Image Computing and Computer-Assisted Intervention (MICCAI), 2017.

[64] World Health Organization (Feb 2015) Cancer, Fact sheet N deg 297. http://www.who.int/mediacentre/factsheets/fs297/en/

[65] Mori K, Hasegawa J, Toriwaki J, Anno H and Kataba K, "Automated Extraction and Visualization of Bronchus from 3D CT Images of Lung." Proceeding of 1st CVRMIed95:542-548, 1995.

[66] Singh H, Crawford M, Curtin J.P, Zwiggelaar R, "Automated 3D segmentation of the lung airway tree using gain-based region growing approach." In: MICCAI. Lecture Notes in Computer Science:975-982, 2004.

[67] Kitasaka T, Mori K, Hasegawa J and Toriwaki J, "A Method for Extraction of Bronchus Regions from 3D Branch Tracing and Image Sharpening for Airway Tree Chest X-ray Images by Analyzing Structural Features of the Bronchus." Forma 17:321-338, 2002.

[68] Feuerstein M, Kitasaka T and Mori K, "Adaptive Branch Tracing and Image Sharpening for Airway Tree Extraction in 3-D Chest CT." Proceeding of Second International Workshop on Pulmonary Image Analysis:273-284, 2009.

[69] Schlathoelter T, Lorenz C, Carlsena IC, Renischa S and Deschamps T, "Simultaneous segmentation and tree reconstruction of the airways for virtual bronchoscopy." Proceeding of SPIE on Medical Imaging 4684:103-113, 2002.

[70] Meng Q, Kitasaka T, Nimura Y, Oda M, and Mori K (2015) A Study on Improvement of Airway Segmentation using Hybrid Method, The 3rd IAPR Asian Conference on Pattern Recognition:225-229

[71] Meng Q, Kitsaka T, Nimura Y, Oda M, Mori K (2016) Accurate airway segmentation based on intensity structure analysis and graphcut, Proceedings of SPIE, 9784, SPIE Medical Imaging: Computer-Aided Diagnosis

[72] Sato Y, Westin C, Bhalerao A, Nakajima S, Shiraga N, Tamura S, "Tissue classification based on 3D local intensity structures for volume rendering." IEEE Transaction on Visualization Computer Graphics, 6(2):160-180, 2000.

[73] Sato Y, Nakajima S, Shiraga N, Atsumi H, Yoshida S, Koller T, Gerig G, Kikinis R, "3D multiscale line filter for segmentation and visialization of curvilinear structures in medical images." Medical Image Analysis, 2(2):143-168, 1998.

[74] Frangi AF, Niessen WJ, Vincken KL, Viergever MA, "Multiscale vessel enhancement filtering." Medical Image Computing and Computer-Assisted Intervention (MICCAI) 1496:130-137, 1998.

[75] Krissian K, Malandain G, Ayache N, "Model based detection of tubular structures in 3D images." Computer Vision and Image Understanding 80(2):130-171, 2000.

[76] Li Q, Sone S, Doi K, "Selective enhancement filters for nodules, vessels, and airway walls in two and three-dimensional CT images." Medical Physics 30:20-40, 2003.

[77] Hirano Y, Xu R, Tachibana R, and Kido S, "A Method for Extracting Airway Tree by Using a Cavity Enhancement Filter." Fourth International Workshop on Pulmonary Image Analysis:91-99, 2011.

[78] Lesage D, Angelini E.D, Bloch I, Funka-Lea G, "A review of 3D vessel lumen segmentation techniques: Models, features and extraction schemes." Medical image analysis 13(6):819-845, 2009

[79] Chang C , Lin C J, "LIBSVM: a library for support vector machines." ACM Transactions on Intelligent Systems and Technology (TIST) 2(3):27, 2011.

[80] Boykov Y, Veksler O and Zabih R, "Fast Approximate Energy Minimization via Graph Cuts." IEEE Transactions on Pattern Analysis and Machine Intelligence 23(11):1222-1239, 2011.

[81] Boykov Y and Kolmogorov V, "An experimental comparison of min experimental min-cutmax-flow algorithms for energy minimization in vision." IEEE Transactions on Pattern Analysis and Machine Intelligence 26(9):1124-1137, 2004.

[82] Ali AM, El-Baz AS, Farag AA, "A novel framework for accurate lung segmentation using graph cuts." 4th IEEE International Symposium on Biomedical Imaging:908-911, 2007.

[83] T.-Y. Law and P. Heng., "Automated extraction of bronchus from 3D CT images of lung based on genetic algorithm and 3D region growing." SPIE Medical Imaging: Image Processing 3979, 906-916, 2000.

[84] C.I.Fetita, F.Prteux, C.Beigelman-Aubry,et al., "Pulmonary airways: 3-D reconstruction from multislice CT and clinical investigation., IEEE Transactions on Medical Imaging23, 1353-1364, 2004.

[85] D. Bartz, D. Mayer, J. Fischer et al., "Hybrid segmentation and exploration of the human lungs." Proceedings of the 14th IEEE Visualization Conference, 177-184, 2003.

[86] T.Blow, C. Lorenz, and S. Renisch., "A general framework for tree segmentation and reconstruction from medical volume data.," International Conference on Medical Image Computing and Computer-Assisted Intervention3216, 533-540, 2004.

[87] P.Lo, J.Sporring, J.J.H.Pedersen,et al., "Airway tree extraction with locally optimal paths." International Conference on Medical Image Computing and Computer-Assisted Intervention 5762, 51-58, 2008.

[88] C. Bauer and H. Bischof., "A novel approach for detection of tubular objects and its application to medical image analysis," Proceeding of Second International Workshop on Pulmonary Image Analysis 5096, 273-284, 2008.

[89] M. M. G. Macedo, C. Mekkaoui, and M. P. Jackowski., "Vessel centerline tracking in CTA and MRA images using Hough transform," Progress in Pattern Recognition, Image Analysis, Computer Vision, and Applications6419, 295-302, 2010.

[90] Xu, C, Prince, J. L (1998): Snakes, shapes, and gradient vector flow. IEEE Trans. on Image Processing 7(3): 359-369

[91] lvarez L, Baumela L, Henrquez P, Mrquez-Neila P (2010): Morphological snakes. Computer Vision and Pattern Recognition: 2197-2202

[92] Ciecholewski M (2016): An edge-based active contour model using an inflation/deflation force with a damping coefficient. Expert Systems with Applications 44: 22-36.

[93] Zhang K, Song H, Zhang L (2010): Active contours driven by local image fitting energy. Pattern recognition 43(4): 1199-1206

[94] Li C, Huang R, Ding Z, Gatenby JC, Metaxas DN, Gore JC (2011): A level set method for image segmentation in the presence of intensity in homogeneities with application to MRI.IEEE Trans Image Process 20(7):2007-2016

[95] T. Saito, K. Mori, and J. Ichiro Toriwaki., "A sequential thinning algorithm for three dimensional digital pictures using the Euclidean distance transformation and its properties," The transactions of the Institute of Electronics, Information and Communication Engineers J79-D-2(10), 1675-1685, 1996.

[96] K. Palgyi, J. Tschirren, E. A. Hoffman,et al., "Quantitative analysis of pulmonary airway tree structures," Computers in Biology and Medicine36(9), 974-996 (2006).

[97] Mori K, Hasegawa J, Suenaga Y, Junichiro Toriwaki (2001) Automated Anatomical Labeling of the Bronchial Branch and Its Application to the Virtual Bronchoscopy. IEEE Transactions on Medical Imaging 19(2): 103-114.

[98] S.T, L.C, C.IC,et al., "Simultaneous segmentation and tree reconstruction of the airway for virtual bronchoscopy," Proceeding of SPIE on Medical Imaging 4684, 103-113, 2002.

[99] Batchelor PG, Castellano Smith AD, Hill DL, Hawkes DJ, Cox TC, Dean AF, "Measures of folding applied to the development of the human fetal brain," IEEE Transactions on Medical Imaging, 21(8): 953-965 (2002)

[100] J. Long et al., "Fully convolutional networks for semantic segmentation," CVPR, 2015.

[101] O. Ronneberger et al., "U-Net: Convolutional Networks for Biomedical Image Segmentation," MICCAI, 2015.

[102] O. Cicek et al., "3D U-Net: Learning Dense Volumetric Segmentation from Sparse Annotation," 19th International Conference of Medical Image Computing and Computer Assisted Interventions, 2016.

[103] Y. Jia et al., "Caffe: Convolutional architecture for fast feature embedding," ACM Multimedia 2014 Open Source Software Competition, 2014.